

NUMERICAL SIMULATIONS OF BOUNCING JETS

A Dissertation

by

SANGHYUN LEE

Submitted to the Office of Graduate and Professional Studies of
Texas A&M University
in partial fulfillment of the requirements for the degree of
DOCTOR OF PHILOSOPHY

Chair of Committee,	Andrea Bonito
Committee Members,	Jean-Luc Guermond Raytcho Lazarov Kumbakonam Rajagopal
Head of Department,	Emil Straube

August 2014

Major Subject: Mathematics

Copyright 2014 Sanghyun Lee

ABSTRACT

The Kaye effect is a fascinating phenomenon of a leaping shampoo stream which was first described by Alan Kaye in 1963 as a property of non-Newtonian fluid. It manifest itself when a thin stream of non-Newtonian fluid is poured into a dish of fluid. As pouring proceeds, a small stream of liquid occasionally leaps upward from the heap. We investigate numerically the impact of the experimental setting as well as the fluid rheology on the apparition of bouncing jets. In particular, we observe the importance of the creation of a thin lubricating layer of air between the jet and the rest of the liquid. The numerical method consists of a projection method coupled with a level set formulation for the interface representation. Adaptive finite element methods are advocated to capture the different length scales inherent to this context.

In addition, we design and study two modifications of the first order standard pressure correction projection scheme for the Stokes system. The first scheme improves the existing schemes in the case of open boundary condition by modifying the pressure increment boundary condition, thereby minimizing the pressure boundary layer and recovering the optimal first order decay. The second scheme allows for variable time stepping. It turns out that the straightforward modification to variable time stepping leads to unstable schemes. The proposed scheme is not only stable but also exhibits the optimal first order decay. Numerical computations illustrating the theoretical estimates are provided for both new schemes.

ACKNOWLEDGEMENTS

First I wish to thank my advisor, Andrea Bonito, and it has been an honor to be his first Ph.D. student. He guided me to the thesis topic and his academical and emotional support and patience allowed me to now stand at the finish line of the Ph.D. I also appreciate all his contributions of time, ideas and financial support to continue my Ph.D.

Also, my thesis committee and numerical analysis group greatly supported me through all these years. Thank you to Jean-Luc Guermond for sharing so much time for the questions and discussions, and the financial support to travel for several conferences. Thanks to Raytcho Lazarov for being so gentle and generous all of the time, and encouraging me. Also, I want to thank Kumbakonam Rajagopal for sharing his valuable time. I was also fortunate to have Wolfgang Bangerth, one of the authors of deal.II, in our department and thank for the help regarding to developing our code with deal.II. I can't forget the remarkable time at High Speed Imaging Lab in KAUST, thanks to Dr.Thoroddsen and my friend Dr.Li for allowing me to perform a nice experiments.

Finally, and most importantly, I would like to thank my family. Especially, my wife Jiyoung's support, encouragement, quiet patience and unwavering love were the power to pursue my Ph.D. I also want to say that I love my son Joon and daughter Joanne so much. At last, I thank my parents for their faith in me and supporting all the needs during my time in College Station.

My research is partially supported by the National Science Foundation under grant DMS-0914977, DMS-1254618 and award No. KUS-C1-016-04 made by King Abdullah University of Science and Technology.

TABLE OF CONTENTS

	Page
ABSTRACT	ii
ACKNOWLEDGEMENTS	iii
TABLE OF CONTENTS	iv
LIST OF FIGURES	vi
LIST OF TABLES	x
1. INTRODUCTION	1
2. INCREMENTAL PRESSURE CORRECTION PROJECTION METHOD FOR THE TIME-DEPENDENT NAVIER STOKES SYSTEM	5
2.1 Navier Stokes system	5
2.1.1 Initial and boundary conditions	6
2.2 Incremental Pressure Correction Projection Method	6
2.2.1 Stability and error estimate	10
2.2.2 Numerical results	24
2.3 Optimal Incremental Pressure Correction Projection Method for open boundary problem	25
2.3.1 Stability and error estimate	27
2.3.2 Numerical results	38
2.4 Variable time stepping Standard Pressure Correction Projection Method	39
2.4.1 Stability and error estimate	41
2.4.2 Numerical results	52
3. LEVEL SET METHOD WITH REINITIALIZATION AND ENTROPY STABILIZATION	53
3.1 Representation of the free interface via a level set function	53
3.2 Reinitialization and cut off function	54
3.3 Space discretization using Finite Elements	56
3.4 Time discretization	57
3.5 Entropy residual stabilization	58
3.6 Adaptive mesh refinement	61

3.7	Values of numerical parameters	61
3.8	Numerical results	63
3.8.1	Error convergence test	64
3.8.2	Circle rotation	65
3.8.3	Slotted Disk	67
3.8.4	Single Vortex	68
4.	NUMERICAL SIMULATIONS OF TWO PHASE FLOWS	70
4.1	Mathematical model	70
4.2	Space discretization using Finite Elements	71
4.3	Time discretization	72
4.4	Surface Tension	74
4.5	Numerical results	77
4.5.1	Rayleigh-Taylor instability	77
4.5.2	Rising Bubble benchmark problems	78
4.5.3	Buckling fluid	81
5.	NON-NEWTONIAN BOUNCING JET: KAYE EFFECT	82
5.1	Experimental parameters	83
5.2	Shear-thinning model	85
5.3	Existence of the lubricating air layer	86
5.4	Numerical simulation of the Kaye effect	90
5.5	Newtonian bouncing jets	94
6.	CONCLUSION	96
	BIBLIOGRAPHY	97

LIST OF FIGURES

FIGURE	Page
1.1 Comparison of experiment (top) and numerical simulation (bottom) of the Kaye effect.	2
2.1 Errors vs. δt : Convergence rate for original and modified standard pressure correction projection method (a), and modified rotational correction projection method (b) with in particular norms.	38
2.2 Evolution of $\ \mathbf{u}(\cdot, t^n)\ _{L^2(\Lambda)}$ when using the general scheme (2.63)-(2.65) with $\delta t^1 = 0.025$ and δt^n given by (2.66).	40
2.3 Decay of the velocity and pressure errors versus $\overline{\delta t}$ and with the time steps δt^n given by (2.66) when using the proposed scheme. The optimal order of convergence $\mathcal{O}(\overline{\delta t})$ is observed.	51
3.1 An example of a two phase flow system: A fluid(region Ω^+) is entering the cavity filled by another fluid(region Ω^-).	53
3.2 1D Reinitialization steps(from left to right): In a given domain (-1,1), initial distance function $\phi_0 = 0.0625x$ (Solid line) is given and we apply the reinitialization steps with the cut off function(Dashed line) given as (3.6) with $C_\phi = 0.0625$, $\varepsilon_S = 0$, $\mathbf{u} = \mathbf{0}$, and $\lambda = 1$	55
3.3 (a) The initial shape of the level set: the circle with a radius of 1, centered at (0.5,0) in domain $\Lambda = (-1.1)^2$. (b)-(d) illustrates the shape of the level set after 1 cycle (360°) rotated by the velocity given at (3.20). We observe that the entropy residual method preserves the initial value more better.	59
3.4 Adaptivity: Refining meshes with the given initial level set at Figure 3.3.	61
3.5 Plots $Y = C_\phi \tanh(x)$ with $C_\phi = 0.1$, a line with slope 1 and the positions of several constants given at Table 3.1.	62

3.6	Single Vortex convergence test for $t = 0, 0.25, 0.5, 0.75$, and 1. Solid line indicates the contour of zero level set value. In this case, $C_\lambda = C_{\text{Lin}} = C_{\text{Ent}} = 0$	64
3.7	Illustrates the value of the level set which is plotted over the line $(0.5, -0.4) - (0.5, 0.4)$, see (a). For (b)-(e), the solid line indicates the initial value ϕ_0 and the dotted line is the value of ϕ after one cycle. (b) Without any stabilization ($C_{\text{Lin}} = C_{\text{Ent}} = 0$) and without reinitialization($\lambda = 0$). (c) Only adding the first order linear stabilization term with $C_{\text{Lin}} = 0.1$. No oscillations are observed but ϕ is diffused by first order linear stabilization at the corners. (d) With the entropy residual stabilization method. $C_{\text{Lin}} = 0.1$ and $C_{\text{Ent}} = 0.1$. (e) Finally also adding reinitialization with $\lambda = 0.1$	66
3.8	(a) The value of the entropy residual $ R_E(\phi) $ (white: large; black: low). As expected, the entropy residual is large near the interface(solid line), where ϕ is not smooth. (b) Choice of viscosity: μ_E (black), μ_F (white). Again, as expected, the linear viscosity μ_F is active where ϕ is not smooth(near the interface). (c)-(e) depicts the solution after 5,15, and 20 time steps. We see that the diffusion from the algorithm smooth ϕ near the interface in such a way only the entropy viscosity μ_E is active.	66
3.9	Comparing the contour of $\phi_0 = 0$ (outside) to the contour of $\phi = 0$ after one cycle, 360° (inside).	67
3.10	Rotating Slotted Disk at each position.	67
3.11	Single Vortex: Illustrates the deformation of the initial circle in corresponding time from $t = 0$ to $t = 4$. (a)-(d) and (f)-(i) shows the shape of the vortex in each time compare to the initial circle. (d) and (i) are comparing the contour of $\phi(t) = 0$ and $\phi^0 = 0$ at $t = 2$ and $t = 4$. (e) and (j) plots the level set value over the line $(-0.3, 0.5) - (0.3, 0.5)$, at $t = 2$ and $t = 4$ respectively, and confirms that the computed results are almost identical with the initial data. Compare with Figure 3.6, an another Single Vortex example we performed without any reinitialization, cut off function, and any stabilization.	68
3.12	Single Vortex 3D: Deformation of the sphere at several times. Vectors indicate the velocity field.	69
4.1	The interface is shown at times 1, 1.5, 1.75, 2, 2.25, and 2.5. Compare the result with [30].	77

4.2	Comparison of the rising bubble test case #1.	79
4.3	Comparison of the rising bubble test case #2.	80
4.4	Rising bubble problem test case #2 at time=3. The right end bubble is our result, and left bubbles are from [38].	80
4.5	Buckling fluid in 2D.	81
4.6	Buckling Silicone Oil in 3D.	81
5.1	Kaye effect(from left to right): The fluid buckles at first producing a heap and a stream of liquid suddenly leaps outside the heap. Experiments taken with Dr.Thoroddsen and Dr.Li at High Speed Fluid Imaging Lab in KAUST.	82
5.2	(a) Setup for free falling Kaye effect. We use the high speed video imaging camera, Phantom V1610 CMOS at frame rates up to 12,000 fps. Also we use a long-distance microscope(Leica Z16 APO) at optical magnifications up to 4×, giving 7 μm/px. Backlighting was accomplished with a 350W metal-halide lamp(Sumita), shone on to a diffuser. (b) Notations: H is the height of the free falling jet, R is the diameter of the inflow jet, r is the diameter of the jet at the bottom and V_{in} indicates the velocity of the jet at the bottom.	83
5.3	Pictures of the fluids corresponding to the parameters provided in Table 5.1.	84
5.4	Jets with different volume flow rates: (5,6,7,and 8 ml/min). The Kaye effect is observed for values of Q starting at 7.	85
5.5	Shear-thinning viscosity of the shampoo: ‘+’ points illustrate the physical value of the viscosity(Y-axis) depending on shear(X-axis) observed from the rheology test of the shampoo. Solid line is the numerical viscosity model of the shampoo by using (5.1) with the constants (5.2).	86
5.6	Fluid tank: Fluid will drop from the top to this tank. We confine the pool to a narrow channel between two glass walls, through which we can view the jet-turning region within the pool. The large viscosity of the shampoo, only allows slow downhill gliding of the pool, at about 4 mm/s of pool surface velocity.	87

5.7	Overall view of the shampoo jet bouncing of an inclined pool of the same liquid. The white arrow points at he breakup of the air layer into threads and bubbles. The scale bar is 3 mm long. The relative times of the frames are $t = 0, 124, 287, 296, 308, 324$ and 335 ms from left to right and top to bottom. The incoming jet is 0.3 mm in diameter, approaching the pool at 1.2 m/s.	88
5.8	Break up of the air layer under the jet. Times relative to first observed rupture are $t = -717, -189, 20,$ and 132 ms(from left to right). The incoming jet is 0.56 mm in diameter and approaches the pool at 1.59 m/s.	89
5.9	(left) The trajectory of typical particles within the jet. The solid curve marks the air layer and the dotted curve the upper side of the jet if the cross-section remains circular. (right) The velocity vs horizontal location along the curving jet.	90
5.10	The computational domain with boundary.	91
5.11	Shear-thinning viscosity of the fluid. (a) Illustrates the numerical result with the shear-thinning constants given in (5.2). (b) Shear-thinning viscosity with values in (5.2)(dotted line), and (5.5) with the solid line.	92
5.12	Numerical simulation of the Kaye effect with adaptive meshes (from left to right and top to bottom). From the fifth frame to the end, we observe the air layer under the leaping jet(white arrow).	93
5.13	Newtonian bouncing jet (from left to right). The white arrow indicates the direction of the bath flow. (Top) Numerical simulation of the bouncing jet with bath velocity 8 cm/s and surface tension coefficient $\sigma = 21$ mN/m. (Middle) Without the surface tension. (Bottom) With surface tension but increased the bath velocity to 25 cm/s. We observe the existence of the air layer between the jet and the bath.	94

LIST OF TABLES

TABLE	Page
2.1	Error vs. δt : Standard first order Euler scheme. 24
2.2	Error vs. δt : Rotational BDF2 second order scheme. 24
3.1	Suggested numerical parameters which are appropriate for our algorithm. Values of $\varepsilon_H, \varepsilon_S$, and ε_R according to above values $\mathbf{x}_H, \mathbf{x}_S$ and \mathbf{x}_R are shown at Figure 3.5. 62
3.2	Convergence rate for SSP RK3 on the exact solution given by (3.18). The expected third order of convergence is observed. 63
3.3	Convergence rate of the error $\ \phi(T_C) - \phi_0\ _{L^2}$ for the Single Vortex test in Figure 3.6. L^2 error is calculated at the time $T = 1$. The expected third order of convergence is recovered. 65
4.1	Two different sets of physical constants for the rising bubble benchmark. 78
5.1	Free falling Kaye effect with the setup described in Figure 5.2: we change H from 5 cm to 40 cm. It shows that H should be higher enough (more than 30 cm) to observe the bouncing jet, the Kaye effect. Higher H gives larger V_{in} and smaller r 84
5.2	Kaye effect depending on Q . Here the jet falls from a fixed height $H = 2$ cm. Again, larger Q gives larger V_{in} and smaller r 85

1. INTRODUCTION

Prediction and study of fluid dynamics is one of the major interests in mathematical and experimental science. For example, fluid flows can be hurricanes, transporting air pollutions, heating buildings, air interacting with vehicles, and blood flows. Accurate numerical predictions start with adequate mathematical models generally described by partial differential equations. Providing reliable numerical approximations is the next significant step. In an ultimate step, the validation of the overall process consists in comparing numerical predictions with experimental data. Our efforts and the aim of this thesis is to provide accurate numerical simulations of Newtonian [41, 50] and non-Newtonian [7, 16, 39, 42, 54] bouncing jets. The latter is referred as the Kaye effect. Thrasher et al. [50] and Lockhart et al. [41] demonstrated the existence of an air layer under the Newtonian bouncing jets. However for the Kaye effect, whether non-Newtonian effects such as shear-thinning are sufficient for the jet to glide on top a liquid layer or if an air layer is necessary even in that case was on the debate; see [7, 50, 54]. This is one of the motivation for the present study. Lab experiments using high speed cameras [40] as well as numerical evidences are presented in this study and shows unambiguously the presence of an air layer during the Kaye effect. Figure 1.1 shows the comparison of experiment data and numerical simulation of the Kaye effect.

The Navier Stokes equation are the basic model for fluid dynamics. Numerical approximations are based on a Chorin-Temam projection method type [13, 14, 25, 47, 48] coupled with finite elements [11, 15, 21, 24, 23, 28] for the space discretization and several time marching discretization methods.

An important feature of our algorithm is its ability to automatically deduct the

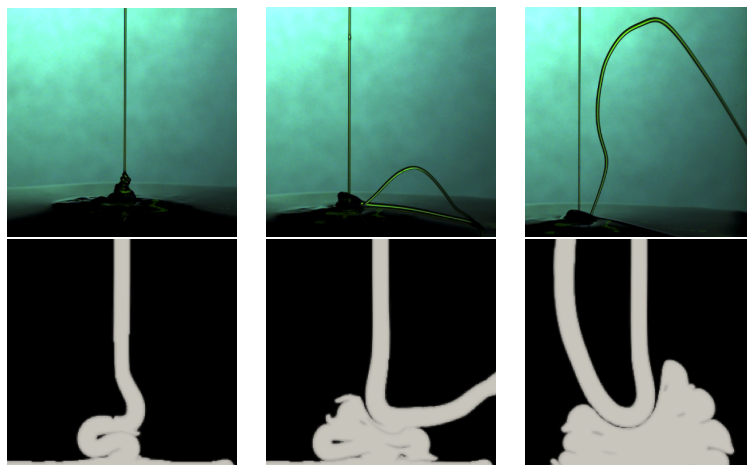


Figure 1.1: Comparison of experiment (top) and numerical simulation (bottom) of the Kaye effect.

necessary amount of effort for a desired accuracy. In fact, adaptive algorithms are crucial in this context in order to optimally balance the computational effort and to provide the small enough scales inherent to bouncing jets.

Many commercial and open sources are available for simulations of two phase flows, but here we use our own developed C++ code, by using deal.II finite element library. See [3, 4, 5] for any additional information. Due to the large number of degree of freedoms for sufficiently refined mesh for accuracy and 3D computations, we also use MPI(Message Passing Interface) library [22] to execute the parallel computation with more than a single processor. To distribute the mesh, data, and computations to multiple processors, we use p4est [12] library, and for linear algebra to create and compute vectors and matrices, deal.II is compatible and already linked with BLAS [8], LAPACK [1], Trilinos [36], and PETSc [2].

This thesis is organized as follows. Chapter 2 starts by introducing the mathematical model, namely the Navier Stokes system, together with its approximation method. It continues to derive a modified projection method for open boundary

problem. The current pressure correction projection method suffers a loss of error convergence rate [33]. Our modified scheme restores the optimal rate of convergence. This is achieved by modifying adequately the boundary condition, thereby attenuating the boundary layer that standard scheme suffer from [29]. However, this is possible at the expense of requiring a consistent ‘grad-div’ term guaranteeing the stability of the method. Similarly, the standard pressure correction projection algorithm do not allow for variable time stepping. We design and study a modified scheme allowing for variable time stepping. Both modified schemes apply in the context of bouncing jets.

A level set method is used to track the interface between two fluids. Chapter 3 presents some novel advanced features in its implementation using finite elements. We use a reinitialization method with filters introduced by Ville et al. [55], take advantage of accurate entropy viscosity stabilization term [35], and adaptive finite element method to accurately capture the two fluid interface. Several classical level set benchmark problems are provided at the end of the chapter to validate our algorithms.

The full algorithm approximating the two phase flow system by combining the numerical method for Navier Stokes system and level set equation is described in Chapter 4. To validate our numerical algorithm, we compare again classical benchmarks and experimental data.

The two phase flow algorithm is used in Chapter 5 to obtain numerical simulations of bouncing jets. We perform physical lab experiments with particular shampoo to gather the important parameters to observe the Kaye effect. Also, we determine the parameters for the shear thinning viscosity model. Those parameters are fed in our numerical algorithm, which ultimately predict jet bouncing for both, Newtonian and non-Newtonian fluids. An air layer between the bouncing jet and the fluid is

observed at each instance.

2. INCREMENTAL PRESSURE CORRECTION PROJECTION METHOD FOR THE TIME-DEPENDENT NAVIER STOKES SYSTEM

Time dependent Navier Stokes system is the common model to describe the motion of small Mach number fluids, which relates the velocity field \mathbf{u} and the pressure p . We start this chapter by briefly introducing the Navier Stokes system.

2.1 Navier Stokes system

Let $\Lambda \subset \mathbb{R}^d$ ($d = 2, 3$) be the open and bounded computational domain with Lipschitz boundary $\partial\Lambda$, and $T > 0$ be the final time of the computation. We consider incompressible fluids. In particular, the density does not depend on the pressure, the temperature, and composition. This is a reasonable assumption for fluids with small Mach number as considered in this study.

To model an incompressible Newtonian fluid, we use the incompressible Navier Stokes system relating the velocity $\mathbf{u} : \Lambda \times [0, T] \rightarrow \mathbb{R}^d$ and the pressure $p : \Lambda \times [0, T] \rightarrow \mathbb{R}$ by,

$$\rho \left(\frac{\partial}{\partial t} \mathbf{u} + \mathbf{u} \cdot \nabla \mathbf{u} \right) = 2 \operatorname{div}(\mu \nabla^S \mathbf{u}) - \nabla p + \mathbf{f} \quad \text{in } \Lambda \times [0, T], \quad (2.1)$$

$$\operatorname{div}(\mathbf{u}) = 0 \quad \text{in } \Lambda \times [0, T], \quad (2.2)$$

where $\nabla^S \mathbf{u}$ denotes the symmetric gradient, $\nabla^S \mathbf{u} := \frac{1}{2} (\nabla \mathbf{u} + \nabla \mathbf{u}^T)$, \mathbf{f} is an external force, and ρ and μ are the fluid density and viscosity, respectively.

Notice that we will also consider shear dependent viscosity models, i.e. μ in (2.1) depends on $|\nabla^S \mathbf{u}|$. Here we use the notation $|\mathbf{v}| := \sqrt{\sum_{i=1}^d (\mathbf{v}_i)^2}$ for a vector $\mathbf{v} \in \mathbb{R}^d$ of components \mathbf{v}_i , $i = 1, \dots, d$, $|M| := \sqrt{M : M}$ for a matrix $M \in \mathbb{R}^{d \times d}$ of components M_{ij} , $1 \leq i, j \leq d$, and where $M : M := \sum_{i=1}^d \sum_{j=1}^d (M_{ij})^2$.

2.1.1 Initial and boundary conditions

The Navier Stokes system (2.1)-(2.2) is supplemented by initial and boundary conditions. To describe them, we decompose the boundary in two parts Γ_D and Γ_N , which are both open sets satisfying $\bar{\Gamma}_D \cup \bar{\Gamma}_N = \partial\Lambda$, and $\Gamma_D \cap \Gamma_N = \emptyset$.

To model inflows, outflows or obstacles the fluid cannot pass through, we set

$$\mathbf{u} = \mathbf{f}_D \quad \text{on} \quad \Gamma_D \times (0, T], \quad (2.3)$$

which is called Dirichlet boundary condition for given $\mathbf{f}_D : \Gamma_D \times (0, T] \rightarrow \mathbb{R}^d$. To model boundary forces, we set

$$\left(2\mu\nabla^S \mathbf{u} - p\right) \boldsymbol{\nu} = \mathbf{f}_N \quad \text{on} \quad \Gamma_N \times (0, T], \quad (2.4)$$

for given $\mathbf{f}_N : \Gamma_N \times (0, T] \rightarrow \mathbb{R}^d$, where $\boldsymbol{\nu}$ denotes the toward unit normal to Λ . In addition, the initial velocity is provided by,

$$\mathbf{u}(\cdot, 0) = \mathbf{u}_0 \quad \text{in} \quad \Lambda, \quad (2.5)$$

where $\mathbf{u}_0 : \Lambda \rightarrow \mathbb{R}^d$ is a given initial velocity.

2.2 Incremental Pressure Correction Projection Method

Among the several numerical methods available to solve the time dependent Navier Stokes system for incompressible flows, we will focus on projection methods, originally proposed by Chorin and Temam [13, 14, 47, 48], see also Goda [25]. We refer to Guermond et al. [34] for an overview of projection methods and to [29, 31, 32, 33, 44] for description and analysis of various projection methods.

We focus on the Stokes system and note that the extension to the Navier Stokes

system is treated similarly with the additional, but well known, techniques used to cope with the nonlinearity. For this section, we only consider homogeneous cases of Dirichlet boundary conditions with $\Gamma_N = \emptyset$ and $\mathbf{f}_D = \mathbf{0}$ in (2.3), i.e.

$$\mathbf{u} = \mathbf{0} \quad \text{on } \partial\Lambda. \quad (2.6)$$

In this case, the pressure is not unique and rather up to a constant. We fix the constant by assuming $\int_\Lambda p = 0$. Given a positive integer N , let $0 = t^0 < t^1 < t^2 < \dots < t^N = T$ be a subdivision of the time interval $[0, T]$ and denote by $\delta t^n := t^n - t^{n-1}$ the time steps for $n = 1, \dots, N$. The time derivative is written in short \mathbf{u}_t , i.e. $\mathbf{u}_t(t) := \frac{\partial}{\partial t} \mathbf{u}(t)$. The norm in $L^2(\Lambda)$ is denoted by $\|\cdot\|_{L^2(\Lambda)}$ and we equip $H^1(\Lambda)$ with the norm $\|\cdot\|_{H^1(\Lambda)} := \left(\|\cdot\|_{L^2(\Lambda)}^2 + \|\nabla \cdot\|_{L^2(\Lambda)}^2 \right)^{1/2}$, and denote the semi-norm $|\cdot|_{H^1(\Lambda)} := \|\nabla \cdot\|_{L^2(\Lambda)}$. The $L^2(\Lambda)$ inner product is denoted by (\cdot, \cdot) , and we define $L_0^2(\Lambda) := \{v \in L^2(\Lambda) \mid \int_\Lambda v = 0\}$. Corresponding norms for vector functions are defined by $\|\mathbf{v}\|_{[E]^d} := \|\mathbf{v}\|_E$ written in short $\|\mathbf{v}\|_E$ for $E = L^2(\Lambda)$ or $H^1(\Lambda)$. Also we shorter notation $\|\cdot\|_2$ for $\|\cdot\|_{L^2(\Lambda)}$ and $\|\cdot\|_1$ for $\|\cdot\|_{H^1(\Lambda)}$ whenever it is unambiguous to do so. Given a sequence of function $\varphi := \{\varphi^n\}_{n=0}^N \subset E$, for $E = L^2(\Lambda)$ or $H^1(\Lambda)$, we define the following norms:

$$\|\varphi\|_{l^2(E)} := \left(\sum_{n=0}^N \delta t^n \|\varphi^n\|_E^2 \right)^{1/2}, \quad \|\varphi\|_{l^\infty(E)} := \max_{0 \leq n \leq N} (\|\varphi^n\|_E), \quad (2.7)$$

and

$$\|\varphi\|_{L^2(t^n, t^{n+1}; E)} = \left(\int_{t^n}^{t^{n+1}} \|\varphi\|_E^2 dt \right)^{1/2}.$$

In addition we introduce some notations:

$$(\varphi^n)^* := 2\varphi^n - \varphi^{n-1}, \quad \delta(\varphi^{n+1}) := \varphi^{n+1} - \varphi^n, \quad \delta^2(\varphi^{n+1}) := \varphi^{n+1} - 2\varphi^n + \varphi^{n-1}.$$

The expression, $A \lesssim B$ denotes $A \leq cB$ with an any positive constant c , independent of the arguments of $A(\cdot)$ and $B(\cdot)$.

We revisit the analysis of the standard incremental pressure correction method using implementable scheme in Section 2.2 to gain insight on the modifications needed to recover optimal convergence rate for open boundary discussed in Section 2.3, and variable time stepping scheme considered in Section 2.4.

We now recall the first order incremental pressure correction scheme [25, 29, 44] applied to system (2.1)-(2.2) with the uniform time discretization δt , i.e. $\delta t^n = \delta t$, $\forall n = 1, \dots, N$. The approximations of $\mathbf{u}(\cdot, t^n)$, $\tilde{\mathbf{u}}(\cdot, t^n)$, and $p(\cdot, t^n)$, for $n = 0, \dots, N$, are denoted \mathbf{u}^n , $\tilde{\mathbf{u}}^n$, and p^n , respectively. We seek recursively the velocity \mathbf{u}^{n+1} , and the pressure p^{n+1} in three steps. Note that together with an initial velocity $\tilde{\mathbf{u}}^0 := \mathbf{u}^0$, the algorithm requires an initial pressure $p^0 \in L_0^2(\Lambda)$. Given $\tilde{\mathbf{u}}^n \in [H_0^1(\Lambda)]^d$ and $p^n \in L_0^2(\Lambda)$, the first sub step accounts for the viscous diffusion, and entails to find $\mathbf{u}^{n+1} \in [H_0^1(\Lambda)]^d$ the solution of

$$\rho \frac{\mathbf{u}^{n+1} - \tilde{\mathbf{u}}^n}{\delta t} - 2\operatorname{div} \left(2\mu \nabla^S \mathbf{u}^{n+1} \right) + \nabla p^n = \mathbf{f}(\cdot, t^{n+1}), \quad \text{in } \Lambda. \quad (2.8)$$

The second step consists in seeking $\tilde{\mathbf{u}}^{n+1} \in \mathbf{H}(\Lambda)$, where

$$\mathbf{H}(\Lambda) := \{ \mathbf{v} \in [L^2(\Lambda)]^d; \operatorname{div}(\mathbf{v}) = 0; \mathbf{v} \cdot \boldsymbol{\nu}|_{\partial\Lambda} = 0 \},$$

and $\psi^{n+1} \in H^1(\Lambda) \cap L_0^2(\Lambda)$ by solving,

$$\frac{1}{\delta t} (\tilde{\mathbf{u}}^{n+1} - \mathbf{u}^{n+1}) + \frac{1}{\rho} \nabla \psi^{n+1} = 0 \quad \text{in } \Lambda. \quad (2.9)$$

Finally, we can update the pressure via the relation,

$$p^{n+1} = \psi^{n+1} + p^n. \quad (2.10)$$

Note that the step (2.9) is the orthogonal decomposition of $[L^2(\Lambda)]^d$, called Helmholtz decomposition,

$$[L^2(\Lambda)]^d = \mathbf{H}(\Lambda) \oplus \nabla H^1(\Lambda),$$

which plays a key role in the analysis of projection method. However, the above algorithm is not ‘implementable’, and (2.9) is not a Poisson problem. Also the projected velocity $\tilde{\mathbf{u}}^{n+1}$ is not an $[H_0^1(\Lambda)]^d$ function. An alternate ‘implementable’ scheme is now derived. First, add (2.9) at time t^n and (2.8) at time t^{n+1} to obtain

$$\rho \frac{\mathbf{u}^{n+1} - \mathbf{u}^n}{\delta t} - 2\operatorname{div}(\mu \nabla^S \mathbf{u}^{n+1}) + \nabla(p^n + \psi^n) = \mathbf{f}(\cdot, t^{n+1}) \quad \text{in } \Lambda. \quad (2.11)$$

Next, the divergence of relation (2.9) leads to

$$\Delta \psi^{n+1} = \frac{\rho}{\delta t} \operatorname{div}(\mathbf{u}^{n+1}) \quad \text{in } \Lambda, \quad (2.12)$$

which is supplemented with the boundary condition

$$\frac{\partial}{\partial \boldsymbol{\nu}} \psi^{n+1} = 0 \quad \text{on } \partial \Lambda. \quad (2.13)$$

Finally, the pressure update remains unchanged

$$p^{n+1} = \psi^{n+1} + p^n. \quad (2.14)$$

Relation (2.11)-(2.14) defines the so-called implementable algorithm, which is equiv-

alent to (2.8)-(2.10).

2.2.1 Stability and error estimate

We start from deriving the variational form of the Stokes system (2.1)-(2.2) by taking $L^2(\Lambda)$ inner product with corresponding test functions and applying the boundary conditions (2.6), to cancel the boundary term appearing after the integration by parts. Thus, for almost every $t \in (0, T]$, we find $\mathbf{u}(t) \in [H_0^1(\Lambda)]^d$ and $p(t) \in L_0^2(\Lambda)$ that solves,

$$\int_{\Lambda} \rho \frac{\partial}{\partial t} \mathbf{u}(t) \mathbf{v} + \int_{\Lambda} 2\mu (\nabla^S \mathbf{u}(t) : \nabla^S \mathbf{v}) - \int_{\Lambda} p(t) \operatorname{div}(\mathbf{v}) = \int_{\Lambda} \mathbf{f}(t) \mathbf{v}, \quad \forall \mathbf{v} \in [H_0^1(\Lambda)]^d, \quad (2.15)$$

with

$$\int_{\Lambda} q \operatorname{div}(\mathbf{u}(t)) = 0, \quad \forall q \in L_0^2(\Lambda). \quad (2.16)$$

Similarly, we derive the weak formulation of the implementable scheme (2.11)-(2.14).

First, we seek $\mathbf{u}^{n+1} \in [H_0^1(\Lambda)]^d$ that solves

$$\begin{aligned} \int_{\Lambda} \rho \left(\frac{\mathbf{u}^{n+1} - \mathbf{u}^n}{\delta t} \right) \mathbf{v} + \int_{\Lambda} 2\mu (\nabla^S \mathbf{u}^{n+1} : \nabla^S \mathbf{v}) - \int_{\Lambda} (p^n + \psi^n) \operatorname{div}(\mathbf{v}) \\ = \int_{\Lambda} \mathbf{f}(\cdot, t^{n+1}) \mathbf{v}, \quad \forall \mathbf{v} \in [H_0^1(\Lambda)]^d, \end{aligned} \quad (2.17)$$

and $\psi^{n+1} \in H^1(\Lambda) \cap L_0^2(\Lambda)$ that solves

$$\int_{\Lambda} \nabla \psi^{n+1} \nabla q = - \int_{\Lambda} \frac{\rho}{\delta t} \operatorname{div}(\mathbf{u}^{n+1}) q, \quad \forall q \in H^1(\Lambda) \cap L_0^2(\Lambda). \quad (2.18)$$

The stability of the velocity field approximation is guaranteed by the following theorem (cf. [29]).

Theorem 2.2.1 (Velocity Stability). Set $\mathbf{f} = \mathbf{0}$ in (2.11), then there holds

$$\rho \|\mathbf{u}\|_{l^\infty(L^2(\Lambda))}^2 + 4\mu \|\nabla^S \mathbf{u}\|_{l^2(L^2(\Lambda))}^2 + \frac{\delta t^2}{\rho} \|\nabla p\|_{l^\infty(L^2(\Lambda))}^2 \leq \rho \|\mathbf{u}^0\|_0^2 + \frac{\delta t^2}{\rho} \|\nabla p^0\|_0^2,$$

provided $\mathbf{u}_0 \in [L_2(\Lambda)]^d$ and $p_0 \in H^1(\Lambda)$.

Proof. Choosing $\mathbf{v} = 2\delta t \mathbf{u}^{n+1}$ in (2.17) we find,

$$\rho(\|\mathbf{u}^{n+1}\|_0^2 - \|\mathbf{u}^n\|_0^2 + \|\delta \mathbf{u}^{n+1}\|_0^2) + 4\delta t \mu \|\nabla^S \mathbf{u}^{n+1}\|_0^2 = 2\delta t(p^n + \psi^n, \operatorname{div}(\mathbf{u}^{n+1})).$$

To control the right hand side term in the above equation, we use (2.18) by taking $q = 2\delta t^2(p^n + \psi^n)$, which gives

$$2\delta t \rho(\operatorname{div}(\mathbf{u}^{n+1}), p^n + \psi^n) = -2\delta t^2(\nabla \psi^{n+1}, \nabla p^n + \nabla \psi^n).$$

Consequently,

$$\begin{aligned} & 2\delta t \rho(\operatorname{div}(\mathbf{u}^{n+1}), p^n + \psi^n) \\ &= -\delta t^2 \|\nabla \psi^n\|_0^2 + \delta t^2 \|\nabla \delta \psi^{n+1}\|_0^2 - \delta t^2 \|\nabla p^{n+1}\|_0^2 + \delta t^2 \|\nabla p^n\|_0^2. \end{aligned} \quad (2.19)$$

To derive the estimate for the term $\delta t^2 \|\nabla \delta \psi^{n+1}\|_0^2$ in the right hand side of the above relation, we take difference between two successive relations of (2.18) and take the integration by parts with applying the boundary condition (2.6). Choosing $q = \delta t \delta \psi^{n+1}$, we obtain,

$$\delta t(\nabla \delta \psi^{n+1}, \nabla \delta \psi^{n+1}) = \rho(\delta \mathbf{u}^{n+1}, \nabla \delta \psi^{n+1}).$$

So that a Cauchy Schwarz inequality yields

$$\frac{\delta t^2}{\rho} \|\nabla \delta \psi^{n+1}\|_0^2 \leq \rho \|\delta \mathbf{u}^{n+1}\|_0^2. \quad (2.20)$$

In view of (2.19) and (2.20), we have

$$\rho \|\mathbf{u}^{n+1}\|_0^2 + 4\delta t \mu \|\nabla^S \mathbf{u}^{n+1}\|_0^2 + \frac{\delta t^2}{\rho} \|\nabla \psi^n\|_0^2 + \frac{\delta t^2}{\rho} \|\nabla p^{n+1}\|_0^2 \leq \rho \|\mathbf{u}^n\|_0^2 + \frac{\delta t^2}{\rho} \|\nabla p^n\|_0^2.$$

Finally, summing the relation for $n = 0, \dots, N-1$, we arrive at the following estimate

$$\begin{aligned} \rho \|\mathbf{u}^N\|_0^2 + 4\mu \sum_{n=0}^{N-1} (\delta t \|\nabla^S \mathbf{u}^{n+1}\|_0^2) + \frac{1}{\rho} \sum_{n=0}^{N-1} (\delta t^2 \|\nabla \psi^n\|_0^2) + \frac{\delta t^2}{\rho} \|\nabla p^N\|_0^2 \\ \leq \rho \|\mathbf{u}^0\|_0^2 + \frac{\delta t^2}{\rho} \|\nabla p^0\|_0^2. \quad \square \end{aligned}$$

We now discuss the convergence of the time discretization by starting with the estimate of

$$\mathcal{R}_0(t^{n+1}) := \frac{\mathbf{u}(t^{n+1}) - \mathbf{u}(t^n)}{\delta t} - \mathbf{u}_t(t^{n+1}). \quad (2.21)$$

Lemma 2.2.1. Assuming that \mathbf{u} is smooth enough, then

$$\|\mathcal{R}_0(t^{n+1})\|_0 \leq (\delta t)^{1/2} \|\mathbf{u}_{tt}\|_{L^2(t^n, t^{n+1}; L^2(\Lambda))}.$$

Proof. The Taylor expansion yields

$$\mathbf{u}(t^n) = \mathbf{u}(t^{n+1}) - \delta t \mathbf{u}_t(t^{n+1}) + \int_{t^{n+1}}^{t^n} (t^n - t) \mathbf{u}_{tt}(t) dt, \quad (2.22)$$

and so that

$$\left\| \frac{1}{\delta t} (\mathbf{u}(t^{n+1}) - \mathbf{u}(t^n)) - \mathbf{u}_t(t^{n+1}) \right\|_0 \leq \int_{t^n}^{t^{n+1}} \|\mathbf{u}_{tt}\|_0 dt.$$

Using a Cauchy Schwarz estimate we get,

$$\|\mathcal{R}_0(t^{n+1})\|_0 \leq (\delta t)^{1/2} \left(\int_{t^n}^{t^{n+1}} \|\mathbf{u}_{tt}\|_0^2 dt \right)^{1/2}. \quad \square$$

Also, we will need an estimate of the increment $\delta\mathcal{R}_0(t^{n+1})$ provided by the next lemma.

Lemma 2.2.2. Assuming \mathbf{u} is smooth enough, then

$$\|\delta\mathcal{R}_0(t^{n+1})\|_0 \lesssim (\delta t)^{3/2} \|\mathbf{u}_{ttt}\|_{L^2(t^{n-1}, t^{n+1}; L^2(\Lambda))}.$$

Proof. We rewrite the residual $\delta\mathcal{R}_0(t^{n+1})$ as follows:

$$\begin{aligned} \delta\mathcal{R}_0(t^{n+1}) &= \left(\frac{\mathbf{u}(t^{n+1}) - \mathbf{u}(t^n)}{\delta t} - \mathbf{u}_t(t^{n+1}) \right) - \left(\frac{\mathbf{u}(t^n) - \mathbf{u}(t^{n-1})}{\delta t} - \mathbf{u}_t(t^n) \right) \\ &= \frac{\mathbf{u}(t^{n+1}) - 2\mathbf{u}(t^n) + \mathbf{u}(t^{n-1})}{\delta t} - (\mathbf{u}_t(t^{n+1}) - \mathbf{u}_t(t^n)), \end{aligned} \quad (2.23)$$

and use following Taylor expansions to estimate the above terms.

$$\mathbf{u}(t^{n+1}) = \mathbf{u}(t^n) + \delta t \mathbf{u}_t(t^n) + \frac{\delta t^2}{2} \mathbf{u}_{tt}(t^n) + \frac{1}{2} \int_{t^n}^{t^{n+1}} (t^{n+1} - t)^2 \mathbf{u}_{ttt}(t) dt, \quad (2.24)$$

$$\mathbf{u}(t^{n-1}) = \mathbf{u}(t^n) - \delta t \mathbf{u}_t(t^n) + \frac{\delta t^2}{2} \mathbf{u}_{tt}(t^n) + \frac{1}{2} \int_{t^n}^{t^{n-1}} (t^{n-1} - t)^2 \mathbf{u}_{ttt}(t) dt, \quad (2.25)$$

and

$$\mathbf{u}_t(t^{n+1}) = \mathbf{u}_t(t^n) + \delta t \mathbf{u}_{tt}(t^n) + \int_{t^n}^{t^{n+1}} (t^{n+1} - t) \mathbf{u}_{ttt}(t) dt. \quad (2.26)$$

Hence (2.24)-(2.26) in (2.23) implies

$$\|\delta\mathcal{R}_0(t^{n+1})\|_0 \lesssim \delta t \int_{t^{n-1}}^{t^{n+1}} \|\mathbf{u}_{ttt}\|_0 dt.$$

Involving a Cauchy Schwarz inequality again, we obtain

$$\|\delta\mathcal{R}_0(t^{n+1})\|_0 \lesssim (\delta t)^{3/2} \left(\int_{t^{n-1}}^{t^{n+1}} \|\mathbf{u}_{ttt}\|_0^2 dt \right)^{1/2}. \quad \square$$

Taylor expansions are again used to derive estimates of the pressure increments $\delta p(t^{n+1})$ and $\delta^2 p(t^{n+1})$.

Lemma 2.2.3. For smooth enough p , there holds

$$\|\delta p(t^{n+1})\|_0 \leq \delta t^{1/2} \|p_t\|_{L^2(t^n, t^{n+1}; L^2(\Lambda))}$$

$$\|\delta^2 p(t^{n+1})\|_0 \leq \delta t^{3/2} \|p_{tt}\|_{L^2(t^{n-1}, t^{n+1}; L^2(\Lambda))}.$$

Proof. Again, a Taylor expansion gives

$$p(t^{n+1}) = p(t^n) + \int_{t^n}^{t^{n+1}} p_t(t) dt.$$

Proceeding as in Lemma 2.2.1 and Lemma 2.2.2, we deduce that

$$\|\delta p(t^{n+1})\|_0 \leq \delta t^{1/2} \left(\int_{t^n}^{t^{n+1}} \|p_t\|_0^2 dt \right)^{1/2},$$

which is the first estimate. To prove the second estimate, we use

$$p(t^{n+1}) = p(t^n) + \delta t p_t(t^n) + \int_{t^n}^{t^{n+1}} (t^{n+1} - t) p_{tt}(t) dt,$$

$$p(t^{n-1}) = p(t^n) - \delta t p_t(t^n) + \int_{t^{n-1}}^{t^n} (t^{n-1} - t) p_{tt}(t) dt,$$

and so

$$\|\delta^2 p(t^{n+1})\|_0 \leq (\delta t)^{3/2} \left(\int_{t^{n-1}}^{t^{n+1}} \|p_{tt}\|_0^2 dt \right)^{1/2}. \quad \square$$

We are now in position to derive an error estimate for the velocity. To begin, we introduce the notations:

$$\mathbf{e}^n := \mathbf{u}(t^n) - \mathbf{u}^n, \quad \pi^n := p(t^n) - p^n.$$

Theorem 2.2.2 (Velocity Error Estimate). The solution of (2.11)-(2.14) satisfies the error estimate:

$$\rho \|\mathbf{e}\|_{l^\infty(L^2(\Lambda))} + \mu \|\nabla^S \mathbf{e}\|_{l^2(L^2(\Lambda))} \lesssim \delta t.$$

provided \mathbf{u} and p smooth enough, and δt is sufficiently small.

Proof. We start by subtracting the equation (2.17) from (2.15) at time t^{n+1} . We find

$$\begin{aligned} \int_{\Lambda} \rho \left(\frac{\mathbf{e}^{n+1} - \mathbf{e}^n}{\delta t} \right) \mathbf{v} + \int_{\Lambda} 2\mu (\nabla^S \mathbf{e}^{n+1} : \nabla^S \mathbf{v}) - \int_{\Lambda} (p(t^{n+1}) - (p^n + \psi^n)) \operatorname{div}(\mathbf{v}) \\ = \int_{\Lambda} \rho \mathcal{R}_0(t^{n+1}) \mathbf{v}, \quad \forall \mathbf{v} \in [H_0^1(\Lambda)]^d, \end{aligned} \quad (2.27)$$

which is rewritten as

$$\begin{aligned} \int_{\Lambda} \rho \left(\frac{\mathbf{e}^{n+1} - \mathbf{e}^n}{\delta t} \right) \mathbf{v} + \int_{\Lambda} 2\mu (\nabla^S \mathbf{e}^{n+1} : \nabla^S \mathbf{v}) - \int_{\Lambda} (\pi^n)^* \operatorname{div}(\mathbf{v}) \\ = \int_{\Lambda} \mathcal{R}(t^{n+1}) \mathbf{v}, \end{aligned} \quad (2.28)$$

where $\mathcal{R}(t^{n+1}) := \rho \mathcal{R}_0(t^{n+1}) + \delta^2 p(t^{n+1})$ and $(\pi^n)^* = 2\pi^n - \pi^{n-1}$. Note that to obtain the previous expression, we used the relation

$$p(t^{n+1}) - 2p^n + p^{n-1} = (\pi^n)^* + \delta^2 p(t^{n+1}). \quad (2.29)$$

Also, subtracting (2.18) from (2.16) at time t^{n+1} leads to

$$\int_{\Lambda} \frac{\rho}{\delta t} \operatorname{div}(\mathbf{e}^{n+1}) q = \int_{\Lambda} \nabla \psi^{n+1} \nabla q, \quad \forall q \in H^1(\Lambda) \cap L_0^2(\Lambda). \quad (2.30)$$

Taking $\mathbf{v} = 2\delta t \mathbf{e}^{n+1}$ in (2.28) yields

$$\begin{aligned} \rho(\|\mathbf{e}^{n+1}\|_0^2 - \|\mathbf{e}^n\|_0^2 + \|\delta \mathbf{e}^{n+1}\|_0^2) + 4\delta t \mu \|\nabla^S \mathbf{e}^{n+1}\|_0^2 \\ = 2\delta t((\pi^n)^*, \operatorname{div}(\mathbf{e}^{n+1})) + 2\delta t(\mathcal{R}(t^{n+1}), \mathbf{e}^{n+1}). \end{aligned} \quad (2.31)$$

To estimate the first term in the right hand side of (2.31), we choose $q = 2\delta t^2(\pi^n)^*$ into (2.30), so that the identity $(\pi^n)^* = -\delta^2 \pi^{n+1} + \pi^{n+1}$ leads to

$$\begin{aligned} 2\delta t \rho(\operatorname{div}(\mathbf{e}^{n+1}), (\pi^n)^*) &= 2\delta t^2(\nabla \delta p(t^{n+1}) - \nabla \delta \pi^{n+1}, \nabla(\pi^n)^*) \\ &= 2\delta t^2(\nabla \delta p(t^{n+1}), \nabla(\pi^n)^*) - \delta t^2 \|\nabla \delta \pi^n\|_0^2 \\ &\quad + \delta t^2 \|\nabla \delta^2 \pi^{n+1}\|_0^2 - \delta t^2 \|\nabla \pi^{n+1}\|_0^2 + \delta t^2 \|\nabla \pi^n\|_0^2. \end{aligned} \quad (2.32)$$

Combining (2.32) with (2.31), we obtain

$$\begin{aligned} \rho\|\mathbf{e}^{n+1}\|_0^2 + \rho\|\delta \mathbf{e}^{n+1}\|_0^2 + 4\delta t \mu \|\nabla^S \mathbf{e}^{n+1}\|_0^2 + \frac{\delta t^2}{\rho} \|\nabla \pi^{n+1}\|_0^2 + \frac{\delta t^2}{\rho} \|\nabla \delta \pi^n\|_0^2 \\ \lesssim \rho\|\mathbf{e}^n\|_0^2 + \frac{\delta t^2}{\rho} \|\nabla \pi^n\|_0^2 + \frac{\delta t^2}{\rho} \|\nabla \delta^2 \pi^{n+1}\|_0^2 \\ + 2\frac{\delta t^2}{\rho}(\nabla \delta p(t^{n+1}), \nabla(\pi^n)^*) + 2\delta t(\mathcal{R}(t^{n+1}), \mathbf{e}^{n+1}). \end{aligned} \quad (2.33)$$

From the above estimate, we can observe that the last 3 terms at the right hand side still need additional bounds. First, to derive the estimate for the term $\frac{\delta t^2}{\rho} \|\nabla \delta^2 \pi^{n+1}\|_0^2$, we take the difference between two successive relations of (2.30) and take $q = \delta^2 \pi^{n+1}$.

After the integration by parts with applying the boundary condition (2.6), we get

$$-\rho(\delta \mathbf{e}^{n+1}, \nabla(\delta^2 \pi^{n+1})) = \delta t(\nabla \delta^2 p(t^{n+1}), \nabla \delta^2 \pi^{n+1}) - \delta t(\nabla \delta^2 \pi^{n+1}, \nabla \delta^2 \pi^{n+1}).$$

Multiple Cauchy Schwarz inequalities give

$$\frac{\delta t}{\rho} \|\nabla \delta^2 \pi^{n+1}\|_0 \leq \frac{\delta t}{\rho} \|\nabla \delta^2 p(t^{n+1})\|_0 + \|\delta \mathbf{e}^{n+1}\|_0. \quad (2.34)$$

Now, we apply a Young's inequality and Lemma 2.2.3 to get

$$\begin{aligned} \frac{\delta t^2}{\rho} \|\nabla \delta^2 \pi^{n+1}\|_0^2 &\leq \rho \|\delta \mathbf{e}^{n+1}\|_0^2 + \frac{\delta t^2}{\rho} \|\nabla \delta^2 p(t^{n+1})\|_0^2 + 2\delta t \|\nabla \delta^2 p(t^{n+1})\|_0 \|\delta \mathbf{e}^{n+1}\|_0 \\ &\lesssim \rho \|\delta \mathbf{e}^{n+1}\|_0^2 + \rho \delta t \|\mathbf{e}^{n+1}\|_0^2 + \rho \delta t \|\mathbf{e}^n\|_0^2 + \frac{\delta t^4}{\rho} \|\nabla p_{tt}\|_{L^2(t^{n-1}, t^{n+1}; L^2)}^2. \end{aligned} \quad (2.35)$$

The next term to consider is $2 \frac{\delta t^2}{\rho} (\nabla \delta p(t^{n+1}), \nabla(\pi^n)^*)$, which is estimated as follows

$$\begin{aligned} 2 \frac{\delta t^2}{\rho} (\nabla \delta p(t^{n+1}), \nabla(\pi^n)^*) &\leq 2 \frac{\delta t^2}{\rho} \|\nabla \delta p(t^{n+1})\|_0 \|\nabla(\pi^n)^*\|_0 \\ &\leq \frac{\delta t^2}{\rho} \int_{t^n}^{t^{n+1}} \|\nabla p_t\|_0^2 dt + \frac{1}{2} \frac{\delta t^3}{\rho} \|\nabla(\pi^n)^*\|_0^2 \\ &\leq \frac{\delta t^2}{\rho} \int_{t^n}^{t^{n+1}} \|\nabla p_t\|_0^2 dt + \frac{\delta t^3}{\rho} (\|\nabla \pi^n\|_0^2 + \|\nabla \delta \pi^n\|_0^2), \end{aligned} \quad (2.36)$$

after applying Lemma 2.2.3. The last term in the right hand side of (2.33) to estimate is $2\delta t(\mathcal{R}(t^{n+1}), \mathbf{e}^{n+1})$. Applying several inequalities such as Cauchy Schwarz,

Poincare, and Young's inequality with Lemma 2.2.1 and Lemma 2.2.3 leads to

$$\begin{aligned}
2\delta t(\mathcal{R}(t^{n+1}), \mathbf{e}^{n+1}) &= 2\delta t(\rho\mathcal{R}_0(t^{n+1}) + \delta^2 p(t^{n+1}), \mathbf{e}^{n+1}) \\
&\leq 2\delta t\rho\|\mathcal{R}_0(t^{n+1})\|_0\|\mathbf{e}^{n+1}\|_0 + 2\delta t\|\delta^2 p(t^{n+1})\|_0\|\mathbf{e}^{n+1}\|_0 \\
&\lesssim 2\delta t\rho\|\mathcal{R}_0(t^{n+1})\|_0\|\nabla\mathbf{e}^{n+1}\|_0 + 2\delta t\|\delta^2 p(t^{n+1})\|_0\|\nabla\mathbf{e}^{n+1}\|_0 \\
&\lesssim \delta t\rho\|\mathcal{R}_0(t^{n+1})\|_0^2 + 3\delta t\mu\|\nabla^S\mathbf{e}^{n+1}\|_0^2 + \delta t\|\delta^2 p(t^{n+1})\|_0^2 \\
&\lesssim \delta t^2\rho\int_{t^n}^{t^{n+1}}\|\mathbf{u}_{tt}\|_0^2 dt + 3\delta t\mu\|\nabla^S\mathbf{e}^{n+1}\|_0^2 + \delta t^4\int_{t^{n-1}}^{t^{n+1}}\|p_{tt}\|_0^2 dt.
\end{aligned} \tag{2.37}$$

Combining the estimate (2.35)-(2.37) with (2.33) yields

$$\begin{aligned}
\rho(1-\delta t)\|\mathbf{e}^{n+1}\|_0^2 + \delta t\mu\|\nabla^S\mathbf{e}^{n+1}\|_0^2 + \frac{\delta t^2}{\rho}\|\nabla\pi^{n+1}\|_0^2 + \frac{\delta t^2}{\rho}(1-\delta t)\|\nabla\delta\pi^n\|_0^2 \\
\lesssim \rho(1+\delta t)\|\mathbf{e}^n\|_0^2 + \frac{\delta t^2}{\rho}(1+\delta t)\|\nabla\pi^n\|_0^2 + \delta t^2\int_{t^n}^{t^{n+1}}\|\mathbf{u}_{tt}\|_0^2 dt \\
+ \delta t^2\int_{t^n}^{t^{n+1}}\|\nabla p_t\|_0^2 dt + \delta t^4\int_{t^{n-1}}^{t^{n+1}}\|p_{tt}\|_0^2 dt.
\end{aligned}$$

Summing the above relation for $n = 0, \dots, N-1$, we arrive at

$$\begin{aligned}
\rho(1-\delta t)\|\mathbf{e}^N\|_0^2 + \sum_{n=0}^{N-1}\delta t\mu\|\nabla^S\mathbf{e}^{n+1}\|_0^2 + \frac{\delta t^2}{\rho}\|\nabla\pi^N\|_0^2 + \sum_{n=0}^{N-1}\frac{\delta t^2}{\rho}(1-\delta t)\|\nabla\delta\pi^n\|_0^2 \\
\lesssim \rho(1-\delta t)\|\mathbf{e}^0\|_0^2 + 2\sum_{n=0}^{N-1}\delta t\|\mathbf{e}^n\|_0^2 + \frac{\delta t^2}{\rho}\|\nabla\pi^0\|_0^2 + \sum_{n=0}^{N-1}\frac{\delta t^3}{\rho}\|\nabla\pi^n\|_0^2 \\
+ \delta t^2\int_0^T\|\mathbf{u}_{tt}\|_0^2 dt + \delta t^2\int_0^T\|\nabla p_t\|_0^2 dt + \delta t^4\int_0^T\|p_{tt}\|_0^2 dt.
\end{aligned}$$

Finally applying the discrete Gronwall's lemma to the above relation and taking into account the initial estimates, $\|\mathbf{e}^0\|_0 = \|\mathbf{u}(t^0) - \mathbf{u}^0\|_0 = 0$ and $\|\pi^0\|_0 = \|p(t^0) - p^0\|_0 =$

0, we have

$$\rho \|\mathbf{e}^N\|_0^2 + \mu \sum_{n=0}^{N-1} \delta t \|\nabla^S \mathbf{e}^{n+1}\|_0^2 + \frac{\delta t^2}{\rho} \|\nabla \pi^N\|_0^2 + \sum_{n=0}^{N-1} \frac{\delta t^2}{\rho} (1 - \delta t) \|\nabla \delta \pi^n\|_0^2 \lesssim \delta t^2,$$

for sufficiently small δt . □

Before to discuss the error convergence rate of the velocity increment, we derive auxiliary lemmas.

Lemma 2.2.4. Assuming \mathbf{u} is smooth enough, then

$$\|\mathcal{R}_0(t^1)\|_0^2 \lesssim \delta t^2.$$

Proof. Taylor expansion yields

$$\mathbf{u}(t^0) = \mathbf{u}(t^1) - \delta t \mathbf{u}_t(t^1) + \delta t^2 \frac{1}{2} \mathbf{u}_{tt}(t^1) - \frac{1}{2} \int_{t^0}^{t^1} (t^0 - t)^2 \mathbf{u}_{ttt}(t) dt,$$

and by a Cauchy Schwarz estimate we obtain

$$\|\mathcal{R}_0(t^1)\|_0^2 \leq \delta t^2 \|\mathbf{u}_{tt}(t^1)\|_0^2 + \delta t^2 \int_{t^0}^{t^1} \|\mathbf{u}_{ttt}\|_0^2 dt. \quad \square$$

Lemma 2.2.5. Assuming p smooth enough, it holds:

$$\|\delta p(t^1)\|_0^2 \lesssim \delta t^2.$$

Proof. Again a Taylor expansion yields

$$p(t^1) = p(t^0) + \delta t p_t(t^0) + \int_{t^0}^{t^1} (t^1 - t) p_{tt}(t) dt,$$

and it follows a Cauchy Schwarz inequality to get,

$$\|\delta p(t^1)\|_0^2 \leq \delta t^2 \|p_t(t^0)\|_0^2 + \delta t^2 \int_{t^0}^{t^1} \|p_{tt}\|_0^2 dt. \quad \square$$

Lemma 2.2.6. Under the same assumptions of Theorem 2.2.2, we have

$$\rho \|\mathbf{e}^1\|_0^2 + \rho \|\delta \mathbf{e}^1\|_0^2 \lesssim \delta t^4.$$

Proof. Taking $\mathbf{v} = 2\delta t \mathbf{e}^1$ in (2.28) when $n = 0$ leads to

$$\rho \|\mathbf{e}^1\|_0^2 + \rho \|\delta \mathbf{e}^1\|_0^2 + 4\delta t \mu \|\nabla^S \mathbf{e}^1\|_0^2 = 2\delta t (\rho \mathcal{R}_0(t^1) + \delta p(t^1), \mathbf{e}^1).$$

We can estimate the right hand side as follows

$$\begin{aligned} 2\delta t (\rho \mathcal{R}_0(t^1) + \delta p(t^1), \mathbf{e}^1) &\leq 2\delta t \rho \|\mathcal{R}_0(t^1)\|_0 \|\mathbf{e}^1\|_0 + 2\delta t \|\delta p(t^1)\|_0 \|\mathbf{e}^1\|_0 \\ &\lesssim \frac{\rho}{2} \|\mathbf{e}^1\|_0^2 + \rho \delta t^2 \|\mathcal{R}_0(t^1)\|_0^2 + \delta t^2 \|\delta p(t^1)\|_0^2. \end{aligned}$$

Involving Lemma 2.2.4 and Lemma 2.2.5, we deduce

$$\frac{\rho}{2} \|\mathbf{e}^1\|_0^2 + \rho \|\delta \mathbf{e}^1\|_0^2 + 4\delta t \mu \|\nabla^S \mathbf{e}^1\|_0^2 \lesssim \delta t^4. \quad \square$$

Lemma 2.2.7. Under the same assumptions of Theorem 2.2.2, we have

$$\|\nabla \delta \pi^1\|_0^2 \lesssim \delta t^2.$$

Proof. Taking $q = \delta \pi^1$ into (2.30) with $n = 0$ and a Cauchy Schwarz estimate yields

$$\|\nabla \delta \pi^1\|_0^2 \lesssim \frac{\rho}{\delta t^2} \|\mathbf{e}^1\|_0^2 + \|\nabla \delta p(t^1)\|_0^2.$$

Thus by applying Lemma 2.2.5 and Lemma 2.2.6, we get

$$\|\nabla\delta\pi^1\|_0^2 \lesssim \delta t^2. \quad \square$$

Corollary 2.2.1 (Velocity Increment Error Estimate). Under the same assumptions of Theorem 2.2.2, we have

$$\begin{aligned} \rho\|\delta\mathbf{e}\|_{l^\infty(L^2(\Lambda))}^2 + \mu\|\nabla^S\delta\mathbf{e}\|_{l^2(L^2(\Lambda))}^2 &\lesssim \rho\|\delta\mathbf{e}^1\|_0^2 + \delta t^2\|\nabla\delta\pi^1\|_0^2 \\ &\lesssim \delta t^4 \end{aligned}$$

Proof. The proof of this Corollary follows the same principle as that we used in Theorem 2.2.2. The only difference in here is that, it consists in working with the time increments $\delta\mathbf{e}^{n+1}$, but we can easily deal with this by taking the time increment of the scheme (2.28) and (2.30). The estimate for the right hand side terms are provided by the previous Lemmas. \square

Lemma 2.2.8 (Estimate on Increments). Using the result of velocity increment error estimate, we can derive the velocity increment stability estimate such as:

$$\sum_{n=0}^{N-1} \|\delta\mathbf{u}^{n+1}\|_0^2 \lesssim \delta t,$$

provided \mathbf{u} smooth enough.

Proof. Using the relation $\delta\mathbf{u}^{n+1} = -\delta\mathbf{e}^{n+1} + \delta\mathbf{u}(t^{n+1})$, we obtain

$$\|\delta\mathbf{u}^{n+1}\|_0 \leq \|\delta\mathbf{e}^{n+1}\|_0 + \|\delta\mathbf{u}(t^{n+1})\|_0.$$

Squaring both sides and summing up for $n = 0, \dots, N - 1$ yield

$$\begin{aligned} \sum_{n=0}^{N-1} \|\delta \mathbf{u}^{n+1}\|_0^2 &\lesssim \sum_{n=0}^{N-1} \|\delta \mathbf{e}^{n+1}\|_0^2 + \sum_{n=0}^{N-1} \|\delta \mathbf{u}(t^{n+1})\|_0^2 \\ &\lesssim \delta t \|\mathbf{u}_t\|_{L^2(0,T;L^2(\Lambda))}^2, \end{aligned}$$

after applying Lemma 2.2.3 and Corollary 2.2.1. □

We focus now on the pressure stability and convergence.

Theorem 2.2.3 (Pressure Stability). Set $\mathbf{f} = \mathbf{0}$ in (2.11), then there holds

$$\|p\|_{L^2(\Lambda)} \leq C$$

with a positive constant C independent of n .

Proof. There exists $\beta > 0$ such that for any function $q \in L^2(\Lambda)$, there holds

$$\|q\|_{L^2(\Lambda)} \leq \beta \cdot \sup_{\mathbf{v} \in [H^1(\Lambda)]^d} \frac{(q, \operatorname{div}(\mathbf{v}))}{\|\mathbf{v}\|_1}. \quad (2.38)$$

This property is known as the inf-sup condition (cf. [24, 49]). Choosing $q = p^n + \psi^n$ and using (2.17) we have

$$\|p^n + \psi^n\|_0 \lesssim \frac{\rho}{\delta t} \|\delta \mathbf{u}^{n+1}\|_0 + 2\mu \|\nabla^S \mathbf{u}^{n+1}\|_0.$$

Squaring both sides and multiplying δt and the above relation gives

$$\delta t \|p^n + \psi^n\|^2 \lesssim \frac{\rho}{\delta t} \|\delta \mathbf{u}^{n+1}\|_0^2 + \delta t \mu \|\nabla^S \mathbf{u}^{n+1}\|_0^2.$$

Now summing for $n = 0$ to $n = N - 1$ leads to

$$\sum_{n=0}^{N-1} \delta t \|p^n + \psi^n\|^2 \lesssim \frac{\rho}{\delta t} \sum_{n=0}^{N-1} \|\delta \mathbf{u}^{n+1}\|_0^2 + \sum_{n=0}^{N-1} \delta t \mu \|\nabla^S \mathbf{u}^{n+1}\|_0^2.$$

Lemma 2.2.8 and Theorem 2.2.1 conclude the proof. \square

Theorem 2.2.4 (Pressure Error Estimate). The pressure solution of (2.11)-(2.14) satisfies the error estimate:

$$\|\pi\|_{l^2(L^2(\Lambda))} \lesssim \delta t$$

provided \mathbf{u} and p smooth enough.

Proof. We use the extrapolation $(\pi^n)^\star = 2\pi^n - \pi^{n-1}$ to derive the result. By choosing $q = (\pi^n)^\star$ in (2.38) we obtain,

$$\|(\pi^n)^\star\|_0 \lesssim \frac{\rho}{\delta t} \|\delta \mathbf{e}^{n+1}\|_0 + 2\mu \|\nabla^S \mathbf{e}^{n+1}\|_0 + \rho \|\mathcal{R}_0(t^{n+1})\|_0 + \|\delta^2 p(t^{n+1})\|_0.$$

Taking squares on both sides and multiplying by δt imply

$$\delta t \|(\pi^n)^\star\|_0^2 \lesssim \frac{\rho}{\delta t} \|\delta \mathbf{e}^{n+1}\|_0^2 + \mu \delta t \|\nabla^S \mathbf{e}^{n+1}\|_0^2 + \delta t \|\mathcal{R}_0(t^{n+1})\|_0^2 + \delta t \|\delta^2 p(t^{n+1})\|_0^2.$$

Now summing for $n = 0$ to $n = N - 1$ leads to

$$\begin{aligned} \sum_{n=0}^{N-1} \delta t \|(\pi^n)^\star\|_0^2 &\lesssim \sum_{n=0}^{N-1} \frac{\rho}{\delta t} \|\delta \mathbf{e}^{n+1}\|_0^2 + \sum_{n=0}^{N-1} \delta t \mu \|\nabla^S \mathbf{e}^{n+1}\|_0^2 + \delta t^2 \int_0^T \|\mathbf{u}_{tt}\|_0^2 dt + \delta t^4 \int_0^T \|p_{tt}\|_0^2 dt \\ &\lesssim \delta t^2, \end{aligned}$$

involving Corollary 2.2.1 and Theorem 2.2.2. \square

δt	$\ \pi\ _{l^2(L^2(\Lambda))}$	Rate	$\ \mathbf{e}\ _{l^2(H^1(\Lambda))}$	Rate
0.025000	0.00745802	1.4154	0.00383904	1.5703
0.012500	0.00311459	1.2598	0.00128411	1.5800
0.006250	0.00146674	1.0864	0.00044933	1.5149
0.003125	0.00072829	1.0100	0.00016856	1.4145

Table 2.1: Error vs. δt : Standard first order Euler scheme.

δt	$\ \pi\ _{l^2(L^2(\Lambda))}$	Rate	$\ \mathbf{e}\ _{l^2(H^1(\Lambda))}$	Rate
0.02500	0.00346123	1.6060	0.00180106	1.6523
0.01250	0.00105156	1.7187	0.00053403	1.7538
0.00625	0.00031129	1.7562	0.00015379	1.7960
0.003125	0.00009231	1.7536	0.00004434	1.7943

Table 2.2: Error vs. δt : Rotational BDF2 second order scheme.

2.2.2 Numerical results

To illustrate the optimality of the proposed algorithm, we consider the exact solution

$$\mathbf{u}(x, y, t) := \begin{pmatrix} \sin(t+x) \sin(t+y) \\ \cos(t+x) \cos(t+y) \end{pmatrix}, \quad p(x, y, t) = \sin(t+x-y),$$

defined on $\Lambda := (0, 1)^2$, and the final time $T = 1$. To approximate the velocity and the pressure, we use the Taylor-Hood($\mathbb{Q}_2, \mathbb{Q}_1$) finite elements. The space discretization is chosen fine enough not to interfere with the time discretization error. The behavior of the errors in velocity and pressure approximations versus the time step δt used are given in Table 2.1. The optimal order of convergence $\mathcal{O}(\delta t)$ is observed for the $l^2(L^2(\Lambda))$ norm of the pressure and little more than expected for $l^2(H^1(\Lambda))$ norm of the velocity.

The rotational incremental method introduced in [51] yields an error decay of the order of $\mathcal{O}(\delta t^{3/2})$, see Table 2.2. The main idea of rotational increment is based on the simple observation that

$$\Delta \mathbf{u} = \nabla \operatorname{div}(\mathbf{u}) - \nabla \times \nabla \times \mathbf{u}.$$

By using the above relation, the pressure correction step (2.14) is modified to

$$p^{n+1} = p^n + \psi^{n+1} - \mu \operatorname{div}(\mathbf{u}^{n+1}).$$

The discretization of the time derivative, $\frac{1}{\delta t}(\mathbf{u}^{n+1} - \mathbf{u}^n)$ in (2.11), is replaced by a Backward Differentiation Formula 2(BDF2) formula

$$\frac{1}{2\delta t}(3\mathbf{u}^{n+1} - 4\mathbf{u}^n + \mathbf{u}^{n-1})$$

in order to take full advantage of the higher order method. Table 2.2 illustrate the convergence of the rotational method and in particular the decay of the error in $l^2(L^2(\Lambda))$ norm for the pressure and $l^2(H^1(\Lambda))$ norm for the velocity.

2.3 Optimal Incremental Pressure Correction Projection Method for open boundary problem

Now, based on the previous section, we design and study two different modifications of the first order standard incremental pressure correction projection scheme for the Stokes system. The first modification will be discussed in this section.

The scheme proposed in [33] when the system is subject to open boundary conditions, see (2.41), is suboptimal with respect to the time discretization parameter. Thus, we propose and study a new scheme which ables to recover the optimal con-

vergence rate by modifying the pressure increment boundary condition.

From here, we consider the Stokes system of (2.1)-(2.2) supplemented with the force condition at the boundary (2.41). For clarity, we also denote by ψ^n the pressure increment approximation, i.e.

$$p^n = p^{n-1} + \psi^n. \quad (2.39)$$

Together with an initial condition on the velocity $\mathbf{u}^0 = \mathbf{u}_0$, the algorithm requires an initial pressure $p(0) \in L_0^2(\Lambda)$ and we set $p^{-1} = p^0 = p(0)$, so that $\psi^0 = 0$. Recursively we seek the velocity \mathbf{u}^{n+1} and the pressure p^{n+1} in three steps. First, given \mathbf{u}^n , ψ^n and p^n , the velocity approximation at t^{n+1} is given by

$$\rho \frac{\mathbf{u}^{n+1} - \mathbf{u}^n}{\delta t} - 2\operatorname{div}(\mu \nabla^S \mathbf{u}^{n+1}) + \nabla(p^n + \psi^n) - \alpha \nabla \operatorname{div} \left(\frac{\mathbf{u}^{n+1} - \mathbf{u}^n}{\delta t} \right) = \mathbf{f}(\cdot, t^{n+1}) \quad (2.40)$$

in Λ , where $\alpha \geq 1$ is a stabilization parameter. As we shall see, the consistent ‘grad-div’ term is instrumental to ensure the stability of the scheme by providing a control on $\|\psi^{n+1} - \psi^n\|_{H^1(\Lambda)}$, i.e. the second increment of the pressure; see (2.49). Equation (2.40) is supplemented by the boundary condition

$$\left(2\mu \nabla^S \mathbf{u}^{n+1} - (p^n + \psi^n) + \alpha \operatorname{div} \left(\frac{\mathbf{u}^{n+1} - \mathbf{u}^n}{\delta t} \right) \right) \boldsymbol{\nu} = 0 \quad \text{on } \partial\Lambda. \quad (2.41)$$

The second step consist in seeking the new pressure increment approximation ψ^{n+1} which is the solution to

$$-\delta t \Delta \psi^{n+1} + \delta t \psi^{n+1} = -\operatorname{div}(\mathbf{u}^{n+1}) \quad \text{in } \Lambda, \quad (2.42)$$

together with the boundary condition

$$\frac{\partial}{\partial \boldsymbol{\nu}} \psi^{n+1} = 0 \quad \text{on } \partial\Lambda. \quad (2.43)$$

Finally, the pressure approximation is then given by (2.39). Note that ρ does not appear in (2.42) as it was in (2.12).

The novelty of this projection scheme is to impose a Neumann boundary condition on the pressure increment (and therefore on the pressure). Its aim is to reduce the boundary layer on the pressure and improve the convergence rate. Compare with [33] where a Dirichlet condition $p^{n+1} = p^n$ is proposed on the pressure. This is at the expense of adding (i) an harmless zero order term $\delta t \psi^{n+1}$ in (2.42) to be able to recover the full $H^1(\Lambda)$ norm for the pressure and (ii) the more serious ‘grad-div’ stabilization term in (2.40), which complicates the linear algebra. Notice that the boundary condition (2.43) proposed here corresponds to the standard boundary condition when the velocity is imposed at the boundary; refer to [33].

2.3.1 Stability and error estimate

We start from deriving the variational form of (2.40) and (2.42) by taking $L^2(\Lambda)$ inner product with corresponding test functions and applying the boundary conditions (2.41) and (2.43), to cancel the boundary term appearing after the integration by parts. Thus, $\mathbf{u}^{n+1} \in [H^1(\Lambda)]^d$ solves

$$\begin{aligned} \int_{\Lambda} \rho \left(\frac{\mathbf{u}^{n+1} - \mathbf{u}^n}{\delta t} \right) \cdot \mathbf{v} + \int_{\Lambda} 2\mu (\nabla^S \mathbf{u}^{n+1} : \nabla^S \mathbf{v}) - \int_{\Lambda} (p^n + \psi^n) \operatorname{div}(\mathbf{v}) \\ + \alpha \int_{\Lambda} \operatorname{div} \left(\frac{\mathbf{u}^{n+1} - \mathbf{u}^n}{\delta t} \right) \operatorname{div}(\mathbf{v}) = \int_{\Lambda} \mathbf{f}(\cdot, t^{n+1}) \cdot \mathbf{v}, \quad \forall \mathbf{v} \in [H^1(\Lambda)]^d, \end{aligned} \quad (2.44)$$

and $\psi^{n+1} \in H^1(\Lambda)$ solves

$$-\int_{\Lambda} \nabla \psi^{n+1} \nabla q - \int_{\Lambda} \psi^{n+1} q = \int_{\Lambda} \frac{1}{\delta t} \operatorname{div}(\mathbf{u}^{n+1}) q, \quad \forall q \in H^1(\Lambda). \quad (2.45)$$

We now discuss the stability and error estimates for the scheme (2.44)-(2.45).

Theorem 2.3.1 (Velocity Stability). Set $\mathbf{f} = \mathbf{0}$ in (2.44) and assume $\alpha \geq 1$, then there holds

$$\begin{aligned} \rho \|\mathbf{u}\|_{l^\infty(L^2(\Lambda))}^2 + 4\mu \|\nabla^S \mathbf{u}\|_{l^2(L^2(\Lambda))}^2 + \alpha \|\operatorname{div}(\mathbf{u})\|_{l^\infty(L^2(\Lambda))}^2 + (\delta t)^2 \|p\|_{l^\infty(H^1(\Lambda))}^2 \\ \leq \rho \|\mathbf{u}_0\|_0^2 + \alpha \|\operatorname{div}(\mathbf{u}_0)\|_0^2 + (\delta t)^2 \|p_0\|_1^2, \end{aligned}$$

provided $\mathbf{u}_0 \in [L^2(\Lambda)]^d$, $\operatorname{div}(\mathbf{u}_0) \in L^2(\Lambda)$ and $p_0 \in H^1(\Lambda)$.

Proof. Choosing $\mathbf{v} = 2\delta t \mathbf{u}^{n+1}$ in (2.44), we get

$$\begin{aligned} \rho \left(\|\mathbf{u}^{n+1}\|_0^2 + \|\mathbf{u}^{n+1} - \mathbf{u}^n\|_0^2 - \|\mathbf{u}^n\|_0^2 \right) + 4\delta t \mu \|\nabla^S \mathbf{u}^{n+1}\|_0^2 \\ + \alpha \left(\|\operatorname{div}(\mathbf{u}^{n+1})\|_0^2 + \|\operatorname{div}(\mathbf{u}^{n+1} - \mathbf{u}^n)\|_0^2 - \|\operatorname{div}(\mathbf{u}^n)\|_0^2 \right) \\ - 2\delta t (p^n + \psi^n, \operatorname{div}(\mathbf{u}^{n+1})) = 0. \end{aligned} \quad (2.46)$$

The last term in the left hand side of the above relation is estimated upon taking $q = 2\delta t^2(p^n + \psi^n)$ in (2.45) to get,

$$-2\delta t (p^n + \psi^n, \operatorname{div}(\mathbf{u}^{n+1})) = 2(\delta t)^2 (\nabla \psi^{n+1}, \nabla (p^n + \psi^n)) + 2(\delta t)^2 (\psi^{n+1}, p^n + \psi^n).$$

In view of (2.39), we write $p^n + \psi^n = \psi^n - \psi^{n+1} + p^{n+1}$ and realize that

$$\begin{aligned} -2\delta t ((p^n + \psi^n), \operatorname{div}(\mathbf{u}^{n+1})) &= (\delta t)^2 \|\psi^n\|_1^2 - (\delta t)^2 \|\psi^{n+1} - \psi^n\|_1^2 \\ &+ (\delta t)^2 \|p^{n+1}\|_1^2 - (\delta t)^2 \|p^n\|_1^2. \end{aligned} \quad (2.47)$$

It remains to derive a bound for $\|\psi^{n+1} - \psi^n\|_1$. Taking the difference of two successive relations of (2.45), and choosing $q = \psi^{n+1} - \psi^n$ yields

$$\delta t \|\psi^{n+1} - \psi^n\|_1^2 = -(\operatorname{div}(\mathbf{u}^{n+1} - \mathbf{u}^n), (\psi^{n+1} - \psi^n)). \quad (2.48)$$

Hence, we deduce that

$$\delta t \|\psi^{n+1} - \psi^n\|_1 \leq \|\operatorname{div}(\mathbf{u}^{n+1} - \mathbf{u}^n)\|_0. \quad (2.49)$$

Gathering the estimate (2.46),(2.47), and (2.49) we obtain

$$\begin{aligned} & \rho \left(\|\mathbf{u}^{n+1}\|_0^2 + \|\mathbf{u}^{n+1} - \mathbf{u}^n\|_0^2 - \|\mathbf{u}^n\|_0^2 \right) + 4\delta t \mu \|\nabla^S \mathbf{u}^{n+1}\|_0^2 \\ & + \alpha \left(\|\operatorname{div}(\mathbf{u}^{n+1})\|_0^2 - \|\operatorname{div}(\mathbf{u}^n)\|_0^2 \right) + (\alpha - 1) \|\operatorname{div}(\mathbf{u}^{n+1} - \mathbf{u}^n)\|_0^2 \\ & + (\delta t)^2 \left(\|p^{n+1}\|_1^2 - \|p^n\|_1^2 + \|\psi^n\|_1^2 \right) \leq 0. \end{aligned}$$

The desired bound follows after summing for $n = 0$ to $N - 1$. □

We emphasize that the above proof is closely related to the case where Dirichlet boundary conditions are imposed on the velocity; refer for instance to [30, 34]. The difference resides on the fact that (2.49) can be circumvented using an integration by parts in (2.48). Hence following the techniques developed for the Dirichlet case together with the argumentation leading to (2.49) yields the optimal convergence rates.

Theorem 2.3.2 (Velocity Error Estimate). The velocity solution of (2.44)-(2.45) satisfies the error estimate:

$$\rho \|\mathbf{e}\|_{l^\infty(L^2(\Lambda))}^2 + \mu \|\nabla^S \mathbf{e}\|_{l^2(L^2(\Lambda))}^2 + \alpha \|\operatorname{div}(\mathbf{e})\|_{l^\infty(L^2(\Lambda))}^2 \lesssim (\delta t)^2,$$

provided \mathbf{u} and p smooth enough, and δt sufficiently small.

Proof. We start by subtracting (2.44) from (2.15) at time t^{n+1} to get,

$$\begin{aligned} & \int_{\Lambda} \rho \left(\frac{\mathbf{e}^{n+1} - \mathbf{e}^n}{\delta t} \right) \mathbf{v} + \int_{\Lambda} 2\mu (\nabla^S \mathbf{e}^{n+1} : \nabla^S \mathbf{v}) - \int_{\Lambda} (p(t^{n+1}) - (p^n)^*) \operatorname{div}(\mathbf{v}) \\ & + \alpha \int_{\Lambda} \operatorname{div} \left(\frac{\mathbf{e}^{n+1} - \mathbf{e}^n}{\delta t} \right) \operatorname{div}(\mathbf{v}) = \int_{\Lambda} (\rho \mathcal{R}_0(t^{n+1}) + \alpha \mathcal{R}_1(t^{n+1})) \mathbf{v}, \quad \forall \mathbf{v} \in [H^1(\Lambda)]^d, \end{aligned} \quad (2.50)$$

where $\mathcal{R}_0(t^{n+1})$ is defined in (2.21), and

$$\begin{aligned} \mathcal{R}_1(t^{n+1}) & := \nabla \operatorname{div} \left(\frac{\mathbf{u}(t^{n+1}) - \mathbf{u}(t^n)}{\delta t} \right) - \nabla \operatorname{div}(\mathbf{u}_t(t^{n+1})) \\ & = \nabla \operatorname{div}(\mathcal{R}_0(t^{n+1})). \end{aligned}$$

In addition, (2.29) allows to rewrite (2.50) as

$$\begin{aligned} & \int_{\Lambda} \rho \left(\frac{\mathbf{e}^{n+1} - \mathbf{e}^n}{\delta t} \right) \mathbf{v} + \int_{\Lambda} 2\mu (\nabla^S \mathbf{e}^{n+1} : \nabla^S \mathbf{v}) - \int_{\Lambda} (\pi^n)^* \operatorname{div}(\mathbf{v}) \\ & + \alpha \int_{\Lambda} \operatorname{div} \left(\frac{\mathbf{e}^{n+1} - \mathbf{e}^n}{\delta t} \right) \operatorname{div}(\mathbf{v}) = \int_{\Lambda} \mathcal{R}(t^{n+1}) \mathbf{v}, \quad \forall \mathbf{v} \in [H^1(\Lambda)]^d, \end{aligned} \quad (2.51)$$

where

$$\mathcal{R}(t^{n+1}) := \rho \mathcal{R}_0(t^{n+1}) + \alpha \mathcal{R}_1(t^{n+1}) + \delta^2 p(t^{n+1}).$$

We subtract (2.45) from (2.16) at time t^{n+1} to derive

$$\int_{\Lambda} \frac{1}{\delta t} \operatorname{div}(\mathbf{e}^{n+1}) q = \int_{\Lambda} \nabla \psi^{n+1} \nabla q + \int_{\Lambda} \psi^{n+1} q, \quad \forall q \in H^1(\Lambda). \quad (2.52)$$

Taking $\mathbf{v} = 2\delta t \mathbf{e}^{n+1}$ in (2.51) we get

$$\begin{aligned} & \rho(\|\mathbf{e}^{n+1}\|_0^2 - \|\mathbf{e}^n\|_0^2 + \|\delta \mathbf{e}^{n+1}\|_0^2) + 4\delta t \mu \|\nabla^S \mathbf{e}^{n+1}\|_0^2 \\ & \quad + \alpha(\|\operatorname{div}(\mathbf{e}^{n+1})\|_0^2 - \|\operatorname{div}(\mathbf{e}^n)\|_0^2 + \|\operatorname{div}(\delta \mathbf{e}^{n+1})\|_0^2) \\ & \quad = 2\delta t((\pi^n)^\star, \operatorname{div}(\mathbf{e}^{n+1})) + 2\delta t(\mathcal{R}(t^{n+1}), \mathbf{e}^{n+1}). \end{aligned} \quad (2.53)$$

To estimate the first term in the right hand side of (2.53), we choose $q = \delta^2(\pi^n)^\star$ in (2.52), so that the identity $\psi^n = \delta p(t^n) - \delta \pi^n$ leads to

$$\begin{aligned} 2\delta t(\operatorname{div}(\mathbf{e}^{n+1}), (\pi^n)^\star) &= 2\delta t^2(\nabla(\delta p(t^{n+1})), \nabla(\pi^n)^\star) - 2\delta t^2(\nabla(\delta \pi^{n+1}), \nabla(\pi^n)^\star) \\ & \quad + 2\delta t^2(\delta p(t^{n+1}), (\pi^n)^\star) - 2\delta t^2(\delta \pi^{n+1}, (\pi^n)^\star). \end{aligned}$$

Noting that $(\pi^n)^\star = \pi^{n+1} - \delta^2 \pi^{n+1}$ and $\delta^2 \pi^{n+1} = \delta \pi^{n+1} - \delta \pi^n$, we get

$$\begin{aligned} 2\delta t(\operatorname{div}(\mathbf{e}^{n+1}), (\pi^n)^\star) + \delta t^2(\|\pi^{n+1}\|_1^2 + \|\delta \pi^n\|_1^2) &= \delta t^2(\|\pi^n\|_1^2 + \|\delta^2 \pi^{n+1}\|_1^2) \\ & \quad + 2\delta t^2(\delta \nabla p(t^{n+1}), \nabla(\pi^n)^\star) + 2\delta t^2(\delta p(t^{n+1}), (\pi^n)^\star). \end{aligned} \quad (2.54)$$

Combining relations (2.53) and (2.54), we obtain

$$\begin{aligned} & \rho(\|\mathbf{e}^{n+1}\|_0^2 - \|\mathbf{e}^n\|_0^2 + \|\delta \mathbf{e}^{n+1}\|_0^2) + 4\delta t \mu \|\nabla^S \mathbf{e}^{n+1}\|_0^2 + \delta t^2(\|\pi^{n+1}\|_1^2 + \|\delta \pi^n\|_1^2) \\ & \quad + \alpha(\|\operatorname{div}(\mathbf{e}^{n+1})\|_0^2 - \|\operatorname{div}(\mathbf{e}^n)\|_0^2 + \|\operatorname{div}(\delta \mathbf{e}^{n+1})\|_0^2) = \delta t^2(\|\pi^n\|_1^2 + \|\delta^2 \pi^{n+1}\|_1^2) \\ & \quad + 2\delta t(\mathcal{R}(t^{n+1}), \mathbf{e}^{n+1}) + 2\delta t^2(\nabla \delta p(t^{n+1}), \nabla(\pi^n)^\star) + 2\delta t^2(\delta p(t^{n+1}), (\pi^n)^\star). \end{aligned} \quad (2.55)$$

We now estimate each terms in the right hand side of (2.55) separately.

1) $\delta t^2 \|\delta^2 \pi^{n+1}\|_1^2$: We take the difference between two successive relations of (2.52)

and take $q = \delta^2 \pi^{n+1}$ to get,

$$\delta t \|\delta^2 \pi^{n+1}\|_1^2 = -(\operatorname{div}(\delta \mathbf{e}^{n+1}), \delta^2 \pi^{n+1}) + \delta t (\nabla \delta^2 p(t^{n+1}), \nabla \delta^2 \pi^{n+1}) + \delta t (\delta^2 p(t^{n+1}), \delta^2 \pi^{n+1}).$$

Cauchy Schwarz estimate yields

$$\delta t \|\delta^2 \pi^{n+1}\|_1 \leq \|\operatorname{div}(\delta \mathbf{e}^{n+1})\|_0 + \delta t \|\delta^2 p(t^{n+1})\|_1,$$

and squaring both side gives,

$$\delta t^2 \|\delta^2 \pi^{n+1}\|_1^2 \leq \|\operatorname{div}(\delta \mathbf{e}^{n+1})\|_0^2 + \delta t^2 \|\delta^2 p(t^{n+1})\|_1^2 + 2\delta t \|\operatorname{div}(\delta \mathbf{e}^{n+1})\|_0 \|\delta^2 p(t^{n+1})\|_1.$$

Applying Young's inequality to the last term above derives,

$$\begin{aligned} 2\delta t \|\operatorname{div} \delta \mathbf{e}^{n+1}\|_0 \|\delta^2 p(t^{n+1})\|_1 &\leq \frac{1}{4} \delta t \|\operatorname{div}(\delta \mathbf{e}^{n+1})\|_0^2 + \delta t \|\delta^2 p(t^{n+1})\|_1^2 \\ &\leq \frac{1}{2} \delta t \|\operatorname{div}(\mathbf{e}^{n+1})\|_0^2 + \frac{1}{2} \delta t \|\operatorname{div}(\mathbf{e}^n)\|_0^2 + \delta t \|\delta^2 p(t^{n+1})\|_1^2. \end{aligned}$$

Thus Lemma 2.2.3 yields

$$\begin{aligned} \delta t^2 \|\delta^2 \pi^{n+1}\|_1^2 &\leq \|\operatorname{div}(\delta \mathbf{e}^{n+1})\|_0^2 + \frac{1}{2} \delta t \|\operatorname{div}(\mathbf{e}^{n+1})\|_0^2 \\ &\quad + \frac{1}{2} \delta t \|\operatorname{div}(\mathbf{e}^n)\|_0^2 + \delta t^4 \|p\|_{L^2(t^{n-1}, t^{n+1}; H^1)}^2. \end{aligned} \quad (2.56)$$

Note that the above estimate is where the additional stabilization term,

$$-\alpha \nabla \operatorname{div} \left(\frac{\mathbf{u}^{n+1} - \mathbf{u}^n}{\delta t} \right)$$

is required.

2) $2\delta t^2(\nabla\delta p(t^{n+1}), \nabla(\pi^n)^\star) + 2\delta t^2(\delta p(t^{n+1}), (\pi^n)^\star)$: By using Cauchy Schwarz and Young's inequality with Lemma 2.2.3 we get

$$\begin{aligned} 2\delta t^2(\nabla\delta p(t^{n+1}), \nabla(\pi^n)^\star) &\leq 2\delta t^2\|\nabla\delta p(t^{n+1})\|_0\|\nabla(\pi^n)^\star\|_0 \\ &\leq \delta t^2 \int_{t^n}^{t^{n+1}} \|\nabla p_t\|_0^2 dt + \frac{\delta t^3}{2} \|\nabla(\pi^n)^\star\|_0 \\ &\leq \delta t^2 \int_{t^n}^{t^{n+1}} \|\nabla p_t\|_0^2 dt + \delta t^3(\|\nabla\pi^n\|_0^2 + \|\nabla(\delta\pi^n)\|_0^2), \end{aligned}$$

Similarly, we have

$$2\delta t^2(\delta p(t^{n+1}), (\pi^n)^\star) \leq \delta t^2 \int_{t^n}^{t^{n+1}} \|p_t\|_0^2 dt + \delta t^3(\|\pi^n\|_0^2 + \|\delta\pi^n\|_0^2),$$

so that

$$2\delta t^2(\nabla\delta p(t^{n+1}), \nabla(\pi^n)^\star) + 2\delta t^2(\delta p(t^{n+1}), (\pi^n)^\star) \leq \delta t^2 \int_{t^n}^{t^{n+1}} \|p_t\|_1^2 dt + \delta t^3(\|\pi^n\|_1^2 + \|\delta\pi^n\|_1^2).$$

3) $2\delta t(\mathcal{R}(t^{n+1}), \mathbf{e}^{n+1})$: The regularity term is bounded by using Cauchy Schwarz, Young's inequality, Lemma 2.2.1, and Lemma 2.2.3. We have

$$\begin{aligned} 2\delta t\rho(\mathcal{R}_0(t^{n+1}), \mathbf{e}^{n+1}) &\leq 4\delta t^2\rho \int_{t^n}^{t^{n+1}} \|\mathbf{u}_{tt}\|_0^2 dt + \frac{\rho}{4}\delta t\|\mathbf{e}^{n+1}\|_0^2, \\ 2\delta t\alpha(\mathcal{R}_1(t^{n+1}), \mathbf{e}^{n+1}) &\leq 4\frac{\alpha^2}{\rho}\delta t^2 \int_{t^n}^{t^{n+1}} \|\nabla\operatorname{div}(\mathbf{u}_{tt})\|_0^2 dt + \frac{\rho}{4}\delta t\|\mathbf{e}^{n+1}\|_0^2, \end{aligned}$$

and

$$2\delta t(\nabla\delta^2 p(t^{n+1}), \mathbf{e}^{n+1}) \leq \frac{4}{\rho}\delta t^4 \int_{t^{n-1}}^{t^{n+1}} \|\nabla p_{tt}\|_0^2 dt + \frac{\rho}{4}\delta t\|\mathbf{e}^{n+1}\|_0^2.$$

Gathering all the estimates provided above 1) - 3), we obtain

$$\begin{aligned}
& \rho(1 - \frac{3}{4}\delta t)\|\mathbf{e}^{n+1}\|_0^2 + \rho\|\delta\mathbf{e}^{n+1}\|_0^2 + 4\delta t\mu\|\nabla^S\mathbf{e}^{n+1}\|_0^2 + (\alpha - \frac{1}{2}\delta t)\|\operatorname{div}(\mathbf{e}^{n+1})\|_0^2 \\
& + (\alpha - 1)\|\operatorname{div}(\delta\mathbf{e}^{n+1})\|_0^2 + \delta t^2(\|\pi^{n+1}\|_1^2 - \|\pi^n\|_1^2) + \delta t^2\|\delta\pi^n\|_1^2 \lesssim \rho(1 - \frac{3}{4}\delta t)\|\mathbf{e}^n\|_0^2 + \frac{3}{2}\delta t\|\mathbf{e}^n\|_0^2 \\
& + (\alpha - \frac{1}{2}\delta t)\|\operatorname{div}(\mathbf{e}^n)\|_0^2 + \delta t\|\operatorname{div}(\mathbf{e}^n)\|_0^2 + \delta t^3\|\pi^n\|_1^2 + \delta t^3\|\delta\pi^n\|_1^2 \\
& + \delta t^2\|\mathbf{u}_{tt}\|_{L^2(t^n, t^{n+1}; L^2)}^2 + \delta t^2\|\nabla\operatorname{div}(\mathbf{u}_{tt})\|_{L^2(t^n, t^{n+1}; L^2)}^2 \\
& + \delta t^2\|p_t\|_{L^2(t^n, t^{n+1}; L^2)}^2 + \delta t^4\|\nabla p_{tt}\|_{L^2(t^{n-1}, t^{n+1}; L^2)}^2 \quad (2.57)
\end{aligned}$$

Summing the above relations for $n = 0, \dots, N-1$, we get

$$\begin{aligned}
& \rho(1 - \frac{3}{4}\delta t)\|\mathbf{e}^N\|_0^2 + \sum_{n=0}^{N-1} \rho\|\delta\mathbf{e}^{n+1}\|_0^2 + 4\sum_{n=0}^{N-1} \delta t\mu\|\nabla^S\mathbf{e}^{n+1}\|_0^2 + (\alpha - \frac{1}{2}\delta t)\|\operatorname{div}\mathbf{e}^N\|_0^2 \\
& + (\alpha - 1)\sum_{n=0}^{N-1} \|\operatorname{div}(\delta\mathbf{e}^{n+1})\|_0^2 + \delta t^2\|\pi^N\|_1^2 + \sum_{n=0}^{N-1} \delta t^2(1 - \delta t)\|\delta\pi^n\|_1^2 \\
& \lesssim \delta t^2 + \sum_{n=0}^{N-1} \frac{3}{2}\delta t\|\mathbf{e}^n\|_0^2 + \sum_{n=0}^{N-1} \delta t\|\operatorname{div}(\mathbf{e}^n)\|_0^2 + \sum_{n=0}^{N-1} \delta t^3\|\pi^n\|_1^2. \quad (2.58)
\end{aligned}$$

Assuming that δt is small enough, we use Gronwall's inequality to conclude the proof. \square

Now, we derive several estimates about the increment of the velocity which will be instrumental in the analysis of the pressure stability and convergence.

Lemma 2.3.1. Under the assumptions of Theorem 2.3.2, we get

$$\rho\|\mathbf{e}^1\|_0^2 + \rho\|\delta\mathbf{e}^1\|_0^2 + \alpha\|\operatorname{div}(\delta\mathbf{e}^1)\|_0^2 \lesssim \delta t^4.$$

Proof. Choosing $\mathbf{v} = 2\delta t\mathbf{e}^1$ in (2.51) with $n = 0$ we get

$$\rho\|\mathbf{e}^1\|_0^2 + \rho\|\delta\mathbf{e}^1\|_0^2 + 4\delta t\mu\|\nabla^S\mathbf{e}^1\|_0^2 + 2\alpha\|\operatorname{div}(\mathbf{e}^1)\|_0^2 = 2\delta t(\rho\mathcal{R}_0(t^1) + \alpha\mathcal{R}_1(t^1) + \nabla\delta p(t^1), \mathbf{e}^1).$$

The right hand side term is bounded similarly as Lemma 2.2.6 by using Lemma 2.2.4 and Lemma 2.2.5, and therefore satisfies

$$\frac{1}{4}\rho\|\mathbf{e}^1\|_0^2 + \rho\|\delta\mathbf{e}^1\|_0^2 + 4\delta t\mu\|\nabla^S\mathbf{e}^1\|_0^2 + 2\alpha\|\operatorname{div}(\mathbf{e}^1)\|_0^2 \lesssim \delta t^4. \quad \square \quad (2.59)$$

Lemma 2.3.2. Under the assumptions of Theorem 2.3.2 that holds

$$\|\delta\pi^1\|_1^2 \lesssim \delta t^2.$$

Proof. Taking $q = \delta\pi^1$ into (2.52) when $n = 0$ and a Cauchy Schwarz estimate yields

$$\|\delta\pi^1\|_1^2 \leq \frac{1}{\delta t^2}\|\operatorname{div}(\mathbf{e}^1)\|_0^2 + \|\nabla\delta p(t^1)\|_0^2.$$

Thus by applying Lemma 2.2.5 and Lemma 2.3.1, we obtain

$$\|\delta\pi^1\|_1^2 \lesssim \delta t^2. \quad \square$$

From Lemma 2.3.1 and Lemma 2.3.2 we can derive the following result.

Corollary 2.3.1 (Velocity Increment Error Estimate). Under the assumptions of Theorem 2.3.2, we have

$$\begin{aligned} \|\delta\mathbf{e}\|_{l^\infty(L^2(\Lambda))}^2 + \alpha\|\operatorname{div}(\delta\mathbf{e})\|_{l^\infty(L^2(\Lambda))}^2 &\lesssim \rho\|\delta\mathbf{e}^1\|_0^2 + \alpha\|\operatorname{div}(\delta\mathbf{e}^1)\|_0^2 + \delta t^2\|\delta\pi^1\|_1^2 \\ &\lesssim \delta t^4. \end{aligned}$$

Proof. The proof of this Corollary follows the same principle as that we used in Theorem 2.3.2. The only difference is here it consists in working with the time increments $\delta\mathbf{e}^{n+1}$, but we can easily deal with this by taking the time increment of

the whole scheme (2.44)-(2.45) and applying Lemma 2.3.1 and Lemma 2.3.2. \square

Lemma 2.3.3. (Estimate on Increments) Using the result of velocity increment error estimate, we can derive the velocity increment stability estimate such as:

$$\sum_{n=0}^{N-1} \|\delta \mathbf{u}^{n+1}\|_0^2 + \sum_{n=0}^{N-1} \alpha \|\operatorname{div}(\delta \mathbf{u}^{n+1})\|_0^2 \lesssim \delta t, \quad (2.60)$$

provided \mathbf{u} smooth enough.

Proof. Using the identity $\delta \mathbf{u}^{n+1} = \delta \mathbf{u}(t^{n+1}) - \delta \mathbf{e}^{n+1}$, we obtain

$$\begin{aligned} \|\delta \mathbf{u}^{n+1}\|_0 + \alpha \|\operatorname{div} \delta \mathbf{u}^{n+1}\|_0 &= \|\delta \mathbf{u}(t^{n+1}) - \delta \mathbf{e}^{n+1}\|_0 + \alpha \|\operatorname{div} \delta \mathbf{u}(t^{n+1}) - \operatorname{div} \delta \mathbf{e}^{n+1}\|_0 \\ &\leq \|\delta \mathbf{u}(t^{n+1})\|_0 + \|\delta \mathbf{e}^{n+1}\|_0 \\ &\quad + \alpha \|\operatorname{div}(\delta \mathbf{u}(t^{n+1}))\|_0 + \alpha \|\operatorname{div}(\delta \mathbf{e}^{n+1})\|_0. \end{aligned}$$

Squaring both sides and summing up for $n = 0, \dots, N - 1$ yields

$$\begin{aligned} \sum_{n=0}^{N-1} \|\delta \mathbf{u}^{n+1}\|_0^2 + \sum_{n=0}^{N-1} \alpha \|\operatorname{div}(\delta \mathbf{u}^{n+1})\|_0^2 &\lesssim \sum_{n=0}^{N-1} \|\delta \mathbf{e}^{n+1}\|_0^2 + \sum_{n=0}^{N-1} \alpha \|\operatorname{div}(\delta \mathbf{e}^{n+1})\|_0^2 \\ &\quad + \delta t \int_0^T \|\mathbf{u}_t\|_0^2 dt + \delta t \int_0^T \|\operatorname{div} \mathbf{u}_t\|_0^2 dt \\ &\leq \delta t, \end{aligned}$$

after applying Lemma 2.2.3 and Corollary 2.3.1. \square

Now, let's work on stability and error convergence rate for the pressure.

Theorem 2.3.3 (Pressure Stability). Set $\mathbf{f} = \mathbf{0}$ in (2.40) then there holds

$$\|p\|_{l^2(L^2(\Lambda))} \leq C,$$

with a positive constant C independent of n , provided \mathbf{u} and p smooth enough.

Proof. Choosing $q = p^n + \psi^n$ in (2.38) implies

$$\|p^n + \psi^n\|_0 \lesssim \frac{\rho}{\delta t} \|\delta \mathbf{u}^{n+1}\|_0 + 2\mu \|\nabla^S \mathbf{u}^{n+1}\|_0 + \frac{\alpha}{\delta t} \|\operatorname{div}(\delta \mathbf{u}^{n+1})\|_0$$

from (2.44). Squaring both sides and multiplying δt and the above relation yield

$$\delta t \|p^n + \psi^n\|_0^2 \lesssim \frac{\rho}{\delta t} \|\delta \mathbf{u}^{n+1}\|_0^2 + \delta t \mu \|\nabla \mathbf{u}^{n+1}\|_0^2 + \frac{\alpha}{\delta t} \|\operatorname{div}(\delta \mathbf{u}^{n+1})\|_0^2. \quad (2.61)$$

Summing for $n = 0, \dots, N-1$, we obtain

$$\sum_{n=1}^{N-1} \delta t \|p^n + \psi^n\|_0^2 \lesssim \frac{\rho}{\delta t} \sum_{n=1}^{N-1} \|\delta \mathbf{u}^{n+1}\|_0^2 + \sum_{n=1}^{N-1} \delta t \mu \|\nabla \mathbf{u}^{n+1}\|_0^2 + \sum_{n=1}^{N-1} \frac{\alpha}{\delta t} \|\operatorname{div}(\delta \mathbf{u}^{n+1})\|_0^2. \quad (2.62)$$

Finally, we can apply Lemma 2.3.3 and Theorem 2.3.1 to conclude the proof. \square

Theorem 2.3.4 (Pressure Error Estimates). Under the assumptions of Theorem 2.3.2, the pressure solution of (2.44)-(2.45) satisfies the error estimate:

$$\|\pi\|_{l^2(L^2(\Lambda))} \lesssim \delta t.$$

Proof. We take the extrapolation $q = (\pi^n)^\star = 2\pi^n - \pi^{n-1}$ into (2.38) and we obtain

$$\begin{aligned} \|(\pi^n)^\star\|_0 &\lesssim \frac{\rho}{\delta t} \|\delta \mathbf{e}^{n+1}\|_0 + 2\mu \|\nabla^S \mathbf{e}^{n+1}\|_0 + \frac{\alpha}{\delta t} \|\operatorname{div}(\delta \mathbf{e}^{n+1})\|_0 \\ &\quad + \rho \|\mathcal{R}_0(t^{n+1})\|_0 + \alpha \|\mathcal{R}_1(t^{n+1})\|_0 + \|\delta^2 p(t^{n+1})\|_0 \end{aligned}$$

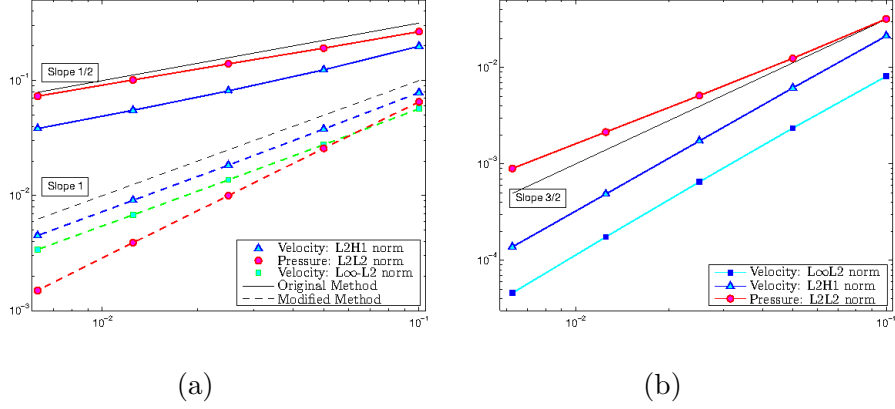


Figure 2.1: Errors vs. δt : Convergence rate for original and modified standard pressure correction projection method (a), and modified rotational correction projection method (b) with in particular norms.

by using (2.51). Now, squaring on both sides and multiplying by δt we get

$$\begin{aligned} \delta t \|(\pi^n)^*\|_0^2 &\lesssim \frac{\rho}{\delta t} \|\delta \mathbf{e}^{n+1}\|_0^2 + \delta t \mu \|\nabla^S \mathbf{e}^{n+1}\|_0^2 + \frac{\alpha}{\delta t} \|\operatorname{div}(\delta \mathbf{e}^{n+1})\|_0^2 \\ &\quad + \delta t \rho \|\mathcal{R}_0(t^{n+1})\|_0^2 + \delta t \alpha \|\mathcal{R}_1(t^{n+1})\|_0^2 + \delta t \|\delta^2 p(t^{n+1})\|_0^2. \end{aligned}$$

Summing for $n = 0, \dots, N-1$, we get the estimate

$$\begin{aligned} \sum_{n=1}^{N-1} \delta t \|(\pi^n)^*\|_0^2 &\lesssim \sum_{n=1}^{N-1} \frac{\rho}{\delta t} \|\delta \mathbf{e}^{n+1}\|_0^2 + \sum_{n=1}^{N-1} \delta t \mu \|\nabla^S \mathbf{e}^{n+1}\|_0^2 + \sum_{n=1}^{N-1} \frac{\alpha}{\delta t} \|\operatorname{div}(\delta \mathbf{e}^{n+1})\|_0^2 \\ &\quad + \delta t^2 \int_0^T \|\mathbf{u}_{tt}\|_0^2 dt + \delta t^2 \int_0^T \|\nabla \operatorname{div}(\mathbf{u}_{tt})\|_0^2 dt + \delta t^2 \int_0^T \|p_{tt}\|_0^2 dt. \end{aligned}$$

We apply Theorem 2.3.2 and Corollary 2.3.1 to conclude the proof. \square

2.3.2 Numerical results

To illustrate the optimality of the proposed algorithm, we consider the same setting as in Section 2.2.2. The behavior of the errors in velocity and pressure ap-

proximations versus the time step δt used are depicted in Figure 2.1. Suboptimal order of convergence $\mathcal{O}(\delta t^{1/2})$ is observed for the standard method while the optimal order of convergence $\mathcal{O}(\delta t)$ is recovered using the proposed scheme. The space discretization is chosen fine enough not to interfere with the time discretization error. The analysis of modified rotational pressure correction scheme is still an open problem.

2.4 Variable time stepping Standard Pressure Correction Projection Method

The second modification in the standard incremental pressure correction projection method is to allow the variable time stepping. It turns out that the straightforward generalization of constant time stepping to variable time stepping is unstable, see Figure 2.2. The proposed scheme is not only stable but also exhibits the optimal first order decay. Numerical computations illustrating the theoretical estimates are provided for both new schemes. To the best of our knowledge, projection schemes with variable time stepping have not been studied in the literature. Notice however, that no additional difficulty arises from having variable time stepping in the non-incremental scheme setting.

From original non-implementable incremental scheme (2.8)-(2.10), we can derive the implementable variable time stepping scheme by applying similar steps as (2.11)-(2.14), but with the variable time steps $\delta t^n := t^n - t^{n-1} > 0$, $n = 1, \dots, N$. Thus, the first step of implementable scheme with the variable time stepping becomes to find $\mathbf{u}^{n+1} \in [H_0^1(\Lambda)]^d$ by solving,

$$\rho \frac{\mathbf{u}^{n+1} - \mathbf{u}^n}{\delta t^{n+1}} - 2\operatorname{div}(\mu \nabla^S \mathbf{u}^{n+1}) + \nabla(p^n + \frac{\delta t^n}{\delta t^{n+1}} \psi^n) = \mathbf{f}(\cdot, t^{n+1}) \text{ in } \Lambda, \quad (2.63)$$

with the Dirichlet boundary condition, $\mathbf{u}^{n+1} = 0$ on $\partial\Lambda$. Note, the apparition of the

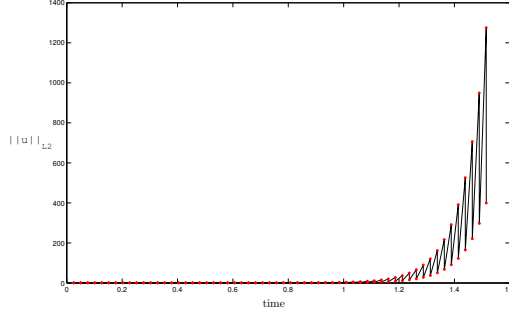


Figure 2.2: Evolution of $\|\mathbf{u}(\cdot, t^n)\|_{L^2(\Lambda)}$ when using the general scheme (2.63)-(2.65) with $\delta t^1 = 0.025$ and δt^n given by (2.66).

coefficient $\frac{\delta t^n}{\delta t^{n+1}}$ in front of ψ . The second step reads: Seek $\psi^{n+1} \in H^1(\Lambda) \cap L_0^2(\Lambda)$ satisfying

$$\Delta \psi^{n+1} = \frac{\rho}{\delta t^{n+1}} \operatorname{div}(\mathbf{u}^{n+1}) \text{ in } \Lambda, \text{ and } \frac{\partial \psi^{n+1}}{\partial \boldsymbol{\nu}} = 0 \text{ on } \partial \Lambda, \quad (2.64)$$

and we update the pressure in a third step according to

$$p^{n+1} = p^n + \psi^{n+1}. \quad (2.65)$$

However scheme (2.63)-(2.65) is unstable. We illustrate this fact by considering the same setting as in Section 2.2.2, but we use variable time steps chosen as

$$\delta t^n = \delta t^1 \times \begin{cases} 1 & \text{when } n \text{ is odd,} \\ 10^{-2} & \text{when } n \text{ is even,} \end{cases} \quad (2.66)$$

with $\delta t^1 = 0.025$. Figure 2.2 illustrates the unstable behavior of $\|\mathbf{u}^n\|_{L^2(\Lambda)}$ for $n = 0, \dots, N$.

We propose a new variable time stepping scheme assuming for a positive constant

$\overline{\delta t}$ independent of n , that holds

$$\delta t^n \leq \overline{\delta t}, \quad \forall 1 \leq n \leq N.$$

Given \mathbf{u}^n , ψ^n and p^n , the velocity approximation at t^{n+1} is defined by the relation

$$\rho \frac{\mathbf{u}^{n+1} - \mathbf{u}^n}{\delta t^{n+1}} - 2\operatorname{div}(\mu \nabla^S \mathbf{u}^{n+1}) + \nabla(p^n + \frac{(\overline{\delta t})^2}{\delta t^n \delta t^{n+1}} \psi^n) = \mathbf{f}(\cdot, t^{n+1}), \quad \text{in } \Lambda. \quad (2.67)$$

For simplicity, we consider the boundary condition $\mathbf{u} = \mathbf{0}$ on $\partial\Lambda$ but the techniques presented in Section 2.3 for the open boundary condition case apply in this context as well. The pressure increment ψ^{n+1} is the solution to

$$-\frac{(\overline{\delta t})^2}{\delta t^{n+1}} \Delta \psi^{n+1} = -\rho \operatorname{div}(\mathbf{u}^{n+1}) \quad \text{in } \Lambda \quad \text{and} \quad \frac{\partial}{\partial \boldsymbol{\nu}} \psi^{n+1} = 0 \quad \text{on } \partial\Lambda. \quad (2.68)$$

Finally, the pressure is updated according to the relation (2.65).

To the best of the authors knowledge, incremental projection schemes with variable time stepping have not been studied in the literature. Note that, the factors $\frac{\overline{\delta t}^2}{\delta t^n \delta t^{n+1}}$ and $\frac{\overline{\delta t}^2}{\delta t^{n+1}}$ multiplying the increment ψ^n in (2.67) and (2.68), respectively, are not the expected factors $\frac{\delta t^n}{\delta t^{n+1}}$ and δt^{n+1} , respectively, when using the (2.63) and (2.64)

2.4.1 Stability and error estimate

We now discuss the stability and error estimates for the scheme (2.67)-(2.68). We take the $L^2(\Lambda)$ inner product with corresponding test functions and apply the boundary conditions to cancel the boundary term appearing after the integration by

parts. Thus, we find $\mathbf{u}^{n+1} \in [H_0^1(\Lambda)]^d$ that solves

$$\begin{aligned} \int_{\Lambda} \rho \left(\frac{\mathbf{u}^{n+1} - \mathbf{u}^n}{\delta t^{n+1}} \right) \mathbf{v} + \int_{\Lambda} 2\mu (\nabla^S \mathbf{u}^{n+1} : \nabla^S \mathbf{v}) - \int_{\Lambda} (p^n + \frac{(\bar{\delta t})^2}{\delta t^n \delta t^{n+1}} \psi^n) \operatorname{div}(\mathbf{v}) \\ = \int_{\Lambda} \mathbf{f}(\cdot, t^{n+1}) \mathbf{v}, \quad \forall \mathbf{v} \in [H_0^1(\Lambda)]^d, \end{aligned} \quad (2.69)$$

and $\psi^{n+1} \in H^1(\Lambda) \cap L_0^2(\Lambda)$ that solves

$$\int_{\Lambda} \frac{(\bar{\delta t})^2}{\delta t^{n+1}} \nabla \psi^{n+1} \nabla q = - \int_{\Lambda} \rho \operatorname{div}(\mathbf{u}^{n+1}) q, \quad \forall q \in H^1(\Lambda) \cap L_0^2(\Lambda). \quad (2.70)$$

The stability of the velocity field approximation is guaranteed by the following theorem.

Theorem 2.4.1 (Velocity Stability). Set $\mathbf{f} = \mathbf{0}$ in (2.69), and assume $\delta t^n \leq \bar{\delta t}$, $n = 1, \dots, N$, then there holds

$$\rho \|\mathbf{u}\|_{l^\infty(L^2(\Lambda))}^2 + 4\mu \|\nabla^S \mathbf{u}\|_{l^2(L^2(\Lambda))}^2 + \frac{1}{\rho} (\bar{\delta t})^2 \|p\|_{l^\infty(H^1(\Lambda))}^2 \leq \rho \|\mathbf{u}_0\|_0^2 + \frac{1}{\rho} (\bar{\delta t})^2 \|p_0\|_0^2,$$

provided $\mathbf{u}_0 \in [L^2(\Lambda)]^d$ and $p_0 \in H^1(\Lambda)$.

Proof. Choosing $\mathbf{v} = 2\delta t^{n+1} \mathbf{u}^{n+1}$ in (2.69) we find

$$\begin{aligned} \rho \left(\|\mathbf{u}^{n+1}\|_0^2 + \|\mathbf{u}^{n+1} - \mathbf{u}^n\|_0^2 - \|\mathbf{u}^n\|_0^2 \right) + 4\delta t^{n+1} \mu \|\nabla^S \mathbf{u}^{n+1}\|_0^2 \\ - 2 \left(\delta t^{n+1} p^n + \frac{(\bar{\delta t})^2}{\delta t^n} \psi^n, \operatorname{div}(\mathbf{u}^{n+1}) \right) = 0. \end{aligned} \quad (2.71)$$

The pressure increment relation (2.68) is invoked to derive a bound for the last term in the left hand side of the above relation. More precisely, we realize that taking

$q = 2(\delta t^{n+1} p^n + \frac{(\bar{\delta t})^2}{\delta t^n} \psi^n)$ in (2.70) yields,

$$\begin{aligned} & -2\rho(\delta t^{n+1} p^n + \frac{(\bar{\delta t})^2}{\delta t^n} \psi^n, \operatorname{div}(\mathbf{u}^{n+1})) \\ & = 2(\bar{\delta t})^2(\nabla \psi^{n+1}, \nabla p^n) + 2\left(\nabla\left(\frac{(\bar{\delta t})^2}{\delta t^{n+1}} \psi^{n+1}\right), \nabla\left(\frac{(\bar{\delta t})^2}{\delta t^n} \psi^n\right)\right). \end{aligned}$$

Relation (2.65) allows us to rewrite the right hand side of the above expression as

$$\begin{aligned} & (\bar{\delta t})^2 \left(\|\nabla p^{n+1}\|_0^2 - \|\nabla p^n\|_0^2 - \|\nabla \psi^{n+1}\|_0^2 \right) \\ & + \frac{(\bar{\delta t})^4}{(\delta t^{n+1})^2} \|\nabla \psi^{n+1}\|_0^2 + \frac{(\bar{\delta t})^4}{(\delta t^n)^2} \|\nabla \psi^n\|_0^2 - \left\| \nabla \left(\frac{(\bar{\delta t})^2}{\delta t^{n+1}} \psi^{n+1} - \frac{(\bar{\delta t})^2}{\delta t^n} \psi^n \right) \right\|_0^2. \end{aligned}$$

Going back to (2.71), we get

$$\begin{aligned} & \rho \left(\|\mathbf{u}^{n+1}\|_0^2 + \|\mathbf{u}^{n+1} - \mathbf{u}^n\|_0^2 - \|\mathbf{u}^n\|_0^2 \right) + 4\delta t^{n+1} \mu \|\nabla^S \mathbf{u}^{n+1}\|_0^2 \\ & + \frac{1}{\rho} (\bar{\delta t})^2 \left(\|\nabla p^{n+1}\|_0^2 - \|\nabla p^n\|_0^2 \right) + \frac{1}{\rho} (\bar{\delta t})^2 \left(\frac{(\bar{\delta t})^2}{(\delta t^{n+1})^2} - 1 \right) \|\nabla \psi^{n+1}\|_0^2 \\ & + \frac{1}{\rho} \frac{(\bar{\delta t})^4}{(\delta t^n)^2} \|\nabla \psi^n\|_0^2 = \frac{1}{\rho} \left\| \nabla \left(\frac{(\bar{\delta t})^2}{\delta t^{n+1}} \psi^{n+1} - \frac{(\bar{\delta t})^2}{\delta t^n} \psi^n \right) \right\|_0^2. \end{aligned}$$

The difference of two successive relations (2.70) together with the boundary condition $\mathbf{u}^n = \mathbf{u}^{n+1} = 0$ on $\partial\Lambda$ guarantee that

$$\left\| \nabla \left(\frac{(\bar{\delta t})^2}{\delta t^{n+1}} \psi^{n+1} - \frac{(\bar{\delta t})^2}{\delta t^n} \psi^n \right) \right\|_0 \leq \rho \|\mathbf{u}^{n+1} - \mathbf{u}^n\|_0.$$

Hence, using the assumption $\delta t^{n+1} \leq \bar{\delta t}$,

$$\begin{aligned} & \rho \left(\|\mathbf{u}^{n+1}\|_0^2 - \|\mathbf{u}^n\|_0^2 \right) + 4\delta t^{n+1} \mu \|\nabla^S \mathbf{u}^{n+1}\|_0^2 + \frac{1}{\rho} (\bar{\delta t})^2 \left(\|\nabla p^{n+1}\|_0^2 - \|\nabla p^n\|_0^2 \right) \\ & + \frac{1}{\rho} \frac{(\bar{\delta t})^4}{(\delta t^n)^2} \|\nabla \psi^n\|_0^2 \leq 0, \end{aligned}$$

and the desired bound follows after summing for $n = 0$ to $N - 1$. \square

2.4.1.1 Error Convergence

For convenience, we move the factor $(\frac{\overline{\delta t}}{\delta t^{n+1}})^2$ multiplying the increment ψ^n in (2.69) and (2.70) to the incremental step (2.65). In this view, we realize the scheme (2.69)-(2.69) and (2.65) changes to the following: We solve for the velocity $\mathbf{u}^{n+1} \in [H_0^1(\Lambda)]^d$ such that

$$\begin{aligned} \int_{\Lambda} \rho \left(\frac{\mathbf{u}^{n+1} - \mathbf{u}^n}{\delta t^{n+1}} \right) \mathbf{v} + \int_{\Lambda} 2\mu (\nabla^S \mathbf{u}^{n+1} : \nabla^S \mathbf{v}) - \int_{\Lambda} (p^n + \frac{\delta t^n}{\delta t^{n+1}} \psi^n) \operatorname{div}(\mathbf{v}) \\ = \int_{\Lambda} \mathbf{f}(\cdot, t^{n+1}) \mathbf{v}, \quad \forall \mathbf{v} \in [H_0^1(\Lambda)]^d, \end{aligned} \quad (2.72)$$

and, the pressure increment ψ^{n+1} as the solution to

$$\int_{\Lambda} \nabla \psi^{n+1} \nabla q = - \int_{\Lambda} \frac{\rho}{\delta t^{n+1}} \operatorname{div}(\mathbf{u}^{n+1}) q, \quad \forall q \in H^1(\Lambda) \cap L_0^2(\Lambda). \quad (2.73)$$

The increment step changes to

$$\left(\frac{\overline{\delta t}}{\delta t^{n+1}} \right)^2 p^{n+1} = \left(\frac{\overline{\delta t}}{\delta t^{n+1}} \right)^2 p^n + \psi^{n+1}. \quad (2.74)$$

In the following, we use the notations:

$$\mathbf{e}^n := \mathbf{u}(t^n) - \mathbf{u}^n, \quad \pi^n := p(t^n) - p^n,$$

and recall the norm conventions for sequences provided in Section 2.2. In addition, we introduce a notation: for any sequence $\varphi^0, \varphi^1, \dots$, we set

$$\begin{aligned}\theta(\varphi^{n+1}) &:= \delta t^{n+1} \varphi^{n+1} - \delta t^{n+1} \varphi^n - \delta t^n \left(\frac{\bar{\delta t}}{\delta t^n}\right)^2 \varphi^n + \delta t^n \left(\frac{\bar{\delta t}}{\delta t^n}\right)^2 \varphi^{n-1} \\ &= \delta t^{n+1} \delta \varphi^{n+1} - \delta t^n \left(\frac{\bar{\delta t}}{\delta t^n}\right)^2 \delta \varphi^n.\end{aligned}$$

Before we start the analysis, we introduce the lemma to derive the estimate for $\theta(p(t^{n+1}))$.

Lemma 2.4.1. Assuming p is smooth enough, we have

$$\|\theta(p(t^{n+1}))\|_0 \lesssim \bar{\delta t}^{3/2} \left(\int_{t^{n-1}}^{t^{n+1}} \|p_t\|_0^2 dt \right)^{1/2},$$

provided $\delta t^n \leq \bar{\delta t}$, $\forall n$.

Proof. It suffices to realize that

$$\|\theta(p(t^{n+1}))\|_0^2 \leq 2 \left((\delta t^{n+1})^2 \|\delta p(t^{n+1})\|_0^2 + \left(\frac{\bar{\delta t}}{\delta t^n}\right)^4 (\delta t^n)^2 \|\delta p(t^n)\|_0^2 \right),$$

and involves Lemma 2.2.3. □

Theorem 2.4.2 (Velocity Error Estimate). Assume that the solution (\mathbf{u}, p) is smooth enough and that there exists $0 < \bar{\delta t} < 1$ independent of N such that $\delta t^n \leq \bar{\delta t}$, $\forall n = 1, \dots, N$. Then the solution of (2.72)-(2.74) satisfies the error estimate

$$\rho \|\mathbf{e}\|_{l^\infty(L^2(\Lambda))} + \mu \|\nabla^S \mathbf{e}\|_{l^2(L^2(\Lambda))} \lesssim \bar{\delta t}.$$

Proof. We start by subtracting equation (2.72) from (2.15) at time t^{n+1} . We find

$$\begin{aligned} & \int_{\Lambda} \rho(\mathbf{e}^{n+1} - \mathbf{e}^n) \mathbf{v} + \int_{\Lambda} 2\delta t^{n+1} \mu(\nabla^S \mathbf{e}^{n+1} : \nabla^S \mathbf{v}) \\ & \quad - \int_{\Lambda} \left(\delta t^{n+1} p(t^{n+1}) - (\delta t^{n+1} p^n + \delta t^n \psi^n) \right) \operatorname{div}(\mathbf{v}) \\ & \quad = \int_{\Lambda} \delta t^{n+1} \rho \mathcal{R}_0(t^{n+1}) \mathbf{v}, \quad \forall \mathbf{v} \in [H_0^1(\Lambda)]^d, \end{aligned} \quad (2.75)$$

where $\mathcal{R}_0(t^{n+1})$ is defined in (2.21). The pressure term at (2.75) can be rewritten as,

$$\delta t^{n+1} p(t^{n+1}) - (\delta t^{n+1} p^n + \delta t^n \psi^n) = \theta(p(t^{n+1})) + \delta t^{n+1} \pi^n + \delta t^n \left(\frac{\bar{\delta t}}{\delta t^n} \right)^2 \delta \pi^n.$$

Gathering above relations, we can rewrite (2.75) as,

$$\begin{aligned} & \int_{\Lambda} \rho(\mathbf{e}^{n+1} - \mathbf{e}^n) \mathbf{v} + \int_{\Lambda} 2\delta t^{n+1} \mu(\nabla^S \mathbf{e}^{n+1} : \nabla^S \mathbf{v}) \\ & \quad - \int_{\Lambda} \left(\delta t^{n+1} \pi^n + \delta t^n \left(\frac{\bar{\delta t}}{\delta t^n} \right)^2 \delta \pi^n \right) \operatorname{div}(\mathbf{v}) = \int_{\Lambda} \mathcal{R}(t^{n+1}) \mathbf{v}, \end{aligned} \quad (2.76)$$

where the residual $\mathcal{R}(t^{n+1})$ is defined as

$$\mathcal{R}(t^{n+1}) := \delta t^{n+1} \rho \mathcal{R}_0(t^{n+1}) + \theta(p(t^{n+1})).$$

Also by subtracting (2.73) from (2.15) at time t^{n+1} we get

$$\int_{\Lambda} \delta t^{n+1} \nabla \psi^{n+1} \nabla q = \int_{\Lambda} \rho \operatorname{div}(\mathbf{e}^{n+1}) q, \quad \forall q \in H^1(\Lambda) \cap L_0^2(\Lambda).$$

Using the relation (2.74), we have

$$\delta t^{n+1} \psi^{n+1} = \delta t^{n+1} \left(\frac{\bar{\delta t}}{\delta t^{n+1}} \right)^2 (p^{n+1} - p^n) = \delta t^{n+1} \left(\frac{\bar{\delta t}}{\delta t^{n+1}} \right)^2 (\delta p(t^{n+1}) - \delta \pi^{n+1}),$$

which yields

$$\begin{aligned} \int_{\Lambda} \delta t^{n+1} \left(\frac{\bar{\delta t}}{\delta t^{n+1}} \right)^2 \nabla (\delta p(t^{n+1}) - \delta \pi^{n+1}) \nabla q \\ = \int_{\Lambda} \rho \operatorname{div}(\mathbf{e}^{n+1}) q, \quad \forall q \in H^1(\Lambda) \cap L_0^2(\Lambda). \end{aligned} \quad (2.77)$$

We take $\mathbf{v} = 2\mathbf{e}^{n+1}$ in (2.76) to get,

$$\begin{aligned} \rho (\|\mathbf{e}^{n+1}\|_0^2 - \|\mathbf{e}^n\|_0^2 + \|\delta \mathbf{e}^{n+1}\|_0^2) + 4\delta t^{n+1} \mu \|\nabla^S \mathbf{e}^{n+1}\|_0^2 \\ = 2(\delta t^{n+1} \pi^n + \delta t^n \left(\frac{\bar{\delta t}}{\delta t^n} \right)^2 \delta \pi^n, \operatorname{div}(\mathbf{e}^{n+1})) + 2(\mathcal{R}(t^{n+1}), \mathbf{e}^{n+1}). \end{aligned} \quad (2.78)$$

Note that the first term in the right hand side in (2.78) can be rewritten as

$$\begin{aligned} \delta t^{n+1} \pi^n + \delta t^n \left(\frac{\bar{\delta t}}{\delta t^n} \right)^2 \delta \pi^n &= \delta t^{n+1} \pi^n + \delta t^n \left(\frac{\bar{\delta t}}{\delta t^n} \right)^2 \pi^n - \delta t^n \left(\frac{\bar{\delta t}}{\delta t^n} \right)^2 \pi^{n-1} \\ &= -\theta(\pi^{n+1}) + \delta t^{n+1} \pi^{n+1}, \end{aligned}$$

upon adding and subtracting $\delta t^{n+1} \pi^{n+1}$. Thus, we can estimate the term by choosing $q = -2\theta(\pi^{n+1})$ and $q = 2\delta t^{n+1} \pi^{n+1}$ in (2.77). First, the choice $q = -2\theta(\pi^{n+1})$ gives

$$-2\rho(\operatorname{div} \mathbf{e}^{n+1}, \theta(\pi^{n+1})) = -2 \left(\frac{\bar{\delta t}}{\delta t^{n+1}} \right)^2 \delta t^{n+1} (\nabla \delta p(t^{n+1}) - \nabla \delta \pi^{n+1}, \nabla \theta(\pi^{n+1})).$$

Since, $\nabla \theta(\pi^{n+1}) = \delta t^{n+1} \nabla \delta \pi^{n+1} - \delta t^n \left(\frac{\bar{\delta t}}{\delta t^n} \right)^2 \nabla \delta \pi^n$, we get

$$\begin{aligned} -2\rho(\operatorname{div}(\mathbf{e}^{n+1}), \theta(\pi^{n+1})) &= -2 \frac{\bar{\delta t}^2}{\delta t^{n+1}} (\nabla \delta p(t^{n+1}), \nabla \theta(\pi^{n+1})) \\ &+ \left(\frac{\bar{\delta t}}{\delta t^{n+1}} \right)^2 \left(\|\delta t^{n+1} \nabla \delta \pi^{n+1}\|_0^2 - \|\delta t^n \left(\frac{\bar{\delta t}}{\delta t^n} \right)^2 \nabla \delta(\pi^n)\|_0^2 + \|\nabla \theta(\pi^{n+1})\|_0^2 \right). \end{aligned} \quad (2.79)$$

Next, we apply the same steps with $q = 2\delta t^{n+1}\pi^{n+1}$ to get,

$$\begin{aligned}
2\rho(\operatorname{div}(\mathbf{e}^{n+1}), \delta t^{n+1}\pi^{n+1}) &= 2\bar{\delta t}^2 \left((\nabla\delta p(t^{n+1}), \nabla\pi^{n+1}) - (\nabla\delta\pi^{n+1}, \nabla\pi^{n+1}) \right) \\
&= 2\frac{\bar{\delta t}^2}{\delta t^{n+1}} (\nabla\delta p(t^{n+1}), \delta t^{n+1}\nabla\pi^{n+1}) \\
&\quad - \bar{\delta t}^2 \left(\|\nabla\pi^{n+1}\|_0^2 - \|\nabla\pi^n\|_0^2 + \|\nabla\delta\pi^{n+1}\|_0^2 \right). \quad (2.80)
\end{aligned}$$

Adding (2.79) and (2.80), we get

$$\begin{aligned}
2(\operatorname{div}(\mathbf{e}^{n+1}), \delta t^{n+1}\pi^n + \delta t^n \left(\frac{\bar{\delta t}}{\delta t^n}\right)^2 \delta\pi^n) &= \frac{2\bar{\delta t}^2}{\rho\delta t^{n+1}} (\nabla\delta p(t^{n+1}), \nabla(\delta t^{n+1}\pi^n + \delta t^n \left(\frac{\bar{\delta t}}{\delta t^n}\right)^2 \delta\pi^n)) \\
&\quad - \frac{1}{\rho} \frac{\bar{\delta t}^6}{(\delta t^{n+1})^2 (\delta t^n)^2} \|\nabla\delta\pi^n\|_0^2 + \frac{1}{\rho} \left(\frac{\bar{\delta t}}{\delta t^{n+1}}\right)^2 \|\nabla\theta(\pi^{n+1})\|_0^2 \\
&\quad - \frac{1}{\rho} (\bar{\delta t})^2 \|\nabla\pi^{n+1}\|_0^2 + \frac{1}{\rho} (\bar{\delta t})^2 \|\nabla\pi^n\|_0^2. \quad (2.81)
\end{aligned}$$

The above relation indicates the need for an estimate of 1) $\frac{1}{\rho} \left(\frac{\bar{\delta t}}{\delta t^{n+1}}\right)^2 \|\nabla\theta(\pi^{n+1})\|_0^2$

and 2) $\frac{2\bar{\delta t}^2}{\rho\delta t^{n+1}} (\nabla\delta p(t^{n+1}), \nabla(\delta t^{n+1}\pi^n + \delta t^n \left(\frac{\bar{\delta t}}{\delta t^n}\right)^2 \delta\pi^n))$.

1) $\frac{1}{\rho} \left(\frac{\bar{\delta t}}{\delta t^{n+1}}\right)^2 \|\nabla\theta(\pi^{n+1})\|_0^2$: Taking to the difference between two following successive relations of (2.77) rewritten as follow using the boundary condition $\mathbf{e}^n = \mathbf{e}^{n+1} = \mathbf{0}$ on $\partial\Lambda$:

$$\begin{aligned}
\int_{\Lambda} \delta t^{n+1} \nabla(\delta p(t^{n+1}) - \delta\pi^{n+1}) \nabla q &= - \left(\frac{\delta t^{n+1}}{\bar{\delta t}}\right)^2 \int_{\Lambda} \rho \mathbf{e}^{n+1} \nabla q, \\
\int_{\Lambda} \delta t^n \left(\frac{\bar{\delta t}}{\delta t^n}\right)^2 \nabla(\delta p(t^n) - \delta\pi^n) \nabla q &= - \int_{\Lambda} \rho \mathbf{e}^n \nabla q,
\end{aligned}$$

leads to

$$\int_{\Lambda} \nabla\theta(\pi^{n+1}) \nabla q = \left(\frac{\delta t^{n+1}}{\bar{\delta t}}\right)^2 \int_{\Lambda} \rho \mathbf{e}^{n+1} \nabla q - \int_{\Lambda} \rho \mathbf{e}^n \nabla q + \int_{\Lambda} \nabla\theta(p(t^{n+1})) \nabla q \quad (2.82)$$

Choosing $q = (\frac{\bar{\delta t}}{\delta t^{n+1}})^2 \theta(\pi^{n+1})$ in (2.82) yields,

$$\begin{aligned} \frac{1}{\rho} \left(\frac{\bar{\delta t}}{\delta t^{n+1}} \right)^2 \|\nabla \theta(\pi^{n+1})\|_0^2 &= \rho(\delta \mathbf{e}^{n+1}, \nabla \theta(\pi^{n+1})) + \frac{1}{\rho} \left(\frac{\bar{\delta t}}{\delta t^{n+1}} \right)^2 (\nabla \theta(p(t^{n+1})), \nabla \theta(\pi^{n+1})) \\ &\quad + \rho \left(1 - \left(\frac{\bar{\delta t}}{\delta t^{n+1}} \right)^2 \right) (\mathbf{e}^n, \nabla \theta(\pi^{n+1})). \end{aligned}$$

Applying a Cauchy Schwarz estimate derives

$$\frac{1}{\rho} \left(\frac{\bar{\delta t}}{\delta t^{n+1}} \right)^2 \|\nabla \theta(\pi^{n+1})\|_0 + \left(\left(\frac{\bar{\delta t}}{\delta t^{n+1}} \right)^2 - 1 \right) \|\mathbf{e}^n\|_0 \leq \frac{1}{\rho} \left(\frac{\bar{\delta t}}{\delta t^{n+1}} \right)^2 \|\nabla \theta(p(t^{n+1}))\|_0 + \|\delta \mathbf{e}^{n+1}\|_0,$$

and the relation $\delta t^{n+1} \leq \bar{\delta t}$ imply

$$\frac{1}{\rho} \left(\frac{\bar{\delta t}}{\delta t^{n+1}} \right)^2 \|\nabla \theta(\pi^{n+1})\|_0 \leq \frac{1}{\rho} \left(\frac{\bar{\delta t}}{\delta t^{n+1}} \right)^2 \|\nabla \theta(p(t^{n+1}))\|_0 + \|\delta \mathbf{e}^{n+1}\|_0. \quad (2.83)$$

Squaring both sides, we get

$$\begin{aligned} \frac{1}{\rho} \left(\frac{\bar{\delta t}}{\delta t^{n+1}} \right)^2 \|\nabla \theta(\pi^{n+1})\|_0^2 &\leq \frac{1}{\rho} \left(\frac{\bar{\delta t}}{\delta t^{n+1}} \right)^2 \|\nabla \theta(p(t^{n+1}))\|_0^2 + \rho \left(\frac{\delta t^{n+1}}{\bar{\delta t}} \right)^2 \|\delta \mathbf{e}^{n+1}\|_0^2 \\ &\quad + 2 \|\nabla \theta(p(t^{n+1}))\|_0 \|\delta \mathbf{e}^{n+1}\|_0. \end{aligned}$$

Young's inequality, Lemma 2.4.1, and again the relation $\delta t^{n+1} \leq \bar{\delta t}$ imply

$$\begin{aligned} \frac{1}{\rho} \left(\frac{\bar{\delta t}}{\delta t^{n+1}} \right)^2 \|\nabla \theta(\pi^{n+1})\|_0^2 &\leq \left(\frac{(\bar{\delta t})^5}{\rho(\delta t^{n+1})^2} + \frac{2(\bar{\delta t})^2}{\rho} \right) \int_{t^{n-1}}^{t^{n+1}} \|\nabla p_t\|_0^2 dt + \rho \|\delta \mathbf{e}^{n+1}\|_0^2 \\ &\quad + \frac{\rho}{4} \bar{\delta t} \|\mathbf{e}^{n+1}\|_0^2 + \frac{\rho}{4} \bar{\delta t} \|\mathbf{e}^n\|_0^2. \quad (2.84) \end{aligned}$$

2) $\frac{2\bar{\delta t}^2}{\rho \delta t^{n+1}} (\nabla \delta p(t^{n+1}), \nabla (\delta t^{n+1} \pi^n + \delta t^n (\frac{\bar{\delta t}}{\delta t^n})^2 \delta \pi^n))$: Applying Cauchy Schwarz, Young's

inequality and Lemma 2.2.3, we can derive

$$\begin{aligned}
& \frac{2\bar{\delta t}^2}{\rho\delta t^{n+1}}(\nabla\delta p(t^{n+1}), \nabla(\delta t^{n+1}\pi^n + \delta t^n(\frac{\bar{\delta t}}{\delta t^n})^2\delta\pi^n)) \\
& \leq \frac{2\bar{\delta t}^2}{\rho\delta t^{n+1}}\|\nabla\delta p(t^{n+1})\|_0\|\nabla(\delta t^{n+1}\pi^n + \delta t^n(\frac{\bar{\delta t}}{\delta t^n})^2\delta\pi^n)\|_0 \\
& \leq \frac{1}{\rho}\bar{\delta t}^2\int_{t^n}^{t^{n+1}}\|\nabla p_t\|_0^2 dt + \frac{1}{\rho}(\frac{\bar{\delta t}}{\delta t^{n+1}})^2(\delta t^{n+1})\|\nabla(\delta t^{n+1}\pi^n + \delta t^n(\frac{\bar{\delta t}}{\delta t^n})^2\delta\pi^n)\|_0^2 \\
& \leq \frac{1}{\rho}\bar{\delta t}^2\int_{t^n}^{t^{n+1}}\|\nabla p_t\|_0^2 dt + \frac{1}{\rho}\bar{\delta t}^2\delta t^{n+1}\|\nabla\pi^n\|_0^2 + \frac{1}{\rho}\frac{\bar{\delta t}^6}{(\delta t^{n+1})^2(\delta t^n)^2}\delta t^{n+1}\|\nabla\delta\pi^n\|_0^2.
\end{aligned}$$

The above estimates on (2.76) yields

$$\begin{aligned}
& \rho(1 - \frac{\rho}{4}\bar{\delta t})\|\mathbf{e}^{n+1}\|_0^2 + 4\delta t^{n+1}\mu\|\nabla^S\mathbf{e}^{n+1}\|_0^2 + \frac{1}{\rho}\frac{\bar{\delta t}^6}{(\delta t^{n+1})^2(\delta t^n)^2}(1 - \delta t^{n+1})\|\nabla\delta\pi^n\|_0^2 \\
& + \frac{1}{\rho}(\bar{\delta t})^2\|\nabla\pi^{n+1}\|_0^2 \leq \rho(1 - \frac{\rho}{4}\bar{\delta t})\|\mathbf{e}^n\|_0^2 + \frac{\rho}{2}\bar{\delta t}\|\mathbf{e}^n\|_0^2 + \frac{1}{\rho}\bar{\delta t}^2(1 + \delta t^{n+1})\|\nabla\pi^n\|_0^2 \\
& + \bar{\delta t}^2(1 + \frac{\bar{\delta t}^3}{(\delta t^{n+1})^2})\int_{t^{n-1}}^{t^{n+1}}\|\nabla p_t\|_0^2 dt + 2(\mathcal{R}(t^{n+1}), \mathbf{e}^{n+1}). \quad (2.85)
\end{aligned}$$

It remains to estimate $2(\mathcal{R}(t^{n+1}), \mathbf{e}^{n+1})$. Involving Lemma 2.2.1 and Lemma 2.4.1, we apply several inequalities such as Cauchy Schwarz estimate, Poincare, and Young's inequality to get

$$\begin{aligned}
2(\mathcal{R}(t^{n+1}), \mathbf{e}^{n+1}) & = 2(\rho\delta t^{n+1}\mathcal{R}_0(t^{n+1}) + \nabla\theta(p(t^{n+1})), \mathbf{e}^{n+1}) \\
& \leq 2\rho\delta t^{n+1}\|\mathcal{R}_0(t^{n+1})\|_0\|\mathbf{e}^{n+1}\|_0 + 2\|\nabla\theta(p(t^{n+1}))\|_0\|\mathbf{e}^{n+1}\|_0 \\
& \leq 2\rho\delta t^{n+1}\|\mathcal{R}_0(t^{n+1})\|_0\|\mathbf{e}^{n+1}\|_0 + 2\bar{\delta t}^{3/2}\left(\int_{t^{n-1}}^{t^{n+1}}|p_t|_1^2 dt\right)^{1/2}\|\mathbf{e}^{n+1}\|_0 \\
& \lesssim \rho(\delta t^{n+1})^2\int_{t^n}^{t^{n+1}}\|\mathbf{u}_{tt}\|_0^2 dt + \frac{\bar{\delta t}}{2}\rho\|\mathbf{e}^{n+1}\|_0^2 + \frac{1}{\rho}\bar{\delta t}^2\int_{t^{n-1}}^{t^{n+1}}\|\nabla p_t\|_0^2 dt.
\end{aligned}$$

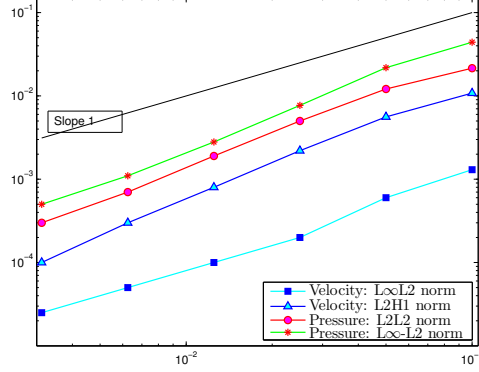


Figure 2.3: Decay of the velocity and pressure errors versus $\bar{\delta t}$ and with the time steps δt^n given by (2.66) when using the proposed scheme. The optimal order of convergence $\mathcal{O}(\bar{\delta t})$ is observed.

Returning to (2.85), we obtain

$$\begin{aligned} & \rho \left(1 - \frac{3\bar{\delta t}}{4}\right) \|\mathbf{e}^{n+1}\|_0^2 + 4\delta t^{n+1} \mu \|\nabla^S \mathbf{e}^{n+1}\|_0^2 + \frac{1}{\rho} \frac{(\bar{\delta t})^6}{(\delta t^{n+1})^2 (\delta t^n)^2} (1 - \delta t^{n+1}) \|\nabla \delta \pi^n\|_0^2 \\ & + \frac{1}{\rho} (\bar{\delta t})^2 \|\nabla \pi^{n+1}\|_0^2 \lesssim \rho \left(1 - \frac{3\bar{\delta t}}{4}\right) \|\mathbf{e}^n\|_0^2 + \rho \frac{3\bar{\delta t}}{2} \|\mathbf{e}^n\|_0^2 + \frac{1}{\rho} (\bar{\delta t})^2 (1 + \delta t^{n+1}) \|\nabla \pi^n\|_0^2 \\ & + (\delta t^{n+1})^2 \int_{t^n}^{t^{n+1}} \|\mathbf{u}_{tt}\|_0^2 dt + \bar{\delta t}^2 \int_{t^{n-1}}^{t^{n+1}} \|\nabla p_t\|_0^2 dt. \end{aligned}$$

Summing for $n = 0$ to $N - 1$ leads to

$$\begin{aligned} & \rho \left(1 - \frac{3\bar{\delta t}}{4}\right) \|\mathbf{e}^N\|^2 + 4 \sum_{n=0}^{N-1} \delta t^{n+1} \mu \|\nabla^S \mathbf{e}^{n+1}\|_0^2 + \frac{1}{\rho} \sum_{n=0}^{N-1} \frac{(\bar{\delta t})^6}{(\delta t^{n+1})^2 (\delta t^n)^2} (1 - \delta t^{n+1}) \|\nabla \delta \pi^n\|_0^2 \\ & + \frac{1}{\rho} (\bar{\delta t})^2 \|\nabla \pi^N\|^2 \lesssim (\bar{\delta t})^2 + \rho \sum_{n=0}^{N-1} \frac{3\bar{\delta t}}{2} \|\mathbf{e}^n\|_0^2 + \sum_{n=0}^{N-1} \frac{1}{\rho} (\bar{\delta t})^2 (\delta t^{n+1}) \|\nabla \pi^n\|_0^2. \quad (2.86) \end{aligned}$$

Using the the assumption $\delta t^n \leq \bar{\delta t} \ll 1, \forall n$ and applying Gronwall's lemma concludes the proof. \square

2.4.2 Numerical results

Using the same settings with Section 2.2.2 but variable time steps (2.66), we get the numerical result which is consistent with Theorem 2.4.2. As a result, the $l^2(H^1(\Lambda))$ and $l^\infty(L^2(\Lambda))$ errors on the velocity decay like $\bar{\delta t}$ when the proposed scheme (2.67)-(2.68) is used, see Figure 2.3. In addition, we emphasize that scheme (2.67)-(2.68) does not optimize the choice of δt^n in order to equi-distribute the time discretization errors and explain that the decay rate is dictated by $\bar{\delta t}$ (and not δt^n , $n = 1, \dots, N$). Including such mechanism is out of the scope of this work. Moreover, the decay rate for the $l^2(L^2(\Lambda))$ error on the pressure is still an open problem but the numerical results provided in Figure 2.3 indicate an optimal rate.

3. LEVEL SET METHOD WITH REINITIALIZATION AND ENTROPY STABILIZATION

The level set method defines an implicit representation of an hypersurface [43]. Let $\Lambda \subset \mathbb{R}^d$ ($d = 2, 3$) be the computational domain and $T > 0$ be the computational final time. The cavity Λ is filled by two non-mixing fluids evolving over time. We denote by $\Omega^+(t)$ and $\Omega^-(t)$ the open sets describing the regions occupied by each fluid and by $\Sigma(t)$ the interface between two fluids, see Figure 3.1.

3.1 Representation of the free interface via a level set function

The configuration of a two phase flow is described using a level set function $\phi(\mathbf{x}, t) : \Lambda \times [0, T] \rightarrow \mathbb{R}$ as follows:

$$\Omega^+(t) := \{\mathbf{x} \in \Lambda \mid \phi(\mathbf{x}, t) > 0\}, \quad \Omega^-(t) := \{\mathbf{x} \in \Lambda \mid \phi(\mathbf{x}, t) < 0\},$$

and

$$\Sigma(t) = \{\mathbf{x} \in \Lambda \mid \phi(\mathbf{x}, t) = 0\},$$

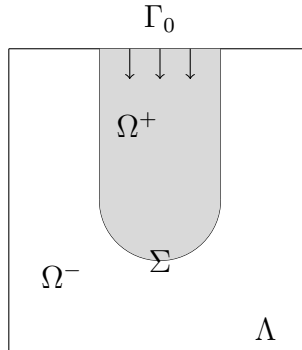


Figure 3.1: An example of a two phase flow system: A fluid(region Ω^+) is entering the cavity filled by another fluid(region Ω^-).

assuming that $|\nabla\phi(\mathbf{x}, t)| \neq 0$ in a neighborhood of $\Sigma(t)$. Assuming that the fluid evolves with a velocity $\mathbf{u} : \Lambda \rightarrow \mathbb{R}^d$ and that the fluids are immiscible, we consider the following evolution equation for the level set:

$$\frac{\partial}{\partial t}\phi + \mathbf{u} \cdot \nabla\phi = 0 \quad \text{in } \Lambda \times [0, T]. \quad (3.1)$$

The above relation is supplemented by an initial boundary condition $\phi(\mathbf{x}, 0) = \phi_0$ in Λ , and an inflow boundary condition $\phi = \phi_{\text{inflow}}$ on

$$\Gamma_0(t) := \{\mathbf{x} \in \partial\Lambda \mid \mathbf{u}(t) \cdot \boldsymbol{\nu} < 0\},$$

where $\boldsymbol{\nu}$ is the unit outer normal of Λ . A possible choice of ϕ_0 is,

$$\phi_0(\mathbf{x}) = \begin{cases} d(\mathbf{x}, \Sigma), & \mathbf{x} \in \Omega^+ \\ 0, & \mathbf{x} \in \Sigma \\ -d(\mathbf{x}, \Sigma), & \mathbf{x} \in \Omega^-, \end{cases} \quad (3.2)$$

where $d(\cdot, \cdot)$ is a distance function.

3.2 Reinitialization and cut off function

Now we discuss the feature called reinitialization for the level set system, ensuring $|\nabla\phi| \approx 1$ close to $\Sigma(t)$. To keep the slope close to a given function S , we define a reinitialized level set as the solution to:

$$\begin{cases} \frac{\partial}{\partial \tau}\tilde{\phi} + \text{sign}(\phi)(|\nabla\tilde{\phi}| - S) = 0 \\ \tilde{\phi}(\mathbf{x}, \tau = 0) = \phi(\mathbf{x}, t), \end{cases} \quad (3.3)$$

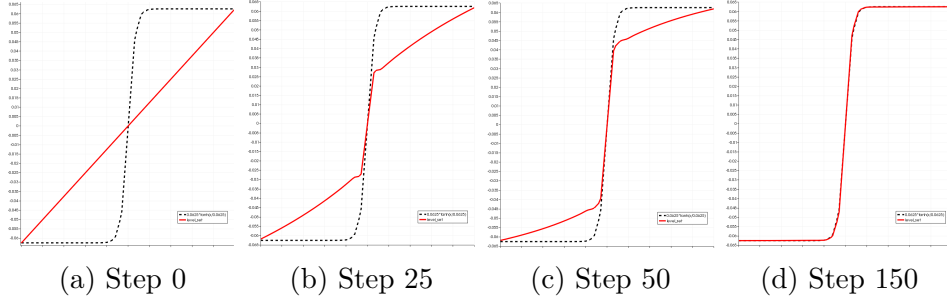


Figure 3.2: 1D Reinitialization steps(from left to right): In a given domain $(-1,1)$, initial distance function $\phi_0 = 0.0625x$ (Solid line) is given and we apply the reinitialization steps with the cut off function(Dashed line) given as (3.6) with $C_\phi = 0.0625$, $\varepsilon_S = 0$, $\mathbf{u} = \mathbf{0}$, and $\lambda = 1$.

where τ denotes a virtual time. Here $\text{sign}(\phi)$ is the sign function defined as:

$$\text{sign}(\phi) = \begin{cases} 1, & \phi > \varepsilon_S \\ -1, & \phi < -\varepsilon_S \\ 0, & |\phi| < \varepsilon_S, \end{cases} \quad (3.4)$$

where ε_S is defined on Section 3.7 after the discussion of the space discretization. Note that $\text{sign}(\phi) = 0$ where $\phi = 0$, thus this reinitialization step does not influence the interface position, and $\tilde{\phi}_\infty(\mathbf{x}) = \lim_{\tau \rightarrow \infty} \tilde{\phi}(\mathbf{x}, \tau)$ satisfies $|\nabla \tilde{\phi}_\infty| = S$. As proposed in [55], we combine the reinitialization process (3.3) with the actual transport equation for the level set ϕ . To this aim, we introduce the notations

$$\lambda := \frac{\partial \tau}{\partial t} \quad \text{and} \quad \mathbf{r} := \text{sign}(\phi) \frac{\nabla \phi}{|\nabla \phi|},$$

which gives

$$\frac{\partial}{\partial t} \tilde{\phi} = \lambda \frac{\partial}{\partial \tau} \tilde{\phi},$$

and so, ϕ satisfies

$$\frac{\partial}{\partial t}\phi + (\mathbf{u} + \lambda\mathbf{r}) \cdot \nabla\phi = \lambda\text{sign}(\phi)S. \quad (3.5)$$

Now we want to emphasize the importance of the choice of S , the expected slope. Note that $S \equiv 1$ ensures the desired slope of the interface but is not efficient as it requires the reinitialization of ϕ over the entire domain yet, only relevant information is the values of the level set function near the interface. Thus, we introduce the \tanh [personal communication with Coupez] cut off function filter:

$$\bar{\phi} := C_\phi \tanh\left(\frac{\phi}{C_\phi}\right), \quad (3.6)$$

where the positive constant C_ϕ depends on the space discretization (See Section 3.7 for the details). The slope of $\bar{\phi}$ is given by

$$|\nabla\bar{\phi}| = \left(1 - \left(\frac{\phi}{C_\phi}\right)^2\right).$$

Therefore $|\nabla\bar{\phi}| = 1$ near $\phi = 0$ and $|\nabla\bar{\phi}| \ll 1$ far away from $\phi = 0$. In view of this, we set $S = (1 - (\phi/C_\phi)^2)$ in (3.5) to obtain,

$$\frac{\partial}{\partial t}\phi + (\mathbf{u} + \lambda\mathbf{r}) \cdot \nabla\phi = \lambda\text{sign}(\phi)\left(1 - \left(\frac{\phi}{C_\phi}\right)^2\right). \quad (3.7)$$

Figure 3.2 shows how the reinitialization step works with this new cut off function. Note that due to the \tanh filter, ϕ is not a distance function anymore.

3.3 Space discretization using Finite Elements

Let \mathcal{T} be a subdivision of $\bar{\Lambda}$ made of disjoint elements K ; rectangles (when $d = 2$) or parallelepiped rectangles (when $d = 3$) such that $\bar{\Lambda} = \cup_{K \in \mathcal{T}} K$. Refer to [9] for more general elements. Let h denote the largest outer circle diameter of the elements.

For any integer $k \geq 1$ and $K \in \mathcal{T}$ we denote by $\mathbb{Q}^k(K)$, the space of polynomials of degree ($\leq k$) on each variable coordinates over K . We denote by $\mathbb{W}(\mathcal{T})$ the associated H^1 conforming finite elements based on piecewise $\mathbb{Q}^k(K)$ element, i.e

$$\mathbb{W}(\mathcal{T}) := \{V \in C^0(\bar{\Lambda}) \mid V = 0 \text{ on } \Gamma_0, V|_K \in \mathbb{Q}^k(K), \forall K \in \mathcal{T}\},$$

where Γ_0 is the inflow boundary assumed to be time independent to simplify, without loss of generality, the discussion. Similarly, the inflow boundary condition ϕ_{inflow} is assumed to be 0.

The finite element approximation of (3.7) becomes: find $\Phi(t) \in \mathbb{W}(\mathcal{T})$ for almost every $t \in [0, T]$, such that,

$$\begin{aligned} \int_{\Lambda} \left(\frac{\partial}{\partial t} \Phi(t)\right) W + \int_{\Lambda} ((\mathbf{u}(t) + \lambda \mathbf{R}) \cdot \nabla \Phi) W \\ = \int_{\Lambda} \lambda \text{sign}(\Phi) \left(1 - \left(\frac{\Phi}{C_\phi}\right)^2\right) W, \quad \forall W \in \mathbb{W}(\mathcal{T}), \end{aligned} \quad (3.8)$$

together with $\phi(0) = \Phi_0$ where $\Phi_0 \in \mathbb{W}(\mathcal{T})$ is an approximation of ϕ_0 . Here we denote $\mathbf{R} = \text{sign}(\Phi) \frac{\nabla \Phi}{|\nabla \Phi|}$.

3.4 Time discretization

The time discretization of (3.8) in time relies on explicit SSP methods [27]. We rewrite (3.1) as

$$\int_{\Lambda} \left(\frac{\partial}{\partial t} \Phi\right) W = \int_{\Lambda} L(\Phi) W, \quad \forall W \in \mathbb{W}(\mathcal{T}), \quad (3.9)$$

where

$$L(t, \Phi) = -(\mathbf{u}(t) + \lambda \mathbf{R}) \cdot \nabla \Phi + \lambda \text{sign}(\Phi) \left(1 - \left(\frac{\Phi}{C_\phi}\right)^2\right). \quad (3.10)$$

Over an integer $N > 0$, we denote by Φ^n , the approximation of $\Phi(t^n)$ where

$0 = t^0 < t^1 < \dots < t^N = T$, and $\delta t^n = t^n - t^{n-1}$. We use Runge-Kutta 3 method to derive a third order scheme:

$$\begin{aligned} \int_{\Lambda} \Phi^{(1)} W &= \int_{\Lambda} \left(\Phi^n + \delta t^{n+1} L(t^n, \Phi^n) \right) W \\ \int_{\Lambda} \Phi^{(2)} W &= \int_{\Lambda} \left(\frac{3}{4} \Phi^n + \frac{1}{4} \Phi^{(1)} + \frac{1}{4} \delta t^{n+1} L(t^{n+1}, \Phi^{(1)}) \right) W \\ \int_{\Lambda} \Phi^{(3)} W &= \int_{\Lambda} \left(\frac{1}{3} \Phi^n + \frac{2}{3} \Phi^{(2)} + \frac{2}{3} \delta t^{n+1} L(t^{n+\frac{1}{2}}, \Phi^{(2)}) \right) W, \quad \forall W \in \mathbb{W}(\mathcal{T}) \end{aligned} \quad (3.11)$$

and $\Phi^{n+1} = \Phi^{(3)}$ with applying the boundary conditions. This SSP method preserves strong stability property with higher order accuracy in time, but with the certain time step restriction, so called Courant-Friedrichs-Lewy(CFL) condition:

$$\delta t^{n+1} \leq C_{CFL} \max_{K \in \mathcal{T}} \|h_K^{-1}(\mathbf{u}(t^n) + \lambda \mathbf{R}^n)\|_{L^\infty(K)},$$

where C_{CFL} is a positive constant independent of \mathcal{T} , δt , and \mathbf{u} . $\mathbf{R}^n = \text{sign}(\Phi^n) \frac{\nabla \Phi^n}{|\nabla \Phi^n|}$ and h_K is the minimum length between the degree of freedoms in each K . We refer to [26, 45] for further details.

3.5 Entropy residual stabilization

The level set system (3.8) is stabilized to eliminate spurious oscillations due to sharp gradients in the exact solution. (See Figure 3.3 (a)-(b)). We start with a first order linear stabilization method by introducing a dissipation in the right hand side of (3.9) by

$$\int_{\Lambda} L(\Phi) W + \sum_K \int_K \mu_{|K}^{\text{Stab}} \nabla \Phi \nabla W, \quad (3.12)$$

where $\mu_{|K}^{\text{Stab}}$ is a local artificial stabilization coefficient given by

$$\mu_{|K}^{\text{Stab}}(t) := \mu_{|K}^{\text{Lin}}(t) = C_{\text{Lin}} \|h_K(\mathbf{u}(t) + \lambda \mathbf{R})\|_{L^\infty(K)}, \quad \forall K \in \mathcal{T}, \quad (3.13)$$

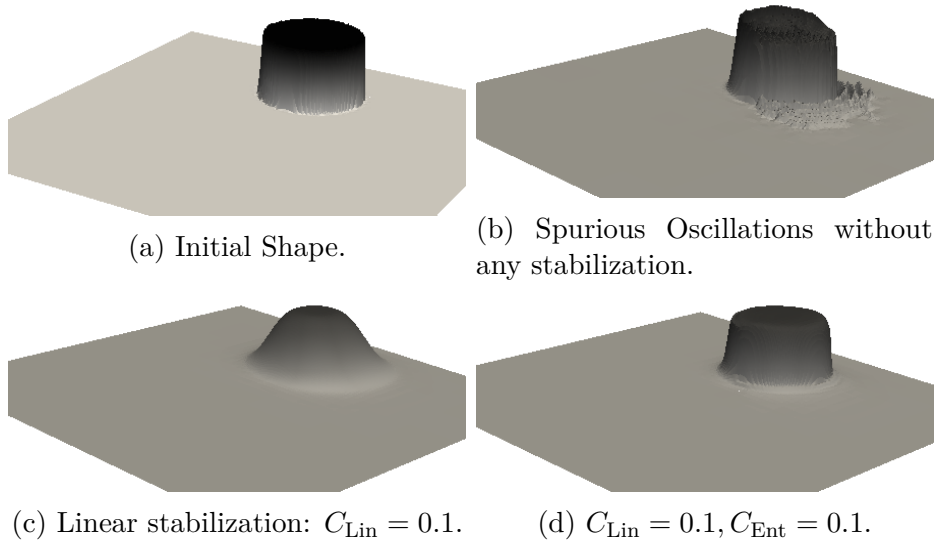


Figure 3.3: (a) The initial shape of the level set: the circle with a radius of 1, centered at $(0.5,0)$ in domain $\Lambda = (-1.1)^2$. (b)-(d) illustrates the shape of the level set after 1 cycle (360°) rotated by the velocity given at (3.20). We observe that the entropy residual method preserves the initial value more better.

with a small enough positive constant C_{Lin} . However, as illustrated in Figure 3.3 (c), this term introduces a large diffusion. We use the entropy viscosity stabilization method introduced in [10, 35]. The main idea of the method is to split the stabilization: when the level set is smooth, have the entropy viscosity stabilization, and when the level set is not smooth, have the first order viscosity. From here, the new artificial stabilization is given instead of (3.13) by,

$$\mu_{|K}^{\text{Stab}}(t) := \min(\mu_{|K}^{\text{Lin}}(t), \mu_{|K}^{\text{Ent}}(t)), \quad \forall K \in \mathcal{T}, \quad (3.14)$$

where $\mu_{|K}^{\text{Ent}}(t)$ denotes the new stabilization term called entropy viscosity defined below.

Let $E(\phi) : \mathbb{R}^d \rightarrow \mathbb{R}$ be any convex function, called entropy and $F(\phi) : \mathbb{R}^d \rightarrow \mathbb{R}$,

its associated entropy flux defined as satisfying,

$$F'(\phi) = \partial F(\phi)/\partial \phi := E'(\phi) \cdot \mathbf{u}. \quad (3.15)$$

With these definitions and a source term f , the entropy pair solves the advection equation

$$\frac{\partial}{\partial t} E(\phi) + \nabla \cdot F(\phi) - E'(\phi) f \leq 0,$$

with equality when ϕ is smooth. This leads to the definition of the entropy residual

$$R_E(\phi) := \partial_t E(\phi) + \nabla \cdot F(\phi) - E'(\phi) f.$$

Thus, this entropy residual $R_E(\phi)$ has large negative value near the interface of the level set and zero else where.

In our computation (3.11), we choose $E(\Phi) = \frac{1}{p} |\Phi|^p$, p even, and so,

$$\begin{aligned} F'(\Phi) &= (\mathbf{u}(t) + \lambda \mathbf{R}) \cdot E'(\Phi) = (\mathbf{u}(t) + \lambda \mathbf{R}) \cdot |\Phi|^{p-1}, \\ \nabla \cdot F(\Phi) &= (\mathbf{u}(t) + \lambda \mathbf{R}) \cdot |\Phi|^{p-1} \cdot \nabla \Phi = (\mathbf{u}(t) + \lambda \mathbf{R}) \cdot \nabla E(\Phi). \end{aligned}$$

Since we use SSP RK3 for time discretization, we need 3 different entropy residuals

$R_E^{(j)}(t)$, $j = 1, 2, 3$, defined as follows

1. $R_E^{(1)}(t^n) = 0$,
2. $R_E^{(2)}(t^{n+1}) = \frac{E(\Phi^{(1)}) - E(\Phi^n)}{\delta t^{n+1}} + (\mathbf{u}(t^{n+1}) + \lambda \mathbf{R}^{(1)}) \nabla E(\Phi^{(1)}) - E'(\Phi^{(1)}) \lambda \text{sign}(\Phi^{(1)}) \left(1 - \left(\frac{\Phi^{(1)}}{C_\phi}\right)^2\right)$,
3. $R_E^{(3)}(t^{n+\frac{1}{2}}) = \frac{E(\Phi^{(2)}) - E(\Phi^n)}{\delta t^{n+1}} + (\mathbf{u}(t^{n+\frac{1}{2}}) + \lambda \mathbf{R}^{(2)}) \nabla E(\Phi^{(2)})$

$$-E'(\Phi^{(2)})\lambda\text{sign}(\Phi^{(2)})\left(1 - \left(\frac{\Phi^{(2)}}{C_\phi}\right)^2\right).$$

The local entropy viscosity for each step is given by,

$$(\mu_K^{\text{Ent}})^j(t) := C_{\text{Ent}} h_K^2 |R_E^{(j)}(t)|_K / \|E(\Phi^{(j)}) - \bar{E}^{(j)}\|_{L^\infty(\Lambda)}, \quad \forall K \in \mathcal{T},$$

where C_{Ent} is a positive constant to choose, and $\bar{E}^{(j)} = \frac{1}{|\Lambda|} \int_\Lambda E(\Phi^{(j)}) d\mathbf{x}$. Figure 3.3 (d) illustrates the performance of the entropy viscosity stabilization.

3.6 Adaptive mesh refinement

We capture the interface described by the level set efficiently by taking advantage of using space adaptivity. We refine the cells near to the zero value of Φ , the solution to (3.8). More precisely, a cell K is refined if the value of the level set is

$$|\Phi(\mathbf{x}_K, t)| \leq \varepsilon_R := C_\phi \tanh(\mathbf{x}_R), \quad (3.16)$$

where \mathbf{x}_K is the barycenter of K and the choice of the parameter \mathbf{x}_R is discussed in Section 3.7.

3.7 Values of numerical parameters

First, we start from tuning the constant λ , which determines the reinitialization speed. We can determine the λ by using the CFL conditional constants for the main

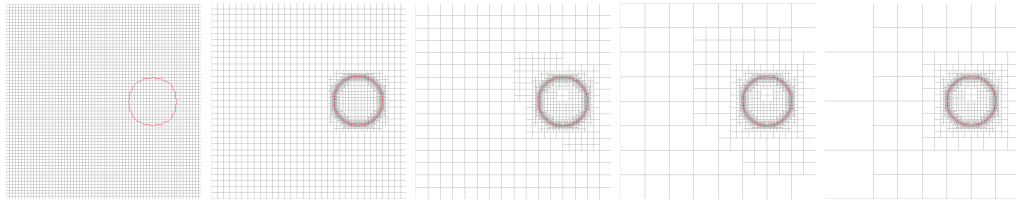


Figure 3.4: Adaptivity: Refining meshes with the given initial level set at Figure 3.3.

Parameter	C_λ	m	\mathbf{x}_H	\mathbf{x}_S	\mathbf{x}_R	C_{Lin}	C_{Ent}	p
Value	0.01	1.	1.25	0.5	2.	0.1	0.1	20

Table 3.1: Suggested numerical parameters which are appropriate for our algorithm. Values of $\varepsilon_H, \varepsilon_S$, and ε_R according to above values $\mathbf{x}_H, \mathbf{x}_S$ and \mathbf{x}_R are shown at Figure 3.5.

time step ∂t and the virtual time step $\partial \tau$, C_{CFL} and $C_{\text{CFL}}^{\text{Reinit}}$ respectively. Using the relations, we get

$$\lambda(t) = \frac{\partial \tau}{\partial t} \approx \max_{K \in \mathcal{T}} \frac{C_{\text{CFL}}^{\text{Reinit}} \|\mathbf{u}(t)\|_{L^\infty(K)}}{C_{\text{CFL}}} \approx \max_{K \in \mathcal{T}} C_\lambda \|\mathbf{u}(t)\|_{L^\infty(K)}, \quad (3.17)$$

where C_λ is some positive constant to adjust the speed of the reinitialization, typically set to 0.1. If $C_\lambda = 0$, reinitialization is turned off.

Secondly, we have to tune C_ϕ in the definition of the cut off function, given at (3.6). We choose $C_\phi := mh$, where m is a positive constant. Note that $|\nabla \phi| \approx 1$ is preserved only near at $-0.5C_\phi \leq x \leq 0.5C_\phi$ due to the value of \tanh . (See Figure 3.5).

Recall the constants for the sign function (3.4) and the linearize function defined

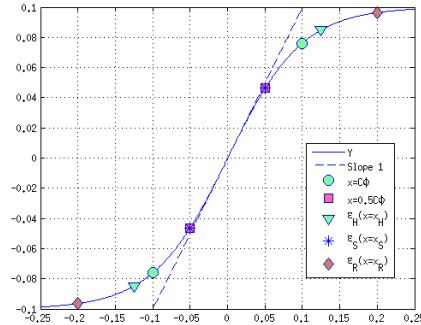


Figure 3.5: Plots $Y = C_\phi \tanh(x)$ with $C_\phi = 0.1$, a line with slope 1 and the positions of several constants given at Table 3.1.

at (4.13),

$$\varepsilon_H = C_\phi \tanh(\mathbf{x}_H), \quad \varepsilon_S = C_\phi \tanh(\mathbf{x}_S),$$

and the choices of \mathbf{x}_H and \mathbf{x}_S are suggested in Table 3.1 with the values depicted at Figure 3.5. We also set \mathbf{x}_R for the adaptivity in (3.16).

We now discuss the values of the constants C_{Lin} and C_{Ent} appearing in Section 3.5. First, we set $C_{\text{Ent}} = \infty$ and get the smallest C_{Lin} so that the computed solution has no spurious oscillations. Then we reduce C_{Ent} , as much as possible keeping the computed solution spurious oscillation free. Suggested values for our algorithm is given at Table 3.1. More details to tune these constants are provided at [35].

3.8 Numerical results

For the validation of the level set system with proposed reinitialization and stabilization method that we discussed in previous sections, we consider several classical test problems.

δt	Dofs	$l^2(L^2(\Lambda))$ Error	Rate	$l^\infty(L^2(\Lambda))$ Error	Rate
0.005	625	0.000000017674	0.0000	0.000000095173	0.0000
0.0025	2401	0.000000001754	3.3329	0.000000009057	3.3935
0.00125	9409	0.000000000154	3.5052	0.000000000751	3.5926
0.000625	37249	0.000000000014	3.4581	0.000000000070	3.4294
0.0003125	148225	0.000000000002	3.2142	0.000000000008	3.1654

Table 3.2: Convergence rate for SSP RK3 on the exact solution given by (3.18). The expected third order of convergence is observed.

3.8.1 Error convergence test

In order to validate our implementation of the SSP RK3 scheme (3.11) applied to the level set system, we consider the exact solution given by

$$\phi(x, y, t) := 2 + \sin(\pi xt) \sin(\pi yt), \quad (3.18)$$

on $(0, 1)^2 \times [0, T]$. The transport velocity \mathbf{u} is chosen to be

$$\mathbf{u}(x, y, t) := \begin{pmatrix} \sin(t+x) \sin(t+y) \\ \cos(t+x) \cos(t+y) \end{pmatrix},$$

and the final time $T = 0.2$. The computations are performed in \mathbb{Q}^3 continuous finite element and we compute the $l^\infty(L2(\Lambda))$ and $l2(L2(\Lambda))$ error of ϕ . The space discretization consists of uniform refinement of an initial subdivision made of 625 degree of freedoms. See Table 3.2 for the results.

Figure 3.6 illustrates the other test for the performance of the method, the Single Vortex problem. In this case, the initial level set ϕ_0 is the distance function to the

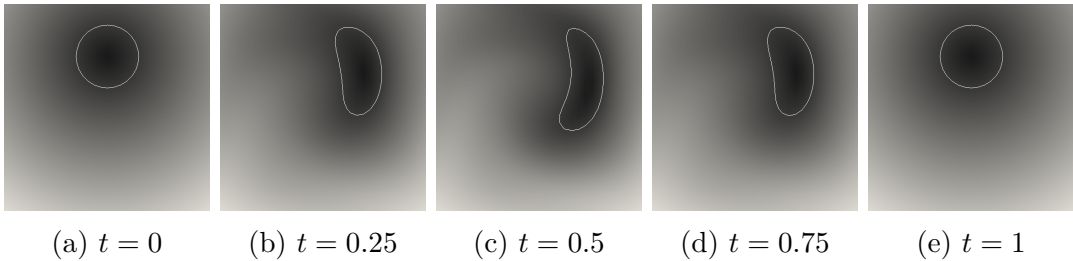


Figure 3.6: Single Vortex convergence test for $t = 0, 0.25, 0.5, 0.75$, and 1 . Solid line indicates the contour of zero level set value. In this case, $C_\lambda = C_{\text{Lin}} = C_{\text{Ent}} = 0$.

δt	Dofs	$l^\infty(L^2(\Lambda))$ Error	Rate
0.01	169	0.02264405	0.0000
0.005	625	0.00213107	3.4095
0.0025	2401	0.00020880	3.3514
0.00125	9409	0.00002218	3.2350

Table 3.3: Convergence rate of the error $\|\phi(T_C) - \phi_0\|_{L^2}$ for the Single Vortex test in Figure 3.6. L^2 error is calculated at the time $T = 1$. The expected third order of convergence is recovered.

circle with a radius of 0.15 and center $(0.5, 0.75)$ in $\Lambda := (0, 1)^2$. A periodic velocity

$$\mathbf{u}(x, y, t) := \begin{pmatrix} -\sin^2(\pi x) \sin(2\pi y) \cos(\pi t/T_C) \\ \sin^2(\pi y) \sin(2\pi x) \cos(\pi t/T_C) \end{pmatrix} \quad (3.19)$$

is prescribed in such a way that $\phi(x, y, n * T_C) = \phi^0(x, y)$, where $n = 1, 2, \dots$. Table 3.3 presents the convergence rate of the error $\|\phi(T_C) - \phi_0\|_{L^2}$ with $T_C = 1$.

3.8.2 Circle rotation

We consider the circle which is initially centered at $(0.5, 0)$ with a radius of 0.25 in the given domain $\Lambda = (-1, 1)^2$, i.e

$$\phi_0 = -(\sqrt{(x - 0.5)^2 + y^2} - 0.25).$$

The circle is rotated in the domain with the divergence free velocity field,

$$\mathbf{u}(x, y, t) := \begin{pmatrix} -\sqrt{x^2 + y^2} \sin(\arctan(y/x)) \\ \sqrt{x^2 + y^2} \cos(\arctan(y/x)) \end{pmatrix}. \quad (3.20)$$

We compare the initial circle with the computed level set after one cycle (360°). Computation is given with approximately 5,000 adaptive meshes, uniform time step

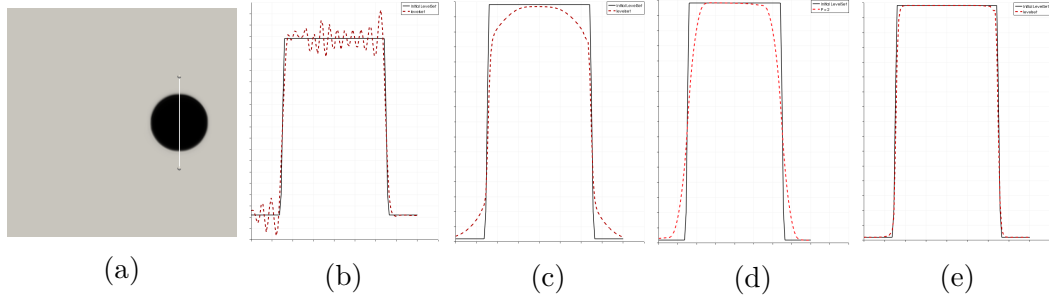


Figure 3.7: Illustrates the value of the level set which is plotted over the line $(0.5, -0.4) - (0.5, 0.4)$, see (a). For (b)-(e), the solid line indicates the initial value ϕ_0 and the dotted line is the value of ϕ after one cycle. (b) Without any stabilization ($C_{\text{Lin}} = C_{\text{Ent}} = 0$) and without reinitialization ($\lambda = 0$). (c) Only adding the first order linear stabilization term with $C_{\text{Lin}} = 0.1$. No oscillations are observed but ϕ is diffused by first order linear stabilization at the corners. (d) With the entropy residual stabilization method. $C_{\text{Lin}} = 0.1$ and $C_{\text{Ent}} = 0.1$. (e) Finally also adding reinitialization with $\lambda = 0.1$.

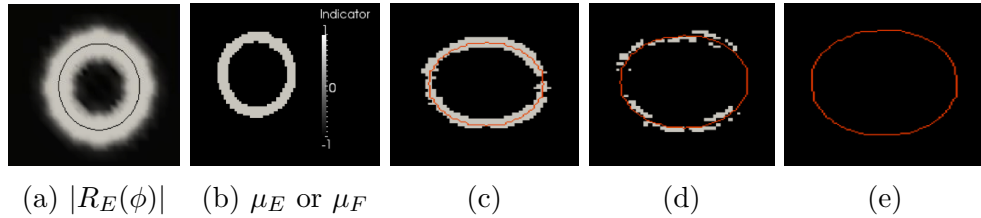


Figure 3.8: (a) The value of the entropy residual $|R_E(\phi)|$ (white: large; black: low). As expected, the entropy residual is large near the interface (solid line), where ϕ is not smooth. (b) Choice of viscosity: μ_E (black), μ_F (white). Again, as expected, the linear viscosity μ_F is active where ϕ is not smooth (near the interface). (c)-(e) depicts the solution after 5, 15, and 20 time steps. We see that the diffusion from the algorithm smooths ϕ near the interface in such a way that only the entropy viscosity μ_E is active.

$\delta t = 0.001$, and the constants in Table 3.1. Figure 3.7 illustrates the value of the level set after one cycle compared with the initial data and given different conditions. We observe the benefit of the entropy residual stabilization and the reinitialization method as the initial shape is recovered after one cycle. Figure 3.8 shows the verifi-

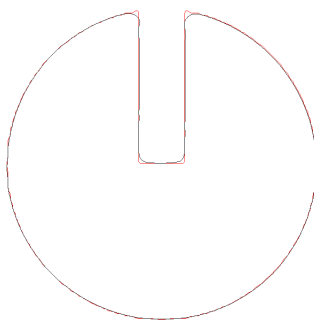


Figure 3.9: Comparing the contour of $\phi_0 = 0$ (outside) to the contour of $\phi = 0$ after one cycle, 360° (inside).

cation of the idea of entropy residual stabilization method.

3.8.3 Slotted Disk

Now the initial data(Figure 3.9) is a slotted disk centered at $(0.5, 0)$ with a radius of 0.25, a notch width of 0.075, and a slot length of 0.25 in the given domain $\Lambda = (-1, 1)^2$. Again, the disk is rotated in the domain with the divergence free velocity field (3.20) and we compare the initial disk with the computed level set after one cycle (360°), see Figure 3.9. Computation is given with approximately 5,000 adaptive meshes, uniform time step $\delta t = 0.001$, and the constants in Table 3.1. Figure 3.10 illustrates the result that the Slotted Disk conserves the value during the cycle compare to the initial data.

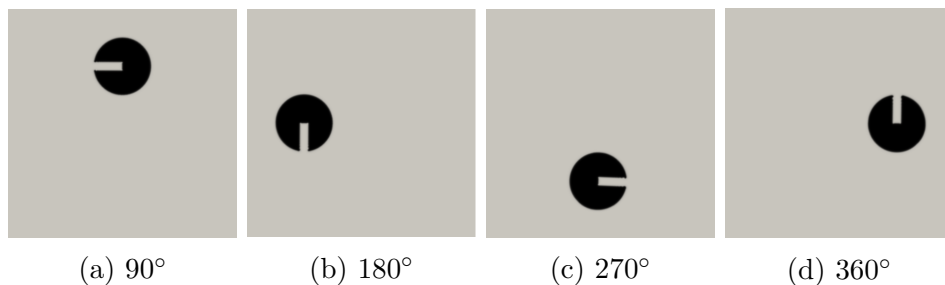


Figure 3.10: Rotating Slotted Disk at each position.

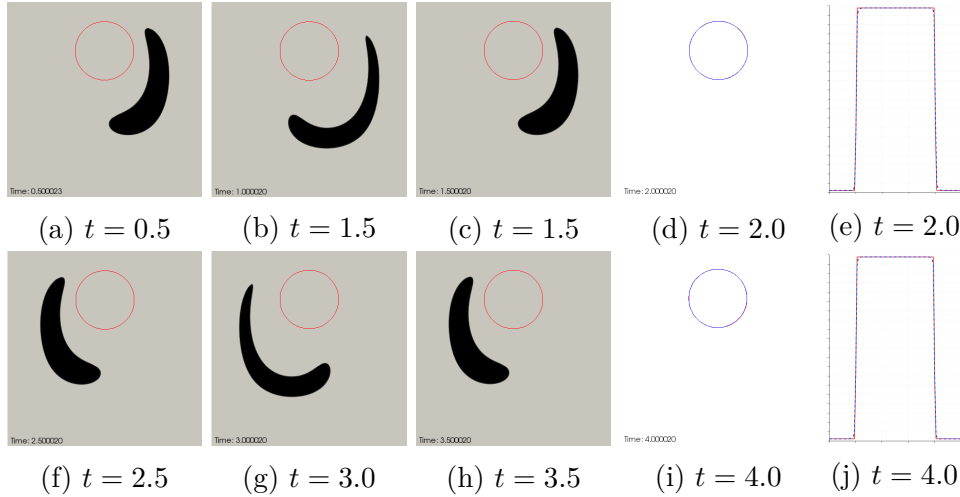


Figure 3.11: Single Vortex: Illustrates the deformation of the initial circle in corresponding time from $t = 0$ to $t = 4$. (a)-(d) and (f)-(i) shows the shape of the vortex in each time compare to the initial circle. (d) and (i) are comparing the contour of $\phi(t) = 0$ and $\phi^0 = 0$ at $t = 2$ and $t = 4$. (e) and (j) plots the level set value over the line $(-0.3, 0.5) - (0.3, 0.5)$, at $t = 2$ and $t = 4$ respectively, and confirms that the computed results are almost identical with the initial data. Compare with Figure 3.6, an another Single Vortex example we performed without any reinitialization, cut off function, and any stabilization.

3.8.4 Single Vortex

The Single Vortex problem consists of the deformation of an initial circle with a reversible vortex flow. Now, $\Lambda = (0, 1)^2$, the initial circle is centered at $(0.5, 0.75)$ and has a radius of 0.15. It is deformed according to the divergence free velocity field described at (3.19), and for example, here the time period $T_C = 2$ indicates that the velocity will reverse at $t = 1$ and the circle will be repositioned at the initial position at $t = 2$. Computation is given with approximately 10,000 adaptive meshes, uniform time step $\delta t = 0.001$ with $T = 4$, and the constants in Table 3.1. Figure 3.11 provides the shape of the interface at several time.

In addition, Figure 3.12 illustrates the 3D problem, when a sphere initially cen-

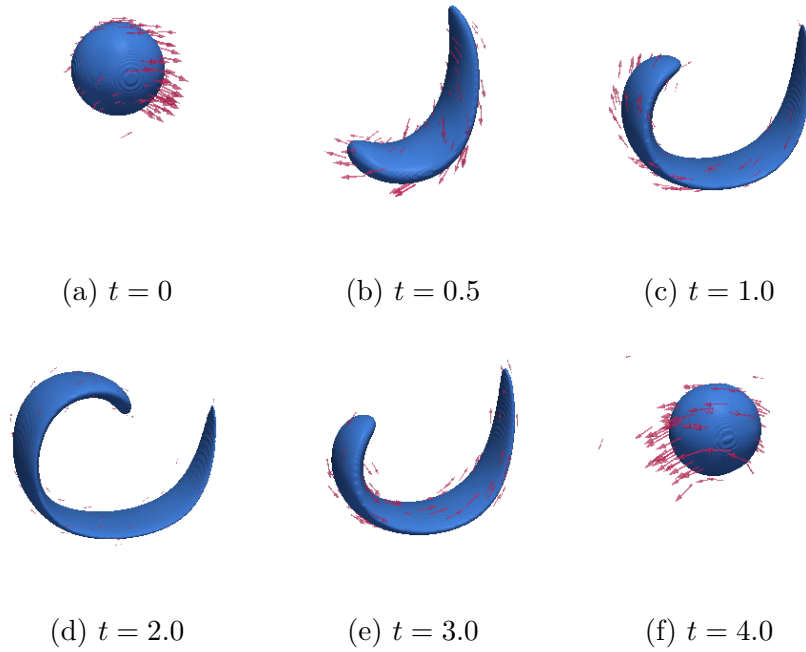


Figure 3.12: Single Vortex 3D: Deformation of the sphere at several times. Vectors indicate the velocity field.

tered at $(0.5, 0.75, 0.)$ with a radius of 0.15 is deformed in the domain $\Lambda = (0, 1)^3$. We use the same divergence free velocity field and setup as 2D problem but adding $\mathbf{u}_3 = 0$, and redefined $T_C = 4$. The numerical constants are same as for the 2D problem.

4. NUMERICAL SIMULATIONS OF TWO PHASE FLOWS

We turn our focus on the numerical simulations of two phase flows with the level set method (cf. [46]). First, we give the mathematical model for a non-mixing two phase flow system with capillary force. Each fluid is assumed to be incompressible.

4.1 Mathematical model

Recall $\Lambda \subset \mathbb{R}^d$ ($d = 2, 3$) is the computational domain and $T > 0$ is the computational time. The cavity Λ is filled by two non-mixing fluids evolving over time. We denote by $\Omega^+(t)$ and $\Omega^-(t)$, the open sets describing the regions occupied by each fluid.

In $\Lambda \times [0, T]$, the velocity field $\mathbf{u} : \Lambda \times [0, T] \rightarrow \mathbb{R}^d$ and the pressure $p : \Lambda \times [0, T] \rightarrow \mathbb{R}$ are assumed to satisfy the incompressible Navier-Stokes system:

$$\rho \left(\frac{\partial}{\partial t} \mathbf{u} + \mathbf{u} \cdot \nabla \mathbf{u} \right) - 2 \operatorname{div} (\mu \nabla^S \mathbf{u}) + \nabla p = \rho \mathbf{g} \quad \text{in } \Lambda \times [0, T] \quad (4.1a)$$

$$\operatorname{div}(\mathbf{u}) = 0 \quad \text{in } \Lambda \times [0, T], \quad (4.1b)$$

where \mathbf{g} is a vertical downward gravity field and $\rho, \mu : \Lambda \times [0, T] \rightarrow \mathbb{R}$ are the density and viscosity of the two phase flow, and $\nabla^S \mathbf{u} = \frac{1}{2}(\nabla \mathbf{u} + \nabla \mathbf{u}^T)$.

Continuity of the velocities and capillary forces are imposed at the interface $\Sigma(t) := (\overline{\Omega^+(t)} \cap \overline{\Omega^-(t)}) \setminus \partial \Lambda$:

$$[\mathbf{u}] = 0 \quad \text{and} \quad [2\mu \nabla^S \mathbf{u} - p] \mathbf{n} = \sigma \kappa \mathbf{n} \quad \text{on} \quad \Sigma(t), \quad (4.2)$$

where $[\cdot]$ denotes the jump across the interface $\Sigma(t)$, σ is the surface tension coefficient, \mathbf{n} is the unit outer normal of Ω^+ , and κ is the total curvature of Σ (sum of

principal curvatures) with the convention that the curvature is negative when Ω^+ is a circle or sphere. Relations (4.1) and (4.2) are supplemented by boundary conditions. The boundary $\partial\Lambda$ is split into two parts $\partial\Lambda := \Gamma_N(t) \cup \Gamma_D(t)$ with $\Gamma_N(t) \cap \Gamma_D(t) = \emptyset$ and for given $\mathbf{f}_N : \Gamma_N(t) \rightarrow \mathbb{R}^d$, $\mathbf{f}_D : \Gamma_D(t) \rightarrow \mathbb{R}^d$, we impose

$$(2\mu\nabla^S \mathbf{u} - p) \boldsymbol{\nu} = \mathbf{f}_N \quad \text{on} \quad \Gamma_N \quad \text{and} \quad \mathbf{u} = \mathbf{f}_D \quad \text{on} \quad \Gamma_D, \quad (4.3)$$

where $\boldsymbol{\nu}$ denotes the toward unit normal to Λ . For simplicity, we assume that $\text{measure}(\Gamma_N) > 0$ and $\text{measure}(\Gamma_D) > 0$, for otherwise, extra constraints on the velocity or pressure are required. Finally, the velocity is provided initially:

$$\mathbf{u}(\cdot, 0) = \mathbf{u}_0 \quad \text{in} \quad \Lambda, \quad (4.4)$$

where $\mathbf{u}_0 : \Lambda \rightarrow \mathbb{R}^d$ is a given initial velocity.

4.2 Space discretization using Finite Elements

We use the conforming finite element method for the space discretization. Recalling the definition of $\mathbb{W}(\mathcal{T})$ provided in Section 3.3, we define the finite element spaces for the velocity and the pressure approximation by

$$\mathbb{V}(\mathcal{T}) := \{V \in C^0(\bar{\Lambda}) \rightarrow \mathbb{R}^d \mid V|_{\Gamma_D} = 0, V|_K \in [\mathbb{Q}^2(K)]^d, \forall K \in \mathcal{T}\}, \quad (4.5)$$

$$\mathbb{M}(\mathcal{T}) := \{Q \in C^0(\bar{\Lambda}) \rightarrow \mathbb{R} \mid Q|_K \in \mathbb{Q}^1(K), \forall K \in \mathcal{T}\}, \quad (4.6)$$

The above pair of finite element spaces is known as the Taylor-Hood finite element approximation which satisfies a discrete inf-sup condition (cf. [24, 49]).

Hence the space discretization of (4.1) is ready. Find $\mathbf{U}(t) \in \mathbb{V}(\mathcal{T})$ and $P(t) \in$

$\mathbb{M}(\mathcal{T})$ for almost every $t \in (0, T]$, such that,

$$\begin{aligned} \int_{\Lambda} \rho(\Phi(t)) \frac{\partial}{\partial t} \mathbf{U}(t) \mathbf{V} \, d\mathbf{x} + 2 \int_{\Lambda} \mu(\Phi(t)) (\nabla^S \mathbf{U}(t) : \nabla^S \mathbf{V}) \, d\mathbf{x} \\ - \int_{\Lambda} P(t) \operatorname{div}(\mathbf{V}) \, d\mathbf{x} = \int_{\Lambda} \rho(\Phi(t)) \mathbf{g}(t) \, d\mathbf{x} \quad \forall \mathbf{V} \in \mathbb{V}(\mathcal{T}), \end{aligned} \quad (4.7)$$

with

$$\int_{\Lambda} Q \operatorname{div}(\mathbf{U}) = 0, \quad \forall Q \in \mathbb{M}(\mathcal{T}). \quad (4.8)$$

4.3 Time discretization

To discretize Navier-Stokes system (4.1)-(4.4) in time, we propose an rotational incremental pressure correction scheme [13, 48, 32, 33] to decouple the velocity and the pressure together with a second order backward differentiation formula (BDF2) for the time discretization. Let $0 =: t^0 < t^1 < t^2 < \dots < t^N := T$ be a subdivision of the time interval $[0, T]$. Given the initial condition $\mathbf{u}(0) := \mathbf{U}^0$, where $\mathbf{U}^0 \in \mathbb{V}(\mathcal{T})$ is an approximation of \mathbf{u}_0 , the algorithm requires an initial pressure $p(0)$ and we set, $P^{-1} = P^0 = p(0)$, where $P^{-1}, P^0 \in \mathbb{M}(\mathcal{T})$. We denote by \mathbf{U}^n, P^n , the approximation of $\mathbf{U}(t^n), P(t^n)$, respectively.

We start with the BDF2 approximation of the time derivative

$$\frac{\partial}{\partial t} \mathbf{U}(\cdot, t^{n+1}) \approx \mathbf{U}_{\text{BDF2}}^{n+1} := \frac{1}{\delta t^{n+1}} \left(\frac{1 + 2\gamma_{n+1}}{1 + \gamma_{n+1}} \mathbf{U}^{n+1} - (1 + \gamma_{n+1}) \mathbf{U}^n + \frac{\gamma_{n+1}^2}{1 + \gamma_{n+1}} \mathbf{U}^{n-1} \right),$$

with variable time steps $\delta t^{n+1} := t^{n+1} - t^n$, see [19]. We also use the notation $(\mathbf{U}^n)^* := \mathbf{U}^n + \gamma^n (\mathbf{U}^n - \mathbf{U}^{n-1})$ and $\gamma_{n+1} := \frac{\delta t^{n+1}}{\delta t^n}$ for the extrapolation. Now, we seek the velocity \mathbf{U}^{n+1} and the pressure P^{n+1} recursively in three steps as proposed in [30]: Given \mathbf{U}^n, Ψ^n and P^n , the velocity approximation $\mathbf{U}^{n+1} \in \mathbb{V}(\mathcal{T})$ is obtained

for each step n via the relation,

$$\begin{aligned}
& \int_{\Lambda} \rho(\Phi^{n+1}) \mathbf{U}_{\text{BDF}_2}^{n+1} \mathbf{V} \, d\mathbf{x} + 2 \int_{\Lambda} \mu(\Phi^{n+1}) (\nabla^S(\mathbf{U}^{n+1}) : \nabla^S \mathbf{V}) \, d\mathbf{x} \\
&= - \int_{\Lambda} \rho(\Phi^{n+1}) ((\mathbf{U}^n)^* \cdot \nabla \mathbf{U}^n) \mathbf{V} \, d\mathbf{x} + \int_{\Lambda} (P^n + \frac{4}{3} \Psi^n - \frac{1}{3} \Psi^{n-1}) \text{div}(\mathbf{V}) \, d\mathbf{x} \\
& \quad + \int_{\Lambda} \rho(\Phi^{n+1}) \mathbf{g}(t^{n+1}) \, d\mathbf{x}, \quad \forall \mathbf{V} \in \mathbb{V}(\mathcal{T}), \quad (4.9)
\end{aligned}$$

where $\Psi^n \in \mathbb{M}(\mathcal{T})$ is the pressure rotational increment approximation, with the convention $\Psi^0 = 0$, i.e.

$$\Psi^{n+1} = P^{n+1} - P^n + \mu_{\min}(\Phi^{n+1}) \text{div}(\mathbf{U}^{n+1}), \quad (4.10)$$

with $\mu_{\min}(\Phi^{n+1}) := \min_{\mathbf{x} \in \Lambda} \mu(\Phi^{n+1}(\mathbf{x}))$. Here Φ^{n+1} is the approximation of the level set function at time t^{n+1} given by (3.9)-(3.11) in Section 3.4, where $\mathbf{u}(t^n)$, $\mathbf{u}(t^{n+\frac{1}{2}})$ and $\mathbf{u}(t^{n+1})$ in (3.10) are replaced by \mathbf{U}^n and second order extrapolation of $\mathbf{U}^{n+\frac{1}{2}}$ and \mathbf{U}^{n+1} . $\rho(\Phi^{n+1})$ and $\mu(\Phi^{n+1})$ are given by

$$\rho(\Phi^{n+1}) = \rho^+ \frac{1 + H(\Phi^{n+1})}{2} + \rho^- \frac{1 - H(\Phi^{n+1})}{2} \quad (4.11)$$

$$\mu(\Phi^{n+1}) = \mu^+ \frac{1 + H(\Phi^{n+1})}{2} + \mu^- \frac{1 - H(\Phi^{n+1})}{2}, \quad (4.12)$$

where, ρ^{\pm}, μ^{\pm} are the density/viscosity in Ω^{\pm} , and

$$H(\Phi) = \begin{cases} 1, & \Phi > \varepsilon_H \\ -1, & \Phi < -\varepsilon_H \\ \frac{\Phi}{\varepsilon_H}, & |\Phi| < \varepsilon_H \end{cases} \quad (4.13)$$

as suggested for a parameter $\varepsilon_H > 0$ in [55], we define $\varepsilon_H := C_{\phi} \tanh(\mathbf{x}_H)$ with \mathbf{x}_H

suggested in Section 3.7. To penalize compressible velocities, we add

$$\sum_{K \in \mathcal{T}} \int_K \alpha_{|K}^{\text{Comp}} \nabla(\text{div} \mathbf{U}) \cdot \mathbf{V},$$

where

$$\alpha_{|K}^{\text{Comp}} := C_{\text{Comp}}(\mu(\Phi^{n+1}) + \rho(\Phi^{n+1}) \|h_K \mathbf{U}\|_{L^\infty(K)}), \quad \forall K \in \mathcal{T}$$

in the left hand side of (4.9) with $C_{\text{Comp}} = 0.2$. If the fluid is considered as air, we add a local first order linear viscosity stabilization term,

$$\sum_{K \in \mathcal{T}} \int_K C_{\text{Lin}} \rho(\Phi^{n+1}) \|h_K \mathbf{U}\|_{L^\infty(K)} (\nabla^S \mathbf{U} : \nabla^S \mathbf{V}),$$

with a positive constant $C_{\text{Lin}} = 0.2$.

The second step, namely the pressure correction step, we find the approximation of the pressure increment $\Psi^{n+1} \in \mathbb{M}(\mathcal{T})$ such that

$$\int_{\Lambda} \nabla \Psi^{n+1} \nabla Q \, d\mathbf{x} = -\frac{3\rho_{\min}(\Phi^{n+1})}{2\delta t^{n+1}} \int_{\Lambda} \text{div}(\mathbf{U}^{n+1}) Q \, d\mathbf{x}, \quad \forall Q \in \mathbb{M}(\mathcal{T}), \quad (4.14)$$

where $\rho_{\min}(\Phi^{n+1}) := \min_{\mathbf{x} \in \Lambda} \rho(\Phi^{n+1}(\mathbf{x}))$.

Finally, the third step is to update the pressure $P^{n+1} \in \mathbb{M}(\mathcal{T})$ by solving,

$$\int_{\Lambda} P^{n+1} Q \, d\mathbf{x} = \int_{\Lambda} (P^n + \Psi^{n+1} - \mu_{\min}(\Phi^{n+1}) \text{div}(\mathbf{U}^{n+1})) Q \, d\mathbf{x}, \quad \forall Q \in \mathbb{M}(\mathcal{T}). \quad (4.15)$$

4.4 Surface Tension

Recall that the interface condition of Navier Stokes system (4.2) reads

$$[2\mu \nabla^S \mathbf{u} - p] \mathbf{n} = \sigma \kappa \mathbf{n} \quad \text{on} \quad \Sigma(t), \quad (4.16)$$

with \mathbf{n} the unit outer normal of Ω^+ . To discretize the surface tension term $\sigma\kappa\mathbf{n}$, we proceed as follow. We define the tangential gradient of a vector function $\mathbf{u} : \Sigma \rightarrow \mathbb{R}^d$ by,

$$\nabla_{\Sigma}\mathbf{u} := \nabla\tilde{\mathbf{u}}(\mathbf{I} - \mathbf{n} \otimes \mathbf{n})|_{\Sigma}, \quad (4.17)$$

where $\tilde{\mathbf{u}}$ is an extension of \mathbf{u} to an open neighborhoods of Σ . In particular, $\nabla_{\Sigma}\mathbf{X} = \mathbf{I} - \mathbf{n} \otimes \mathbf{n}$, where \mathbf{X} is the identity on Σ . The Laplace-Beltrami operator of \mathbf{u} is defined as

$$\Delta_{\Sigma}\mathbf{u}(\mathbf{x}) := \nabla_{\Sigma} \cdot (\nabla_{\Sigma}\mathbf{u}(\mathbf{x})), \quad \mathbf{x} \in \Sigma, \quad (4.18)$$

and recalling the fundamental relation, $\Delta_{\Sigma}\mathbf{X} = \kappa\mathbf{n}$, we obtain,

$$\begin{aligned} \int_{\Sigma} \sigma\kappa\mathbf{n} \cdot \mathbf{v} \, d\Sigma &= \int_{\Sigma} \sigma\Delta_{\Sigma}\mathbf{X} \cdot \mathbf{v} \, d\Sigma \\ &= - \int_{\Sigma} \sigma\nabla_{\Sigma}\mathbf{X} \cdot \nabla_{\Sigma}\mathbf{v} \, d\Sigma + \int_{\partial\Sigma} \sigma\partial_{\partial\Sigma}\mathbf{X} \cdot \mathbf{v} \, d\partial\Sigma, \end{aligned} \quad (4.19)$$

for any smooth function $\mathbf{v} : \Sigma \rightarrow \mathbb{R}^d$. Here $\partial\Sigma$ is the tangent line of Σ , given by the intersection between the interface Σ and boundary of Λ , in the direction tangential to the interface. In our case, the interface is either close or $\partial_{\partial\Sigma}\mathbf{X} = 0$ on $\partial\Sigma$, therefore $\int_{\partial\Sigma} \sigma\partial_{\partial\Sigma}\mathbf{X} \cdot \mathbf{v} \, d\partial\Sigma = 0$.

We now discuss a time discretization for the above relation, which leads to a semi-implicit scheme. For this, we follow [6, 18, 38], and assume that the interface moves along with the fluid, i.e $\dot{\mathbf{X}} = \mathbf{u}$. Then, we advance in time from t^n to t^{n+1} via a semi-implicit Euler method to find the new position by, $\mathbf{X}^{n+1} = \mathbf{X}^n + \delta t^{n+1}\mathbf{U}^{n+1}$, where $\mathbf{X}^{n+1} \approx \mathbf{X}(t^{n+1})$. In the view of (4.19) and applying space and time discretization

introduced in previous sections, we obtain

$$\begin{aligned} \int_{\Lambda} \sigma \kappa \mathbf{n}^{n+1} \cdot \mathbf{v} \delta(\Sigma^{n+1}, \mathbf{x}) \, d\mathbf{x} &\approx -\delta t^{n+1} \int_{\Lambda} \sigma \nabla_{\Sigma^{n+1}} \mathbf{U}^{n+1} \cdot \nabla_{\Sigma^{n+1}} \mathbf{V} \cdot \delta_{\varepsilon}(\Sigma^{n+1}, \mathbf{x}) \, d\mathbf{x} \\ &\quad - \int_{\Lambda} \sigma (\mathbf{I} - \mathbf{n} \otimes \mathbf{n}) \cdot \nabla_{\Sigma^{n+1}} \mathbf{V} \cdot \delta_{\varepsilon}(\Sigma^{n+1}, \mathbf{x}) \, d\mathbf{x}, \quad \forall \mathbf{V} \in \mathbb{V}(\mathcal{T}), \end{aligned}$$

where δ_{ε} is a regularization of the dirac measure δ of Σ .

The regularized continuous delta function δ_{ε} is defined as,

$$\delta_{\varepsilon}(\text{dist}(\Sigma, \mathbf{x})) = \begin{cases} \frac{1}{ch} \omega\left(\frac{1}{ch} \text{dist}(\Sigma, \mathbf{x})\right), & |\text{dist}(\Sigma, \mathbf{x})| < ch \\ 0, & \text{otherwise} \end{cases} \quad (4.20)$$

where c is a positive constant and $\delta_{\varepsilon} \in C(\mathbb{R})$. There are several suitable choices for ω , but in our study we use the linear hat function,

$$\omega(\xi) = 1 - |\xi|. \quad (4.21)$$

In Section 3.2 we introduced the level set function with a cut off filter (3.6), which results on a non-distance level set function Φ . In this reason, (4.20) is not the appropriate approximation of the delta function, since

$$\int_{-ch}^{ch} \delta_{\varepsilon}(\phi(x)) \neq 1. \quad (4.22)$$

To get over this issue, we rescale the delta function to read,

$$\delta_{\varepsilon}(\Phi) = \begin{cases} \frac{1}{\tilde{\varepsilon}} \omega\left(\frac{\Phi}{\tilde{\varepsilon}}\right) |\nabla \Phi|, & |\Phi| < \tilde{\varepsilon} \\ 0, & \text{otherwise} \end{cases} \quad (4.23)$$

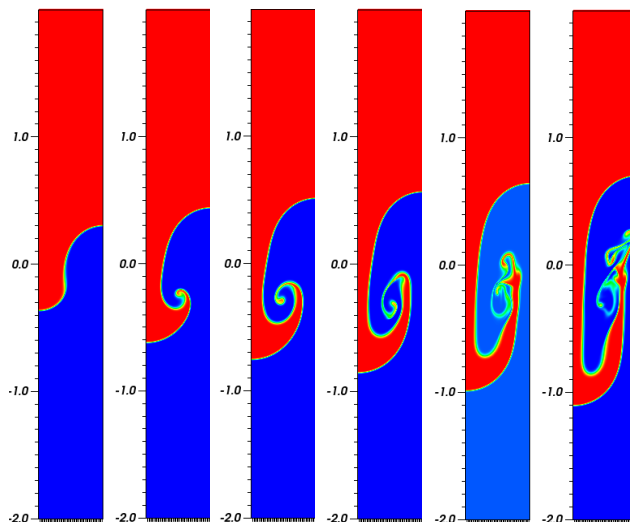


Figure 4.1: The interface is shown at times 1, 1.5, 1.75, 2, 2.25, and 2.5. Compare the result with [30].

where $\tilde{\varepsilon} = \Phi(\varepsilon)$, and finally, this modification satisfies

$$\int_{\Lambda} f(\mathbf{x}) \delta_{\tilde{\varepsilon}}(\phi(\mathbf{x})) |\nabla \phi| d\mathbf{x} = \int_{\Sigma} f(\mathbf{x}) d\Sigma. \quad (4.24)$$

We refer to [20, 52] for the related error analysis.

4.5 Numerical results

We now illustrate the performance of the method described in previous sections on several test problems.

4.5.1 *Rayleigh-Taylor instability*

We implement the development of a Rayleigh-Taylor instability problem documented in [53], and reproduced at [30], by using the projection method with variable density that we proposed at the previous sections. The computational domain is rectangle $(-0.5, 0.5) \times (-2, 2)$, but restricted to $(0, 0.5) \times (-2, 2)$ taking advantage of the problem symmetry. The initial position of the perturbed interface is

$\eta(\mathbf{x}) = -0.1 \cos(2\pi\mathbf{x})$, and the density ratio is 3 with the heavy fluid on top. The Atwood number according to Tryggvason’s definition,

$$A_t := (\rho_0^{\max} - \rho_0^{\min}) / (\rho_0^{\max} + \rho_0^{\min}) = 0.5, \quad (4.25)$$

with $\rho_0^{\max} := \max_{\mathbf{x} \in \Omega} \rho_0(\mathbf{x})$. The transition between the two fluids is regularized as follows

$$\frac{\rho(x, y, t = 0)}{\rho_0^{\min}} = 2 + \tanh\left(\frac{y - \eta(x)}{0.01}\right), \quad (4.26)$$

to match the setup in [30]. Figure 4.1 shows the results of our algorithm at times 1, 1.5, 1.75, 2, 2.25, and 2.5 in the timescale of Tryggvason, $t_{Tryg} = t\sqrt{A_t}$. The results are in good agreement with those from [30].

4.5.2 Rising Bubble benchmark problems

Now, we test the two phase flow system with surface tension given at the interface, using semi-implicit time discretization studied in [6, 18, 37] and discussed in Section 4.4. The rising bubble benchmark problem is proposed in [38]. The initial setup is $\Lambda = (0, 1) \times (0, 2)$, ϕ_0 describes a circular bubble of radius 0.25 centered at $(0.5, 0.5)$, and two different sets of physical constants described in Table 4.1 are considered. Here ρ_1, μ_1 are density and viscosity for outside the circle(Ω_1) and ρ_2, μ_2 are for inside the circle(Ω_2). g is the gravity force and σ is the surface tension coefficient. We compare the following quantities:

Test Case	ρ_1	ρ_2	μ_1	μ_2	g	σ
1	1000	100	10	1.	0.98	24.5
2	1000	1	10	0.1	0.98	1.96

Table 4.1: Two different sets of physical constants for the rising bubble benchmark.

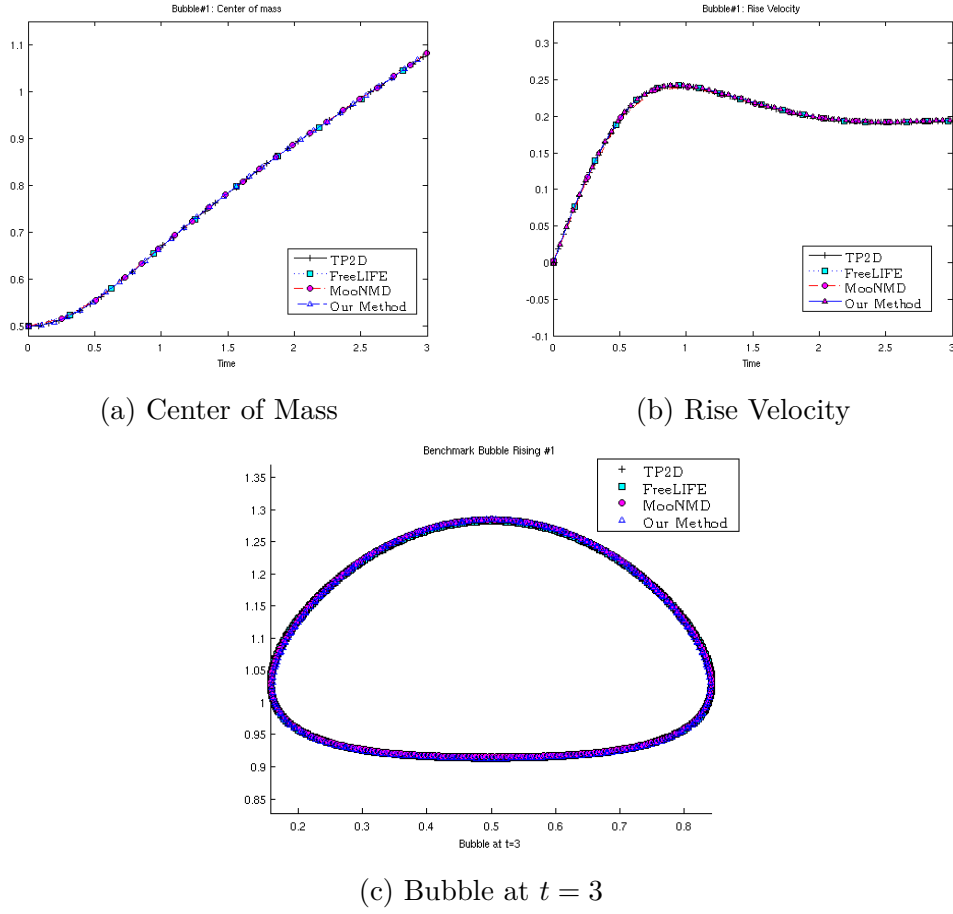


Figure 4.2: Comparison of the rising bubble test case #1.

$$\text{Center of mass: } \mathbf{X}_c := (x_c, y_c) = \frac{\int_{\Omega_2} \mathbf{x} d\mathbf{x}}{\int_{\Omega_2} 1 d\mathbf{x}}, \quad \text{Rise velocity: } \mathbf{U}_c := \frac{\int_{\Omega_2} \mathbf{U} d\mathbf{x}}{\int_{\Omega_2} 1 d\mathbf{x}}.$$

Figure 4.2, and 4.3 are the comparison of (a) center of mass, (b) rise velocity, and (c) shape of the bubble at $t = 3$, for each test case respectively. Also, left part of the Figure 4.4 is taken from [38], and the right end bubble is the result with our model. Computation is given with approximately 2,500 adaptive meshes and the numerical constants in Table 3.1. Our simulations are within the range determined by the benchmark algorithms.

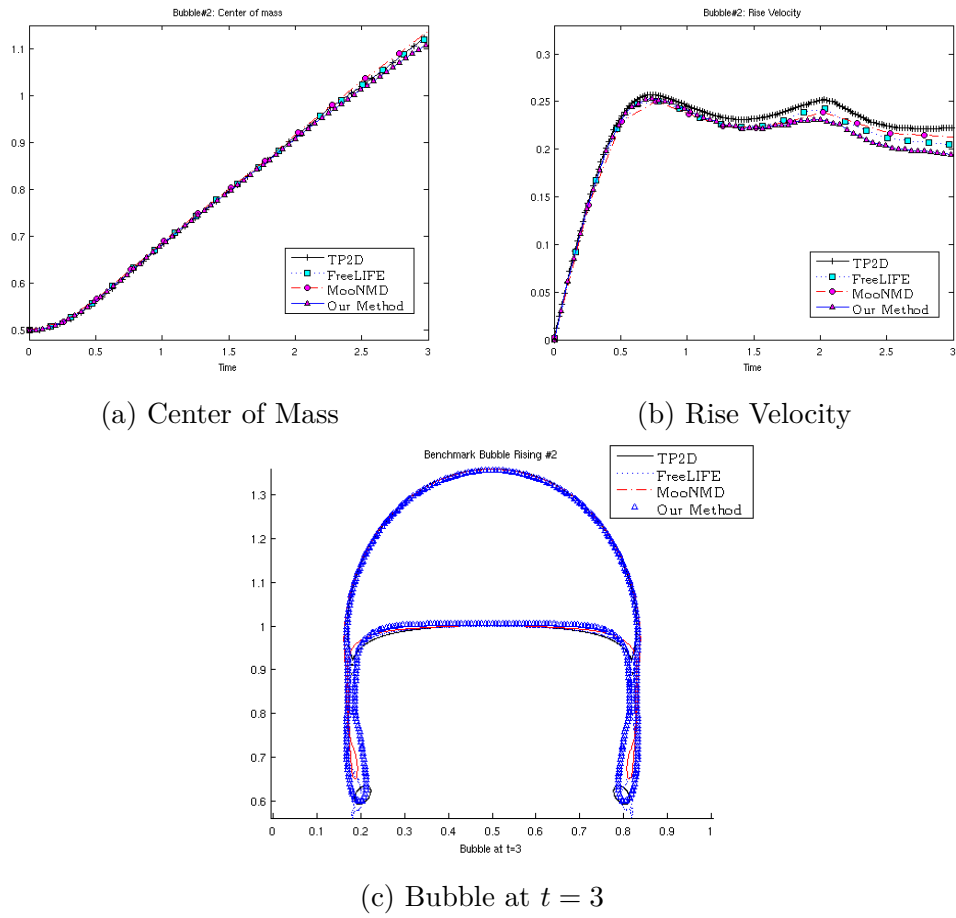


Figure 4.3: Comparison of the rising bubble test case #2.

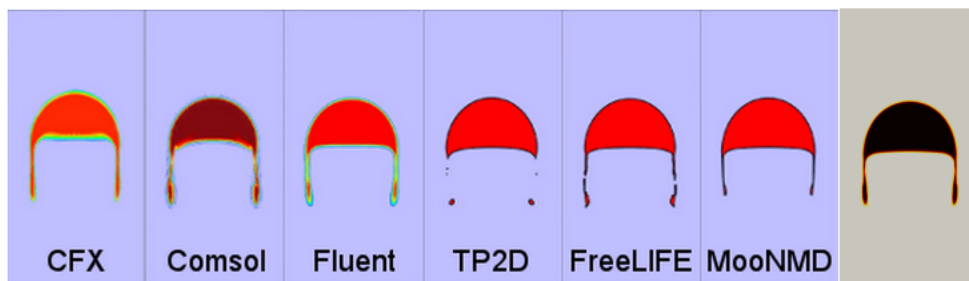


Figure 4.4: Rising bubble problem test case #2 at time=3. The right end bubble is our result, and left bubbles are from [38].

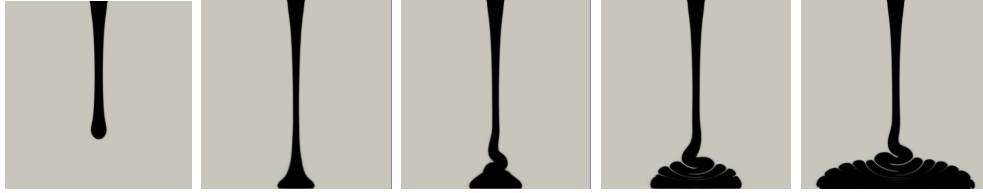


Figure 4.5: Buckling fluid in 2D.

4.5.3 Buckling fluid

We now apply our algorithm in the context of fluid buckling. The benchmark problem for two phase flow problem in 2D is Newtonian buckling fluid in the domain $\Lambda := (0, 1)^2$. Figure 4.5 illustrates the buckling of viscous fluid impacting a rigid plate. The inflow jet diameter is 0.1 m and the inflow velocity is 1 m/s. The physical parameters chosen for the fluid are $\rho = 1800 \text{ kg/m}^3$, $\mu = 250 \text{ Pa s}$ as in [55], which for the air, we take $\rho = 1 \text{ kg/m}^3$, and $\mu = 2 \times 10^{-5} \text{ Pa s}$. The results are obtained with adaptive mesh refinement.

We also present a 3D simulation in Figure 4.6 where $\Lambda = (0, 0.008)^3$. In this case, the inflow jet diameter is 0.0004 m and we take $\mu = 5 \text{ Pa s}$, and $\rho = 960 \text{ kg/m}^3$, corresponding to the Silicone oil. Also surface tension is applied at the fluids interface with a surface tension coefficient $\sigma = 0.021 \text{ N/m}$. The inflow velocity is 1.75 m/s.

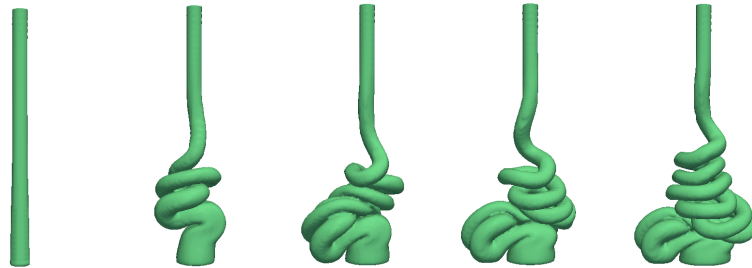


Figure 4.6: Buckling Silicone Oil in 3D.

5. NON-NEWTONIAN BOUNCING JET: KAYE EFFECT*

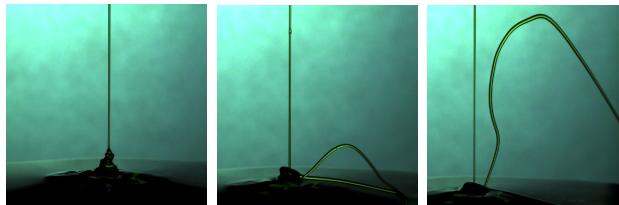


Figure 5.1: Kaye effect(from left to right): The fluid buckles at first producing a heap and a stream of liquid suddenly leaps outside the heap. Experiments taken with Dr.Thoroddsen and Dr.Li at High Speed Fluid Imaging Lab in KAUST.

The Kaye effect is a property of non-Newtonian fluid first described by Alan Kaye in 1963 [39]. It manifest itself when a thin stream of non-Newtonian fluid is poured into a dish of the same fluid. As pouring proceeds, a small stream of liquid occasionally leaps upward from the heap, see Figure 5.1. About 13 years later, Collyer and Fischer [16] revisit the Kaye effect and suggest that shear thinning, and elastic behavior as key ingredients of the Kaye effect. Additional laboratory experiments performed by Versluis et al. [54] and Binder and Landig [7] describe an experimental setting for the Kaye effect to manifest itself. They provide fluid viscosities, fluid shear-thinning rates, falling fluid velocities, and diameters. However, these two studies differ on two major points: (i) the relevance of elastic effects; (ii) the nature of the layer separating the heap and the outgoing jet. In [40], we show strong physical evidence for the existence of air layer between the heap and outgoing jet. Recently [42] also studied the Kaye effect by changing the angle of inclination

*Part of this chapter is reprinted with permission from “Leaping shampoo glides on a lubricating air layer” by S. Lee, E. Q. Li, J. O. Marston, A. Bonito, and S. T. Thoroddsen. Phys. Rev. E 87, 061001(R), 2013.

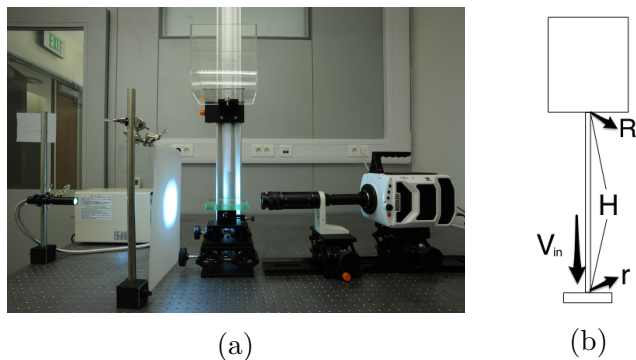


Figure 5.2: (a) Setup for free falling Kaye effect. We use the high speed video imaging camera, Phantom V1610 CMOS at frame rates up to 12,000 fps. Also we use a long-distance microscope(Leica Z16 APO) at optical magnifications up to $4\times$, giving $7\mu\text{m}/\text{px}$. Backlighting was accomplished with a 350W metal-halide lamp(Sumita), shone on to a diffuser. (b) Notations: H is the height of the free falling jet, R is the diameter of the inflow jet, r is the diameter of the jet at the bottom and V_{in} indicates the velocity of the jet at the bottom.

of the flat plate at the bottom, to see the various directions of the effect.

5.1 Experimental parameters

Several laboratory experiments of the Kaye effect were performed at High Speed Fluid Imaging Lab in KAUST to verify the basic phenomenon leading to the Kaye effect.

First, we consider free falling Kaye effect, where the shear-thinning fluid, commercial shampoo(Farmasi-baby-care, www.farmasi.com.tr), is poured on a flat plate from the tank; see Figure 5.2 for the basic setup. Table 5.1 reports whether no outgoing jet, sliding jet, or the bouncing jet height for changing the height of the free falling jet H , and see also Figure 5.3 providing pictures of the corresponding fluids from Table 5.1. Note that the jet diameter r and the jet speed V_{in} is measured when it creates the heap at the bottom.

Secondly, we replace the parameter H by the flow rate $Q(\text{ml}/\text{min})$, and now study

$H(\text{cm})$	$r(\text{mm})$	$V_{in}(\text{m/s})$	Out Jet Height
5	2.3458	0.08559	Buckling
10	1.4265	0.18703	Buckling
15	1.1095	0.34236	Buckling
20	0.8876	0.46282	Sliding
25	0.8242	0.54207	Sliding
30	0.6974	0.78933	2.5 mm
35	0.634	0.95417	4.5 mm
40	0.6657	1.15388	16 mm

Table 5.1: Free falling Kaye effect with the setup described in Figure 5.2: we change H from 5 cm to 40 cm. It shows that H should be higher enough (more than 30 cm) to observe the bouncing jet, the Kaye effect. Higher H gives larger V_{in} and smaller r .

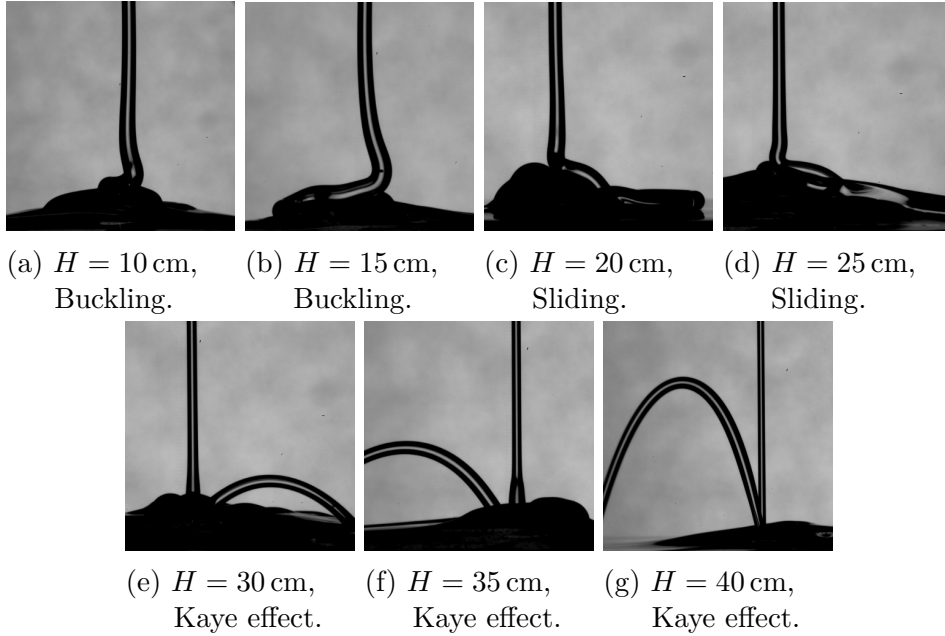


Figure 5.3: Pictures of the fluids corresponding to the parameters provided in Table 5.1.

the Kaye effect by varying Q . To achieve this, we use a syringe and an automatic pump to shoot the fluid at about 2 cm height from the floor. Table 5.2 reports

$Q(\text{ml}/\text{min})$	$r(\text{mm})$	$V_{in}(\text{m}/\text{s})$	Out Jet Height
5	0.6023	0.25043	None
6	0.5072	0.51037	Sliding
7	0.4121	0.7291	3 mm
8	0.3804	1.17924	12 mm

Table 5.2: Kaye effect depending on Q . Here the jet falls from a fixed height $H = 2$ cm. Again, larger Q gives larger V_{in} and smaller r .

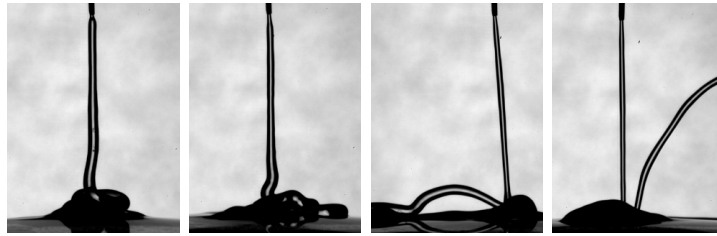


Figure 5.4: Jets with different volume flow rates: (5,6,7,and 8 ml/min). The Kaye effect is observed for values of Q starting at 7.

whether no outgoing jet, sliding jet, or the bouncing jet height for different flow rates, and we also observe that the radius of the in-jet(r) reduces while the velocity(V_{in}) increases. As we see from Figure 5.4, providing pictures of the corresponding fluids from Table 5.2, the Kaye effect is observed for flow rates Q larger than 7.

5.2 Shear-thinning model

An additional possible principal component of fluids exhibiting the Kaye effect is the ability for the fluid to undergo shear-thinning [7, 16, 54]. We adopt the Cross model [17] proposed in [54]. In this context, the viscosity depends on the shear $\gamma := |\nabla^s \mathbf{u}|$ as follows

$$\mu(\gamma) = \mu_\infty + \frac{\mu_0 - \mu_\infty}{1 + \left(\frac{\gamma}{\gamma_c}\right)^n}, \quad (5.1)$$

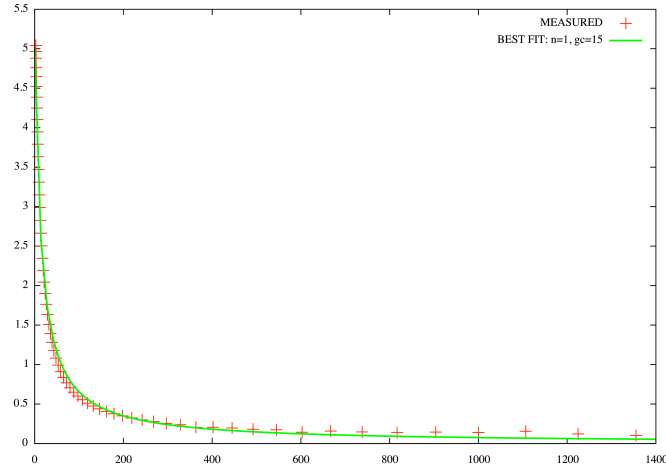


Figure 5.5: Shear-thinning viscosity of the shampoo: ‘+’ points illustrate the physical value of the viscosity(Y-axis) depending on shear(X-axis) observed from the rheology test of the shampoo. Solid line is the numerical viscosity model of the shampoo by using (5.1) with the constants (5.2).

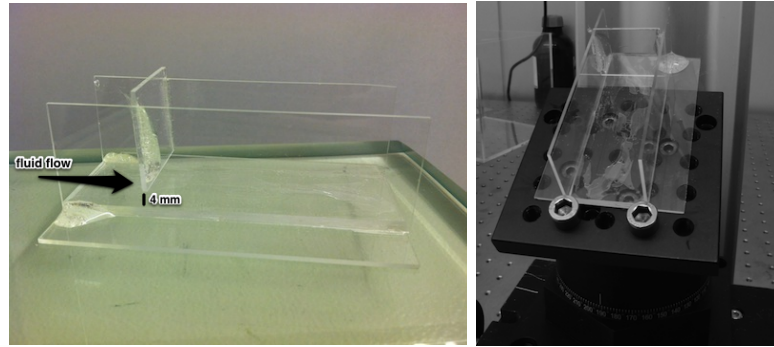
where μ_0 is the viscosity at zero shear stress, μ_∞ is the limiting viscosity for large shear stresses and γ_c , n are two extra fitting parameters. As a benchmark, we consider again the commercial shampoo Farmasi-baby-care which the shear-thinning constants are determined experimentally in [40] and given by

$$\mu_0 = 5.7 \text{ Pa s}, \quad \mu_\infty = 0.001 \text{ Pa s}, \quad \gamma_c = 15 \text{ s}^{-1} \quad \text{and} \quad n = 1, \quad (5.2)$$

see Figure 5.5. For the rheology test of the shampoo, the Carreau model is assumed here.

5.3 Existence of the lubricating air layer

From here, we will discuss the contents from [40]. In earlier studies it has been debated whether non-Newtonian effects are the underlying cause of this Kaye effect, making the jet glide on the top of a shear-thinning liquid layer, or whether an en-



(a) Fluid tank

(b) Reclined tank

Figure 5.6: Fluid tank: Fluid will drop from the top to this tank. We confine the pool to a narrow channel between two glass walls, through which we can view the jet-turning region within the pool. The large viscosity of the shampoo, only allows slow downhill gliding of the pool, at about 4 mm/s of pool surface velocity.

trained air layer is responsible. The work of Binder and Landig [7] has given indirect evidence for the presence of an air layer, by shining a light along the jet and showing that it acts as a light guide. Also the most recent experiments also suggest the presence of an air layer [42], but without direct observations. However [54] managed to produce stable leaping by directing the jet onto an angled pool, and they characterize the leaping behavior and suggest that non-Newtonian effects are crucial for the leaping, proposing the presence of a 100 μm thick layer of shear-thinning liquid between the jet and the pool. Despite the above indications the presence of an air layer for the highly non-Newtonian shampoo has not been conclusively decided up until now. However, the presence of an air layer has been already shown to cause leaping of Newtonian jets, by [50] and we refer to Section 5.5 for numerical evidence indicating the presence of an air layer in all cases.

Herein we show unambiguously that the jet slides on a lubricating air layer. We identify this layer by looking through the pool liquid and observing its rupture into fine bubbles. We used the same fluid and setting as shown at Figure 5.2, but by

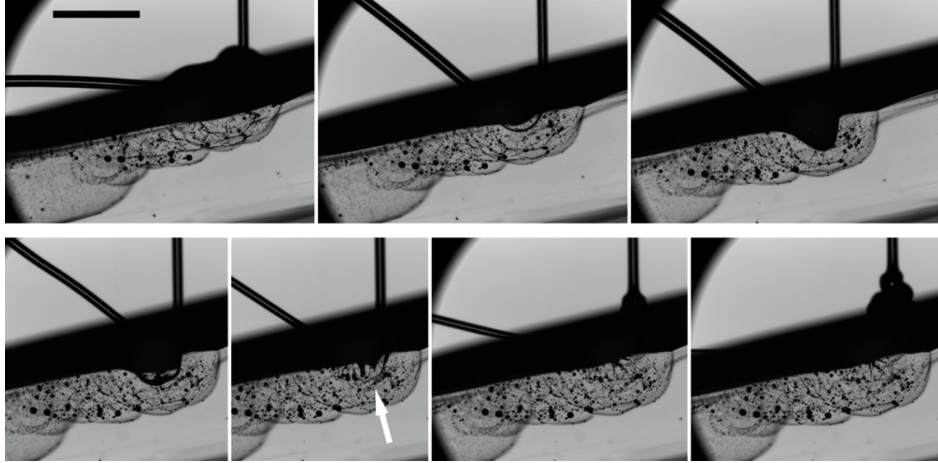


Figure 5.7: Overall view of the shampoo jet bouncing of an inclined pool of the same liquid. The white arrow points at the breakup of the air layer into threads and bubbles. The scale bar is 3 mm long. The relative times of the frames are $t = 0, 124, 287, 296, 308, 324$ and 335 ms from left to right and top to bottom. The incoming jet is 0.3 mm in diameter, approaching the pool at 1.2 m/s.

following [54] we stabilize the direction of the rebounding jet by inclining the pool, by about 14° . See Figure 5.6. This allows high magnification in-focus imaging within the pool. The rapid breakup of the thin air layer requires high speed video imaging at frame rates up to 12,000 fps, and the details about the setting and the device are given at [40].

Figure 5.7 shows the overall view of the leaping jet. When the jet initially hits the pool surface, it usually starts coiling, forming a small heap. Subsequently, it starts sliding down along the surface of this heap and exiting at a small angle to the horizontal along the pool surface, as shown in the first frame. The vertical force required to turn the jet has an opposite reaction on the pool, pushing downwards to form a dip into the pool surface, see the second frame. When this dip becomes deeper it turns the jet by a larger angle, directing it more in the vertical, as it leaves the pool. This proceeds and the jet points progressively more vertically, until it can

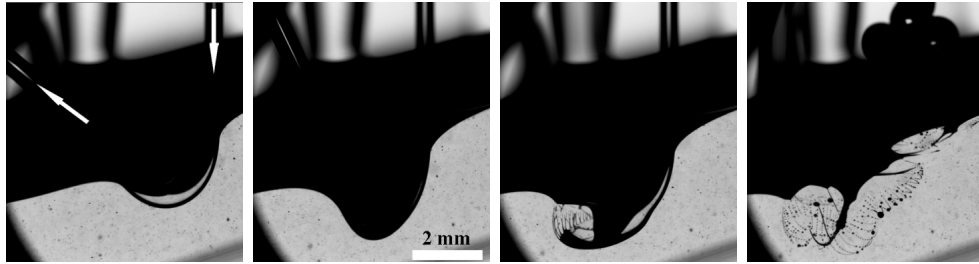


Figure 5.8: Break up of the air layer under the jet. Times relative to first observed rupture are $t = -717, -189, 20,$ and 132 ms(from left to right). The incoming jet is 0.56 mm in diameter and approaches the pool at 1.59 m/s.

intersect the incoming jet. The jet leaving the pool is significantly thicker than the one entering it, indicating it is decelerated by viscous tangential forces.(cf. [42, 54]).

The fourth frame shows a sudden disturbance of the jet, associated with a rupture of the air layer, which breaks up in the fifth frame (white arrow). Immediately during this breakup, the outgoing jet starts falling towards the pool and its diameter thins, as it is no longer fed by the incoming jet. In the last two frames, the jet has again started coiling at the pool surface, before again sliding down the heap to begin a new cycle. Myriad of bubbles are visible within the pool, from earlier breakups of the air layer.

Figure 5.8 shows a close up sequence of frames showing the breakup of the air layer, which occurs over about 40 ms. The layer first breaks up into filaments and then small bubbles. Also, by measuring the spacing and volume of the air threads, we can estimate the thickness of the original air layer, see [40].

By seeding small particles into the jet liquid we can measure the tangential velocity within the section of the jet moving below the original pool level. Keep in mind that we can only visualize within a fraction of the jet diameter, owing to the strong diffraction at the liquid-air interfaces. Figure 5.9 shows trajectories of a few

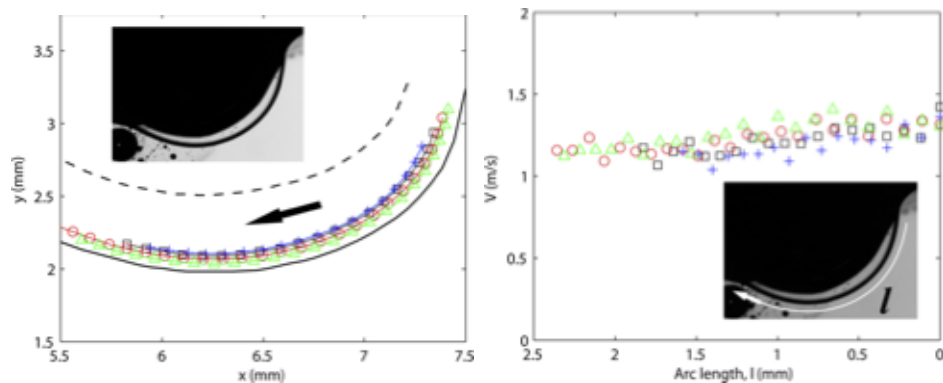


Figure 5.9: (left) The trajectory of typical particles within the jet. The solid curve marks the air layer and the dotted curve the upper side of the jet if the cross-section remains circular. (right) The velocity vs horizontal location along the curving jet.

particles, which we use to calculate the local velocities. There is no clear transverse velocity gradient within this section of the jet, down to about $50\ \mu\text{m}$ from the bottom. The velocity is even slightly faster closer to the bottom, by geometric effects. When seeding particles into the pool, the velocity under the air layer is insignificant, always less than $4\ \text{mm/s}$. This supporting our assertion that the shear is mostly confined within the thin air layer and rules out a $100\ \mu\text{m}$ shear-thinning layer substituting for the air film [54]. On the other hand, Fig. 5.9 shows that the tangential velocity clearly reduces along the jet, due to the underlying shear stress at the boundary.

We thereby propose that the Kaye effect has more to do with the stability of the air layer, rather than the non-Newtonian behavior inside the jet.

5.4 Numerical simulation of the Kaye effect

Finally, with experiments in previous sections and algorithms provided in Chapter 4, we obtain numerical simulation of the Kaye effect. We solve the two phase flow system with the level set at the domain $\Lambda \times [0, T]$, see Figure 5.10(a). Each cavity $\Lambda(t)$ is filled with non-mixing fluids, the air in $\Omega^-(t)$ and the shampoo in $\Omega^+(t)$. Recall

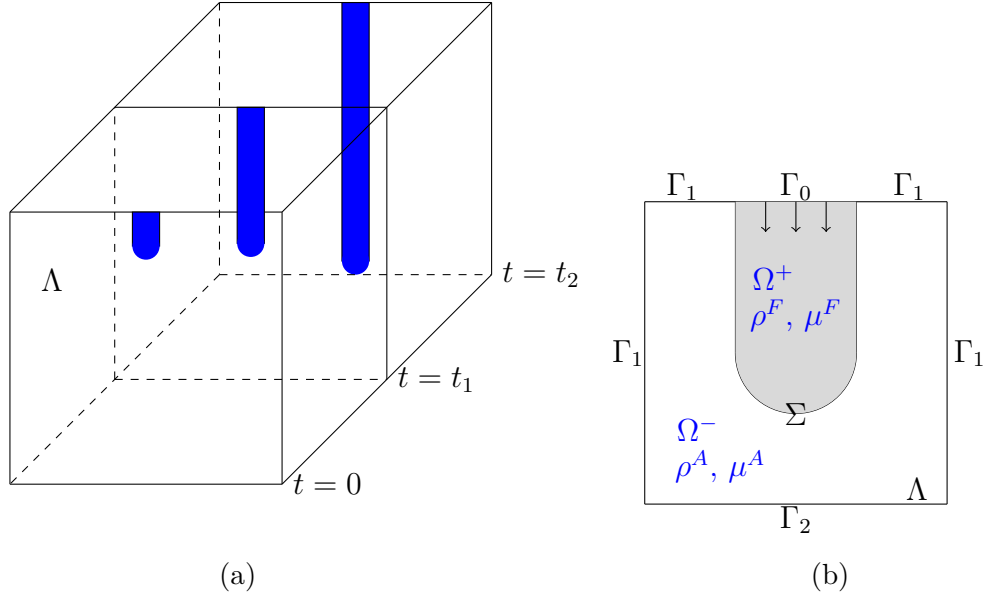


Figure 5.10: The computational domain with boundary.

that we take $\rho^- = 1 \text{ kg/m}^3$, $\mu^- = 2 \times 10^{-5} \text{ Pa s}$ for the air and $\rho^+ = 1020 \text{ kg/m}^3$, μ^+ defined with (5.1) and (5.2). Also recall that the conditions are

$$[\mathbf{u}] = 0 \quad \text{and} \quad [2\mu\nabla^S \mathbf{u} - p] \mathbf{n} = \sigma \kappa \mathbf{n} \quad \text{on} \quad \Sigma(t), \quad (5.3)$$

as, described in (4.2). The boundary of Λ is subdivided as illustrated in Figure 5.10(b). The inflow velocity is imposed on Γ_0 , the Neumann boundary on Γ_1 indicating the air and fluid can come in and go out, and no-slip boundary condition, Dirichlet boundary condition on Γ_2 , see Section 4.1, i.e

$$\mathbf{u} = \mathbf{f}_{\text{inflow}} \text{ on } \Gamma_0, \quad (2\mu\nabla^S \mathbf{u} - p) \boldsymbol{\nu} = 0 \text{ on } \Gamma_1, \quad \text{and} \quad \mathbf{u} = 0 \text{ on } \Gamma_2. \quad (5.4)$$

Following our laboratory experimental findings, the inflow fluid has velocity $\mathbf{f}_{\text{inflow}} = 1.75 \text{ m/s}$, radius of $R = 0.4 \text{ mm}$ and is poured from $H = 2 \text{ cm}$ height.

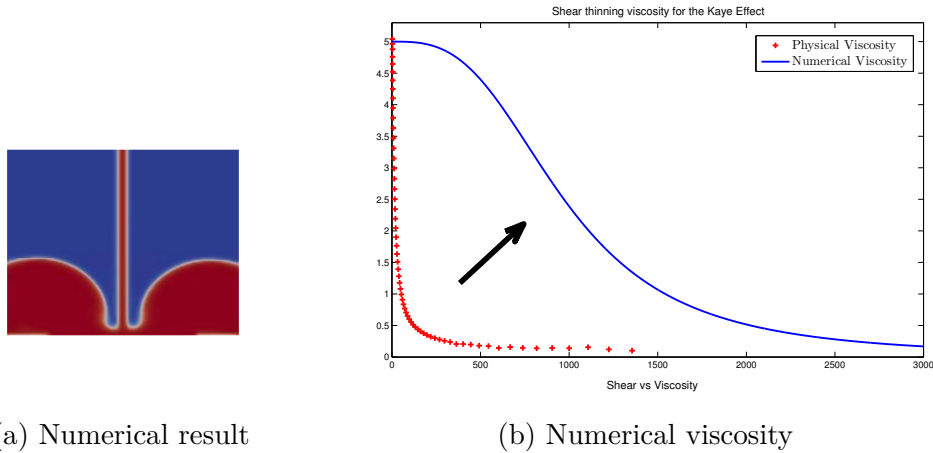


Figure 5.11: Shear-thinning viscosity of the fluid. (a) Illustrates the numerical result with the shear-thinning constants given in (5.2). (b) Shear-thinning viscosity with values in (5.2)(dotted line), and (5.5) with the solid line.

As it turned out, the shear-thinning viscosity constants given in (5.2) was not obvious in this setting, see Figure 5.11a. In fact, we observe that (i) the shear thinning is too strong, (ii) the numerical shear is too large, (iii) a critical ingredient is missing in the mathematical model, or (iv) the assumption using Carreau model for the rheology test does not suit with our numerical algorithm.

In view of (i) above, we now consider the following parameters for the shear-thinning:

$$\mu_0 = 5.7 \text{ Pa s}, \quad \mu_\infty = 0.001 \text{ Pa s}, \quad \gamma_c = 970 \text{ s}^{-1} \quad \text{and} \quad n = 3. \quad (5.5)$$

They correspond to a slower shear-thinning effect appearing at large shear, see Figure 5.11b. Figure 5.12 reports the corresponding numerical simulation; where the Kaye effect is observed. We emphasize the crucial need of adaptive finite element method allowing for the algorithm to capture the lubricating air layer responsible for the Kaye effect.(See Section 5.3).

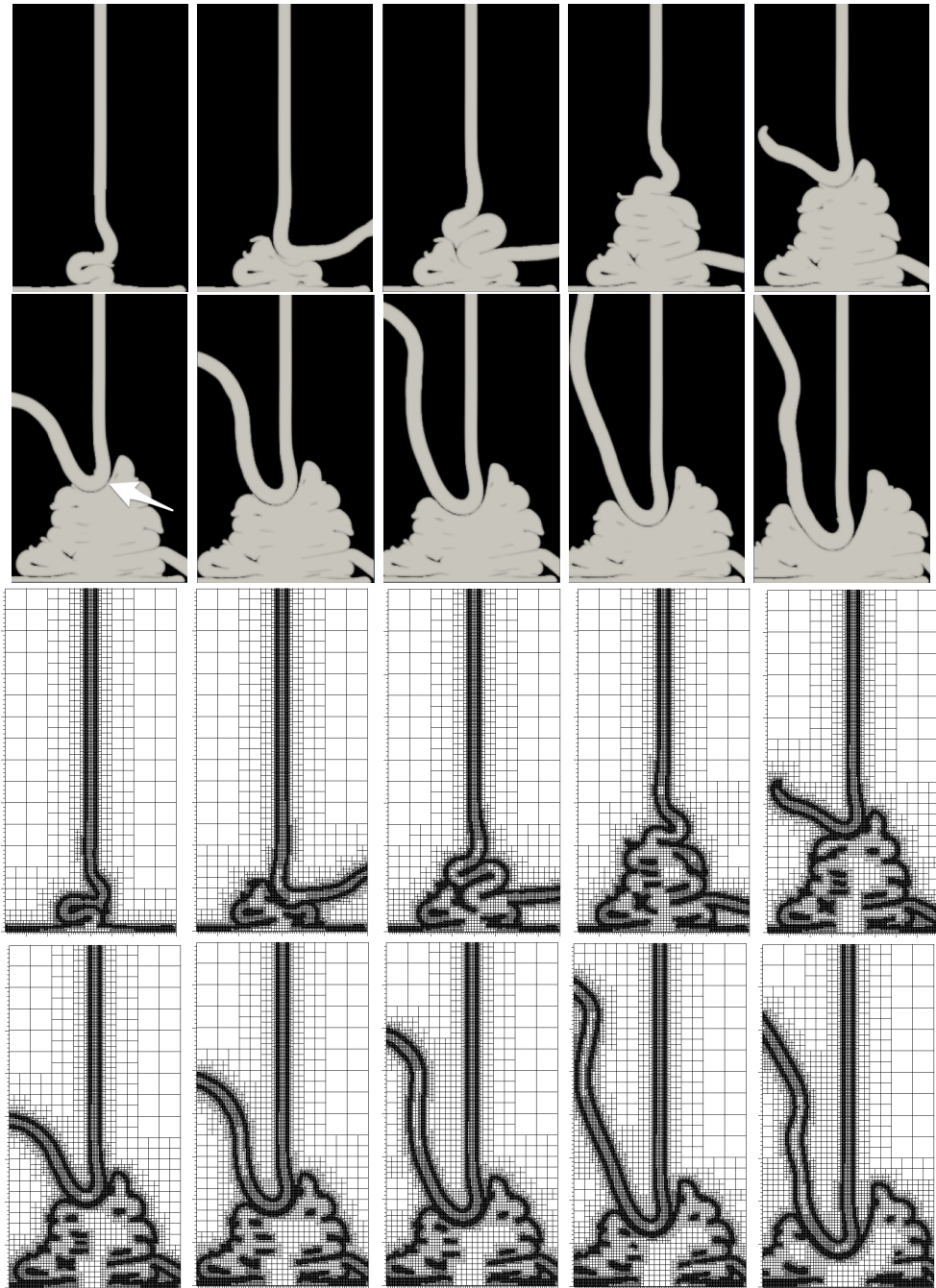


Figure 5.12: Numerical simulation of the Kaye effect with adaptive meshes (from left to right and top to bottom). From the fifth frame to the end, we observe the air layer under the leaping jet(white arrow).

5.5 Newtonian bouncing jets

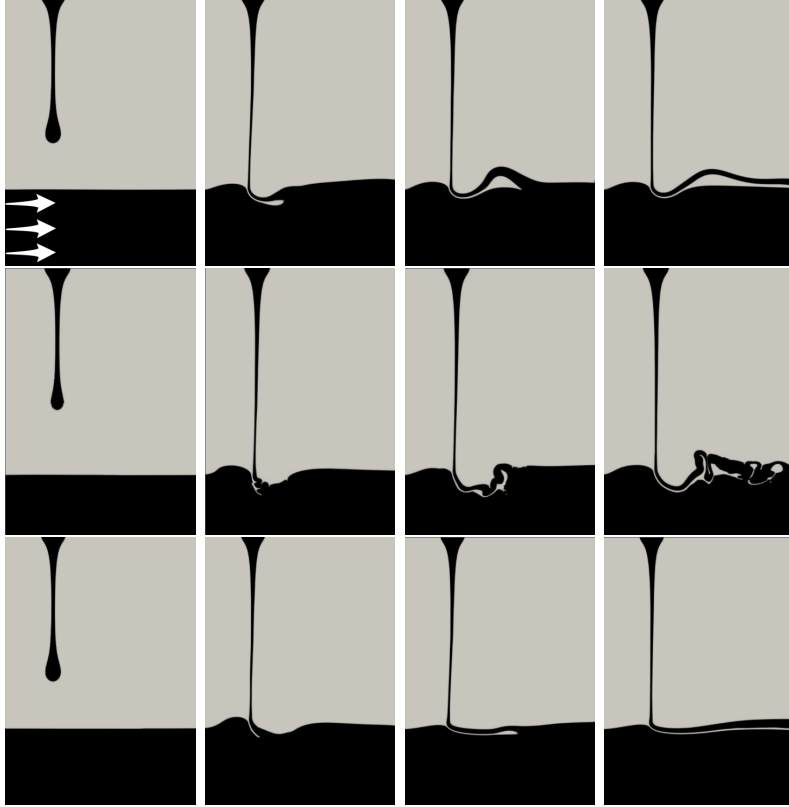


Figure 5.13: Newtonian bouncing jet (from left to right). The white arrow indicates the direction of the bath flow. (Top) Numerical simulation of the bouncing jet with bath velocity 8 cm/s and surface tension coefficient $\sigma = 21$ mN/m. (Middle) Without the surface tension. (Bottom) With surface tension but increased the bath velocity to 25 cm/s. We observe the existence of the air layer between the jet and the bath.

Bouncing jets were observed more recently [50] on a different setting, namely Newtonian fluids (no shear-thinning). However, this time the jet falls into an already filled rotating bath which helps to sustain the air layer between the bath and the jet.

Figure 5.13 reports the numerical simulation in this setting. The height of the jet is 4 cm, and its radius is 0.25 cm, the speed of the rotating bath is 8 cm/s and

25 cm/s with the direction plotted at Figure 5.13. The property of the fluid is the Silicone oil with viscosity $\mu = 250$ mPa s, and density $\rho = 960$ kg/m³.

The bouncing depends on the speed of the bath velocity and we observe higher bath velocity will make the jet just glide on the surface rather than bouncing. Again, an air layer is observed on our numerical simulations, see Figure 5.13.

It turns out surface tension is an important effect stabilizing the jet in this setting, as illustrated in Figure 5.13(Middle), reporting the simulation without surface tension and with a surface tension coefficient as $\sigma = 21$ mN/m.

6. CONCLUSION

In this thesis, appropriate method for numerical simulation of the bouncing jets have been discussed. We provided experimental and numerical evidences supporting the presence of an air layer in both Newtonian and non-Newtonian cases.

Our findings agree with [7] and for the range of parameters tested disprove the thesis in [50, 54] supporting a lubricated shear-thinned layer instead of an air layer during the Kaye effect. In fact, our studies indicate that the key element in the bouncing jets considered is the ability for the fluid to sustain an air layer. For Newtonian fluid, this is done by an entrained bath velocity while a shear thinning viscosity fluid together with an appropriate falling flow rate are sufficient for the Kaye effect.

There is an another interesting debate whether viscoelastic effects are a possible factor facilitating the Kaye effect [7, 54]. Future direction of research may include numerical investigations of the Kaye effect for viscoelastic fluids.

To achieve the numerical simulations of bouncing jets presented in this work, we improved standard pressure correction projection methods failing to be optimal for open boundary problem and stable for variable time stepping. In both cases, modified algorithms are designed, analyzed and implemented: optimal error convergence rates are guaranteed mathematically and observed numerically.

BIBLIOGRAPHY

- [1] E. Anderson, Z. Bai, J. Dongarra, A. Greenbaum, A. McKenney, J. Du Croz, S. Hammerling, J. Demmel, C. Bischof, and D. Sorensen. Lapack: A portable linear algebra library for high-performance computers. In *Proceedings of the 1990 ACM/IEEE Conference on Supercomputing*, Supercomputing '90, pages 2–11, Los Alamitos, CA, USA, 1990. IEEE Computer Society Press.
- [2] S. Balay, M. F. Adams, J. Brown, P. Brune, K. Buschelman, V. Eijkhout, W. D. Gropp, D. Kaushik, M. G. Knepley, L. C. McInnes, K. Rupp, B. F. Smith, and H. Zhang. PETSc users manual. Technical Report ANL-95/11 - Revision 3.4, Argonne National Laboratory, 2013.
- [3] W. Bangerth, R. Hartmann, and G. Kanschat. deal.II — a general purpose object oriented finite element library. *ACM Trans. Math. Softw.*, 33(4), 2007.
- [4] W. Bangerth, T. Heister, L. Heltai, G. Kanschat, M. Kronbichler, M. Maier, B. Turcksin, and T. D. Young. The deal.ii library, version 8.0. *arXiv preprint*, 2013.
- [5] W. Bangerth, T. Heister, L. Heltai, G. Kanschat, M. Kronbichler, M. Maier, B. Turcksin, and T. D. Young. The deal.ii library, version 8.1. *arXiv preprint*, 2013.
- [6] E. Bänsch. Finite element discretization of the Navier-Stokes equations with a free capillary surface. *Numer. Math.*, 88(2):203–235, 2001. ISSN 0029-599X. doi: 10.1007/PL00005443. URL <http://dx.doi.org/10.1007/PL00005443>.

- [7] J. M. Binder and A. J. Landig. The kaye effect. *European Journal of Physics*, 30(6):S115, 2009. URL <http://stacks.iop.org/0143-0807/30/i=6/a=S03>.
- [8] L. S. Blackford, J. Demmel, J. Dongarra, I. Duff, S. Hammarling, G. Henry, M. Heroux, L. Kaufman, A. Lumsdaine, A. Petitet, R. Pozo, K. Remington, and R. C. Whaley. An updated set of basic linear algebra subprograms (blas). *ACM Transactions on Mathematical Software*, 28:135–151, 2001.
- [9] A. Bonito and R. H. Nochetto. Quasi-optimal convergence rate of an adaptive discontinuous Galerkin method. *SIAM J. Numer. Anal.*, 48(2):734–771, 2010. ISSN 0036-1429. doi: 10.1137/08072838X. URL <http://dx.doi.org/10.1137/08072838X>.
- [10] A. Bonito, J.-L. Guermond, and B. Popov. Stability analysis of explicit entropy viscosity methods for non-linear scalar conservation equations. *Math. Comp.*, 83(287):1039–1062, 2014. ISSN 0025-5718. doi: 10.1090/S0025-5718-2013-02771-8. URL <http://dx.doi.org/10.1090/S0025-5718-2013-02771-8>.
- [11] S. C. Brenner and L. R. Scott. *The mathematical theory of finite element methods*, volume 15 of *Texts in Applied Mathematics*. Springer, New York, third edition, 2008. ISBN 978-0-387-75933-3. doi: 10.1007/978-0-387-75934-0. URL <http://dx.doi.org/10.1007/978-0-387-75934-0>.
- [12] C. Burstedde, L. C. Wilcox, and O. Ghattas. `p4est`: Scalable algorithms for parallel adaptive mesh refinement on forests of octrees. *SIAM Journal on Scientific Computing*, 33(3):1103–1133, 2011.
- [13] A. J. Chorin. Numerical solution of the Navier-Stokes equations. *Math. Comp.*, 22:745–762, 1968. ISSN 0025-5718.

- [14] A. J. Chorin. On the convergence of discrete approximations to the Navier-Stokes equations. *Math. Comp.*, 23:341–353, 1969. ISSN 0025-5718.
- [15] P. G. Ciarlet. *The finite element method for elliptic problems*, volume 40 of *Classics in Applied Mathematics*. Society for Industrial and Applied Mathematics (SIAM), Philadelphia, PA, 2002. ISBN 0-89871-514-8. doi: 10.1137/1.9780898719208. URL <http://dx.doi.org/10.1137/1.9780898719208>. Reprint of the 1978 original [North-Holland, Amsterdam; MR0520174 (58 #25001)].
- [16] A. Collyer and P. J. Fischer. The kaye effect revisited. *Nature*, 261:682, 1976.
- [17] M. M. Cross. Rheology of non-newtonian fluids: A new flow equation for pseudoplastic systems. *Journal of Colloid Science*, 20(5):417 – 437, 1965.
- [18] G. Dziuk and C. M. Elliott. An Eulerian approach to transport and diffusion on evolving implicit surfaces. *Comput. Vis. Sci.*, 13(1):17–28, 2010. ISSN 1432-9360.
- [19] E. Emmrich. Stability and error of the variable two-step BDF for semilinear parabolic problems. *J. Appl. Math. Comput.*, 19(1-2):33–55, 2005. ISSN 1598-5865.
- [20] B. Engquist, A.-K. Tornberg, and R. Tsai. Discretization of Dirac delta functions in level set methods. *J. Comput. Phys.*, 207(1):28–51, 2005. ISSN 0021-9991. doi: 10.1016/j.jcp.2004.09.018. URL <http://dx.doi.org/10.1016/j.jcp.2004.09.018>.
- [21] A. Ern and J.-L. Guermond. *Theory and practice of finite elements*, volume 159 of *Applied Mathematical Sciences*. Springer-Verlag, New York, 2004. ISBN

0-387-20574-8. doi: 10.1007/978-1-4757-4355-5. URL <http://dx.doi.org/10.1007/978-1-4757-4355-5>.

- [22] E. Gabriel, G. E. Fagg, G. Bosilca, T. Angskun, J. J. Dongarra, J. M. Squyres, V. Sahay, P. Kambadur, B. Barrett, A. Lumsdaine, R. H. Castain, D. J. Daniel, R. L. Graham, and T. S. Woodall. Open MPI: Goals, concept, and design of a next generation MPI implementation. In *Proceedings, 11th European PVM/MPI Users' Group Meeting*, pages 97–104, Budapest, Hungary, September 2004.
- [23] V. Girault and P.-A. Raviart. *Finite element approximation of the Navier-Stokes equations*, volume 749 of *Lecture Notes in Mathematics*. Springer-Verlag, Berlin-New York, 1979. ISBN 3-540-09557-8.
- [24] V. Girault and P.-A. Raviart. *Finite element methods for Navier-Stokes equations*, volume 5 of *Springer Series in Computational Mathematics*. Springer-Verlag, Berlin, 1986. ISBN 3-540-15796-4. doi: 10.1007/978-3-642-61623-5. URL <http://dx.doi.org/10.1007/978-3-642-61623-5>. Theory and algorithms.
- [25] K. Goda. A multistep technique with implicit difference schemes for calculating two- or three-dimensional cavity flows. *Journal of Computational Physics*, 30(1):76 – 95, 1979. ISSN 0021-9991. doi: [http://dx.doi.org/10.1016/0021-9991\(79\)90088-3](http://dx.doi.org/10.1016/0021-9991(79)90088-3). URL <http://www.sciencedirect.com/science/article/pii/0021999179900883>.
- [26] S. Gottlieb and C.-W. Shu. Total variation diminishing runge-kutta schemes. *Mathematics of Computation of the American Mathematical Society*, 67(221): 73–85, 1998.

- [27] S. Gottlieb, C.-W. Shu, and E. Tadmor. Strong stability-preserving high-order time discretization methods. *SIAM review*, 43(1):89–112, 2001.
- [28] C. Grossmann and H.-G. Roos. *Numerical treatment of partial differential equations*. Universitext. Springer, Berlin, 2007. ISBN 978-3-540-71582-5. doi: 10.1007/978-3-540-71584-9. URL <http://dx.doi.org/10.1007/978-3-540-71584-9>. Translated and revised from the 3rd (2005) German edition by Martin Stynes.
- [29] J.-L. Guermond. Un résultat de convergence d’ordre deux en temps pour l’approximation des équations de navier-stokes par une technique de projection incrémentale. *ESAIM: Mathematical Modelling and Numerical Analysis - Modélisation Mathématique et Analyse Numérique*, 33(1):169–189, 1999.
- [30] J.-L. Guermond and A. Salgado. A splitting method for incompressible flows with variable density based on a pressure poisson equation. *Journal of Computational Physics*, 228(8):2834 – 2846, 2009. ISSN 0021-9991.
- [31] J. L. Guermond and J. Shen. Velocity-correction projection methods for incompressible flows. *SIAM J. Numer. Anal.*, 41(1):112–134 (electronic), 2003. ISSN 0036-1429.
- [32] J. L. Guermond and J. Shen. On the error estimates for the rotational pressure-correction projection methods. *Math. Comp.*, 73(248):1719–1737 (electronic), 2004. ISSN 0025-5718.
- [33] J. L. Guermond, P. Mineev, and J. Shen. Error analysis of pressure-correction schemes for the time-dependent Stokes equations with open boundary conditions. *SIAM J. Numer. Anal.*, 43(1):239–258 (electronic), 2005. ISSN 0036-1429.

- [34] J. L. Guermond, P. Mineev, and J. Shen. An overview of projection methods for incompressible flows. *Comput. Methods Appl. Mech. Engrg.*, 195(44-47):6011–6045, 2006. ISSN 0045-7825.
- [35] J.-L. Guermond, R. Pasquetti, and B. Popov. Entropy viscosity method for nonlinear conservation laws. *Journal of Computational Physics*, 230(11):4248–4267, 2011.
- [36] M. Heroux, R. Bartlett, V. H. R. Hoekstra, J. Hu, T. Kolda, R. Lehoucq, K. Long, R. Pawlowski, E. Phipps, A. Salinger, H. Thornquist, R. Tuminaro, J. Willenbring, and A. Williams. An Overview of Trilinos. Technical Report SAND2003-2927, Sandia National Laboratories, 2003.
- [37] S. Hysing. A new implicit surface tension implementation for interfacial flows. *Internat. J. Numer. Methods Fluids*, 51(6):659–672, 2006. ISSN 0271-2091.
- [38] S. Hysing, S. Turek, D. Kuzmin, N. Parolini, E. Burman, S. Ganesan, and L. Tobiska. Quantitative benchmark computations of two-dimensional bubble dynamics. *International Journal for Numerical Methods in Fluids*, 60(11):1259–1288, 2009.
- [39] A. Kaye. A bouncing liquid stream. *Nature*, 197:1001, 1963.
- [40] S. Lee, E. Q. Li, J. O. Marston, A. Bonito, and S. T. Thoroddsen. Leaping shampoo glides on a lubricating air layer. *Phys. Rev. E*, 87:061001, Jun 2013.
- [41] T. Lockhart, J. Bomber, and N. Brewer. Bouncing of newtonian liquid jets, 2010. URL <https://www.uwec.edu/Physics/research/lockhartjets.htm>.
- [42] J. Ochoa, C. Guerra, and C. Stern. New experiments on the kaye effect. In J. Klapp, A. Cros, O. Velasco Fuentes, C. Stern, and M. A. Rodriguez Meza,

- editors, *Experimental and Theoretical Advances in Fluid Dynamics*, Environmental Science and Engineering, pages 419–427. Springer Berlin Heidelberg, 2012.
- [43] S. Osher and J. A. Sethian. Fronts propagating with curvature-dependent speed: algorithms based on hamilton-jacobi formulations. *Journal of computational physics*, 79(1):12–49, 1988.
- [44] J. Shen. On error estimates of the projection methods for the Navier-Stokes equations: second-order schemes. *Math. Comp.*, 65(215):1039–1065, 1996. ISSN 0025-5718. doi: 10.1090/S0025-5718-96-00750-8. URL <http://dx.doi.org/10.1090/S0025-5718-96-00750-8>.
- [45] C.-W. Shu and S. Osher. Efficient implementation of essentially non-oscillatory shock-capturing schemes. *Journal of Computational Physics*, 77(2):439 – 471, 1988. ISSN 0021-9991.
- [46] M. Sussman, P. Smereka, and S. Osher. A level set approach for computing solutions to incompressible two-phase flow. *Journal of Computational physics*, 114(1):146–159, 1994.
- [47] R. Témam. Une méthode d’approximation de la solution des équations de Navier-Stokes. *Bull. Soc. Math. France*, 96:115–152, 1968. ISSN 0037-9484.
- [48] R. Témam. Sur l’approximation de la solution des équations de Navier-Stokes par la méthode des pas fractionnaires. II. *Arch. Rational Mech. Anal.*, 33:377–385, 1969. ISSN 0003-9527.
- [49] R. Temam. *Navier-Stokes equations*, volume 2 of *Studies in Mathematics and its Applications*. North-Holland Publishing Co., Amsterdam, third edition, 1984.

ISBN 0-444-87558-1; 0-444-87559-X. Theory and numerical analysis, With an appendix by F. Thomasset.

- [50] M. Thrasher, S. Jung, Y. K. Pang, C.-P. Chuu, and H. L. Swinney. Bouncing jet: A newtonian liquid rebounding off a free surface. *Phys. Rev. E*, 76:056319, Nov 2007.
- [51] L. J. P. Timmermans, P. D. Mineev, and F. N. Van De Vosse. An approximate projection scheme for incompressible flow using spectral elements. *International Journal for Numerical Methods in Fluids*, 22(7):673–688, 1996. ISSN 1097-0363.
- [52] A.-K. Tornberg. *Interface tracking methods with application to multiphase flows*. Doctoral dissertation, Royal Institute of Technology, 2000.
- [53] G. Tryggvason. Numerical simulations of the rayleigh-taylor instability. *J. Comput. Phys.*, 75(2):253–282, Apr. 1988. ISSN 0021-9991.
- [54] M. Versluis, C. Blom, D. van der Meer, K. van der Weele, and D. Lohse. Leaping shampoo and the stable kaye effect. *Journal of Statistical Mechanics: Theory and Experiment*, 2006(07):P07007, 2006.
- [55] L. Ville, L. Silva, and T. Coupez. Convected level set method for the numerical simulation of fluid buckling. *International Journal for Numerical Methods in Fluids*, 66(3):324–344, 2011. ISSN 1097-0363. doi: 10.1002/flid.2259. URL <http://dx.doi.org/10.1002/flid.2259>.